UCL Université catholique de Louvain

École polytechnique de Louvain (EPL)

epl

High-Areal Capacity Microbatteries from Symmetrical Interdigitated 3D Nanowire Network Electrodes

Dissertation presented by

Joel Ojonugwa OMALE

for obtaining the Master's degree in

Chemical and Materials Engineering

Supervisors

Prof. Luc PIRAUX, Prof. Alexandru VLAD

Readers

Pascal VAN VELTHEM, Prof. Yaroslav FILINCHUK

Academic year 2017-2018

Acknowledgements

Ever since I resolved to devoting myself to scientific pursuits, I find that I have been particularly blessed with people, teachers and colleagues alike, who have made the journey extremely easy. During the course of this work, I was tutored in the experimental aspects relating to material syntheses and electrochemistry by P. van Velthem and R. Rupp, respectively. They have taught me so much about experimentation, and I am grateful for their patience in the face of the barrage of questions with which I inundated them (which, knowing how pushy I am, is no small feat), and for reviewing my drafts multiple times.

To my supervisors – Prof. L. Piraux and Prof. A. Vlad – I am honoured to have been allowed to work on this subject, and for your confidence in my judgements, allowing me pursue the work as I willed, while providing unconditional support and guidance whenever I needed them.

I would also like to express my gratitude to everyone at IMCN/BSMA, who guided and assisted me through this work: particularly V. Van Kerckhoven, for the laser patterning of my samples, and for proofreading my draft on the description of the technique; C. D'Haese, for the trainings and regular assistance with atomic force microscopy; D. Magnin , for the trainings and assistance with scanning electron microscopy; T. da Câmara Gomes, for allowing me displace him many times during his plasma etching sessions, and, with Dr F. A. Araujo, for addressing my challenges with plasma etching and electrodeposition.

Finally, I express my inestimable gratitude to the FAME Master program, which has supported my studies abroad and offered me a well-rounded, world-class education; and to my parents and siblings, for their undying love and support during my Master's studies. Thank you!

Joel Ojonugwa OMALE

Louvain-la-Neuve, June 2018

Abstract

High-Areal Capacity Microbatteries from Symmetrical Interdigitated 3D Nanowire Network Electrodes

by Joel Ojonugwa OMALE

The inability of state-of-the-art microbatteries to simultaneously meet the performance and size requirements for modern-day, constantly miniaturizing microelectronic devices has created an impetus to finding better materials and designs capable of fulfilling these requirements. Thin film batteries are ubiquitous, but the presence of small active materials precludes their use in high-energy applications; on the other hand, while thick-film batteries are capable of providing adequate energy for many of these devices, long and tortuous ion diffusion pathways limit their use for high-power applications. This work explores a strategy of decoupling power and energy capabilities of microbatteries by using functionalized three-dimensional interconnected core-shell nanowire networks as the electrodes' active material in a 3D microbattery. Specifically, it presents the foremost attempt at fabricating a symmetrical microbattery with interdigitated electrodes from polyaniline, a conducting polymer, whose electrochemistry allows its use in symmetrical batteries; the interdigitated architecture of the electrodes allows its compact integration on a single substrate, consistent with the requirements for microelectronics applications. The Pt nanowire network was prepared by template-assisted electrodeposition; the nanowires and thin films were functionalized with the active material, polyaniline, by electroless deposition, and the interdigitated architecture was effected by laser ablation of the as-grown Pt nanowire network. For the same thickness of active material, the thin-film microbattery presents an areal capacity of $0.09\,\mu\mathrm{A\,h\,cm^{-2}}$, while the 3D microbattery presents $2.7\,\mu\mathrm{A\,h\,cm^{-2}}$, 30 times higher than the thin film's, consistent with the expectations of increased mass loading. The thick-film battery, despite having 40 times more material than the thin film, presents an areal capacity of only $0.45\,\mu\mathrm{A\,h\,cm^{-2}}$, evidence of limitations by longer ion diffusion pathways. The volumetric capacity of the 3D battery is compared with similar batteries in the literature, and it is found to compare favourably, with even better cycle characteristics. This work is a proof of concept of working symmetrical batteries with interdigitated electrodes based on a 3D core-shell nanowire network architecture.

Contents

List of Figures

List of Tables

List of Abbreviations

3DNWN	**3D N**anowire **N**etwork
AFM	**A**tomic **F**orce **M**icroscope
CV	**C**yclic **V**oltammetry
DOD	**D**epth **o**f **D**ischarge
ECD	**E**lectro**c**hemical **d**eposition
ED	**E**lectroless **D**eposition
EM	**Em**eraldine
EPL	**E**cole **P**olytechnique de **L**ouvain
FEG	**F**ield **E**mission **G**un
IHP	**I**nner **H**elmholtz **P**lane
IoT	**I**nternet **o**f **T**hings
LIB	**L**ithium-**i**on **B**attery
LM	**L**eucoe**m**eraldine
LSV	**L**inear **S**weep **V**oltammetry
OHP	**O**uter **H**elmholtz **P**lane
PAni	**P**oly**ani**line
PC	**P**oly**c**arbonate
PL	**P**icosecond **l**aser technology
PN	**P**er**n**igraniline
Redox	**R**eduction-**o**xidation
SCE	**S**tandard **C**alomel **E**lectrode
SEM	**S**canning **E**lectron **M**icroscopy
SHE	**S**tandard **H**ydrogen **E**lectrode
UCL	**U**niversité **c**atholique de **L**ouvain
XPS	**X**-ray **P**hotoelectron **S**pectroscopy

List of Symbols

Roman symbols

a	lattice parameter	m
C	capacitance	$\mathrm{F}\ (\mathrm{C\,V^{-1}})$
$C_\circ$	ion bulk concentration	$\mathrm{mole/m^3}$
C_d	double-layer capacitance	$\mathrm{F}\ (\mathrm{C\,V^{-1}})$
C_{rate}	charge/discharge rate	
C_P	practical capacity	$\mathrm{A\,h\,cm^{-2}}$
C_T	theoretical capacity	$\mathrm{A\,h\,cm^{-2}}$
$E_{1/2}$	midway between peak potentials	V
E_{cell}	cell potential	$\mathrm{V}\ (\mathrm{J\,C^{-1}})$
E°_{cell}	standard cell potential	$\mathrm{V}\ (\mathrm{J\,C^{-1}})$
E_g	bandgap energy	eV
$E^\circ_{half-cell}$	standard electrode potential	$\mathrm{V}\ (\mathrm{J\,C^{-1}})$
E_{ocv}	open-circuit voltage (or potential)	V
ΔE_p	peak-to-peak separation	V
F	Faraday constant	$\mathrm{F}\ (1\,\mathrm{F}{=}96\,485\,\mathrm{C\,mol^{-1}})$
ΔG	Gibbs free energy change	$\mathrm{J\,mol^{-1}}$
i	current	A
i_p	peak current	A
$J_{cut-off}$	cut-off current density	$\mathrm{A\,cm^{-2}}$
k_b	Boltzmann constant	$1.38 \times 10^{-23}\,\mathrm{J\,K^{-1}}$
K	equilibrum constant	
P	power density	$\mathrm{W\,h\,m^{-2}}$
q	amount of charge	$\mathrm{coulomb}$
Q	reaction quotient	
R	universal gas constant	$8.314\,\mathrm{J\,mol^{-1}\,K^{-1}}$
R_i	internal cell resistance	V
R_s	overall cell resistance	Ω
T	temperature	K
T_p	Peierls transition temperature	K
v	rate of reaction	$\mathrm{mol\,s^{-1}\,m^{-2}}$

$[X^+]$	concentration of ion X^+	$\mathrm{mol\,m^{-3}}$

Greek symbols

α	transfer coefficient	
η	overpotential	V
$(\eta_{ct})_{a,c}$	charge-transfer (or activation) polarization	V
$(\eta_c)_{a,c}$	concentration polarization	V
ν	scan rate	$\mathrm{V\,s^{-1}}$

1 Introduction

Experts project that the number of connected Internet of Things (IoT) devices will rise from the present-day value of 17.6 billion to anywhere between 20 billion and 50 billion in 2020, and have a concomitant market value of almost 6 trillion Euros [1–3]. The reason for this is obvious: with wide-ranging applications from medicine, to consumer applications, to infrastructure management, IoT promises increased efficiency and economic benefits to individuals and enterprises. Moreover, global warming, increasing energy demand due to population growth, and recurring energy crises have accelerated the growth of the proportion of renewable energy sources in the total energy mix for all purposes [4]; however, renewable energy sources are intermittent, therefore requiring the integration of energy storage systems. These facts have caused a growing demand for higher-power-density and longer-life-cycle batteries, of all dimensions, than what is available on the market.

The most prevalent type of battery for electronics and mobility applications is the lithium-ion battery (LIB) in which lithium ions shuttle between its electrodes, typically graphite (Li_xC_6) as anode and lithium cobalt oxide ($LiCoO_2$) as cathode, through a lithium ion-containing electrolyte and a separator, which allows for passage of lithium ions but not electrons [5]. However, there are certain issues associated with the prevalent lithium-ion batteries. First, because the most commonly used cathode material is lithium- and cobalt-based ($LiCoO_2$), there is the issue of sustainability, as the abundance of lithium and cobalt (even more so) in the earth are limited; recycling can alleviate some of this, but their imminent scarcity will ultimately lead to an increased price of batteries. Second, there are safety concerns, as the presence of both combustible material and oxidising agent carries the risk of runaway reactions that can result in fire and explosions; although this can be avoided by selecting an electrolyte of appropriate chemistry, accidents are still likely, as, like in most devices, accidents occur due to the manufacturers' attempting to cram more active materials in the same volume, causing internal short-circuits. The final issue is a rather counterintuitive one: We know that one of the chief purposes of energy-storing devices is to reduce CO_2 emission; however, the carbon footprint of LIB production requires well over 100 recharges of each battery before we see any carbon-related benefits [6]. It is obvious, then, that for LIBs to meet the need of curbing CO_2 emission, this number must be drastically reduced.

By and large, there are two currently explored approaches to tackling these issues:

(1) by using nanostructured electrodes, and (2) by exploring other, less expensive materials. Since the electrochemical performance of electrode materials are strongly dependent on their sizes, morphologies, and structures, researches are proving that many of the present issues can be circumvented by using nanostructures. In particular, nanostructures offer short diffusion lengths, which make it possible to charge and discharge batteries faster, i.e., have higher power; nanostructures allow for more facile strain accommodation during charging and discharging than their bulk counterpart, which leads to better cyclability; by virtue of their sizes, the ratio of their surface area to volume is large, which enhances the kinetics of the reactions they undergo, resulting in higher specific capacity; and because the transport of multivalent ions is faster in nanostructures than in bulk materials, using nanostructures enable practical batteries based on larger ions (Mg^{2+}, Al^{3+}, say) than lithium ion, which are typically capable of storing more energy [5–8].

Applications of nanostructures for batteries are mostly as *thin-films* in so-called "microbatteries", which are batteries that have their components stacked either one on another in a planar configuration, or side by side on current-collecting layers [9]. Microbatteries are the choice batteries for microelectronic devices (e.g., IoT devices), because they are miniature and have areal performances consistent with the requirement for such devices. There's a plethora of advantages to using batteries of such configuration. For one, because the thicknesses of the electrodes are in the nanoscale, they tend to be extremely stable upon cycling, because of the shortened Li^+ diffusion pathway [10] and reduction in side reactions by the cell components [11]; for another, since all the components of thin film batteries tend to be solid, they have large thermal stability, making it usable in a temperature range as wide as from $-40°$ to $150°$ C [9]. Notwithstanding these advantages, there are still demerits. Notably, it's challenging to simultaneously achieve high areal energy and power density in such batteries, because increasing film thickness (in order to attain higher energy density) leads to increased Li^+ diffusion lengths (thereby sacrificing power density); moreover, the solid-state electrolytes typically employed have lower ionic conductivities than liquid electrolytes [12]. To surmount these demerits, specifically regarding the competition between areal energy and power density in thin-film batteries, batteries made of *three-dimensional (3D) nanostructures* are proving to be better alternatives to thin-film batteries [9, 13–16]. This is because by using 3D structures on the same footprint area (as a thin film), there's more material and active area, while retaining the short-ion transport distances associated with nanostructures. Therefore, with such architecture, high areal energy and power density batteries can be simultaneously attained; moreover, there's the added advantage that energy density can be easily tailored by increasing the height of the 3D nanostructures.

Furthermore, the finiteness of metal ores implies that, over time, extraction and manufacturing of battery components therefrom will be cost-inhibitive, leading to an

overall rise in the cost of batteries. Many advances in battery technology are underway, but the preponderance of these advances are to replace liquid electrolytes with solid – typically polymer [17] – electrolytes. However, electrolytes account for less than ten percent of battery costs [18, 19]; hence, only as much effort need be expended in optimizing battery costs. The electrodes, on the other hand, account for, at least, fifty percent of the costs [18, 19]; consequently, much more research effort need be directed at finding cheaper, more sustainable replacements. As in electrolytes, polymers are also intriguing alternatives for electrode materials, because they are more sustainable, relatively environmentally benign, possess propitious mechanical properties – light, flexible, etc.– relatively easy to manufacture, and are electroactive towards a host of other ions besides Li^+ [20].

It is the purpose of this work to immensely contribute to these novel approaches to tackling the issues of the sustainability of LIBs, and to the tradeoff between areal energy and power density in thin-film microbatteries. Specifically, this work produces, and studies the performance of, a *symmetrical* microbattery – i.e., a microbattery whose electrodes are *exactly* the same material– with side-by-side interdigitated electrodes made of 3D interconnected platinum (core)-polyaniline (shell) nanowire networks (3DNWN). Polyaniline (PAni) is selected as the active material, because its electrochemistry is suitable for this purpose: It's a conducting polymer that has three main redox states – *leucoemeraldine*, *emeraldine*, and *pernigraniline* – depending on the fraction of benzenoid and quinoid states in the overall structure. The method of synthesis employed in this work – *electroless deposition* – produces PAni in its conducting emeraldine-salt state, which is, in fact, the mid-redox state; thus, by applying a reducing or oxidizing current to the (PAni) emeraldine-salt electrodes (charging), the electrodes are reduced or oxidized to the leucoemeraldine or pernigraniline state, respectively, resulting in a potential difference that can drive charges during discharge of the battery. Furthermore, the use of interdigitated electrodes allows compact integration of the anode and cathode on a single substrate, consistent with the requirements for microelectronics applications, and reduces the ohmic resistance of the system that results from ions having to shuttle long distance between electrodes [14].

To this end, studies to determine the optimal growth parameters for PAni films on Pt substrates and on 3D interconnected Pt nanowire networks were initially undertaken; then the stability windows of potential liquid electrolytes were determined. Subsequently, cyclic voltammetry (CV) was done under variable conditions to determine the redox potentials for the transitions between the PAni redox states, hence the potential window within which cells fabricated therefrom are operable; then, the cycling performance of PAni films were evaluated. Finally, the interdigitated architecture was effected on the 3D nanowire networks, and its cycling performance determined. At all stages, various characterization techniques were used to track and instruct the progress of the work.

This work is divided into three sections. The first section is a literature survey of

important concepts relevant to understanding theoretical aspects, motivation of the work, and the choices of experiments carried out. The second section presents experimental details regarding syntheses, characterization, battery assembling, etc. The third section presents the results obtained and discusses them, from which relevant conclusions are drawn and recommendations are made for future works.

2 Literature Survey

This chapter is a literature survey of concepts, which, in the author's opinion, are relevant to understanding this work. To whet the interest of the reader, it begins on a light note with a short historical context of energy storage; then, it segues to the more involved subject of the science and engineering of batteries, touching on the thermodynamics of energy storage and so on. Microbatteries, the interest of this work, are subsequently particularized, discussing their requirements, the structural aspects that confer their characteristics on them, and the state of the art. Finally, an adequate treatment of the solid-state physics and electrochemistry of conducting polymers, and of polyaniline (PAni), specifically, is given[1]

2.1 A Brief History of Energy Storage

In 1938, a German archaeologist Wilhelm Konig excavated a 14-cm-long ovoid clay jar containing a copper cylinder that encased an iron rod in Khujut Rabu, a local area to the South-East of Baghdad, Iraq [21, 22]. Figure 2.1a shows the excavated artefacts and Figure 2.1b shows the schematic of the device as reconstructed. The artefacts were dated to the Parthian era, *ca.* 250 BC to AD 225 [22], and its discoverer theorized that it's some sort of galvanic battery, akin to the present-day wet-cell battery, which was used for electroplating [22]. There's an alternative view that the device might have been used instead for medical purposes – probably as a local electrical analgesic [22] – after analyses of the characteristics of such a cell; the consensus, however, is that this device, popularly known as the "Baghdad battery" or the "Parthian battery," from antiquity is the first testament to humans' success at converting chemical energy to electrical energy, ages before the underlying principles were known.

Two parties independently discovered, in 1745, that it was possible to store electric charges (from an external source) between two electrical conductors, one inside and the other outside a glass bottle. The parties were the Dutch Professor of physics, Pieter van Musschenbroek, working with his student Andreas Cunaeus, in Leiden, and the German deacon, Ewald Georg von Kleist. Coincidentally, both parties made the discovery while attempting the experiments developed by Georg Matthias Bose, who had shown

[1]The author has elected to present this chapter (and much of this work, in fact) in a conversational tone; this, it is hoped, will reduce the tedium that characterizes the reading of scientific works; so, every now and then, a witty remark may be seen. Don't hesitate to *lol!*.

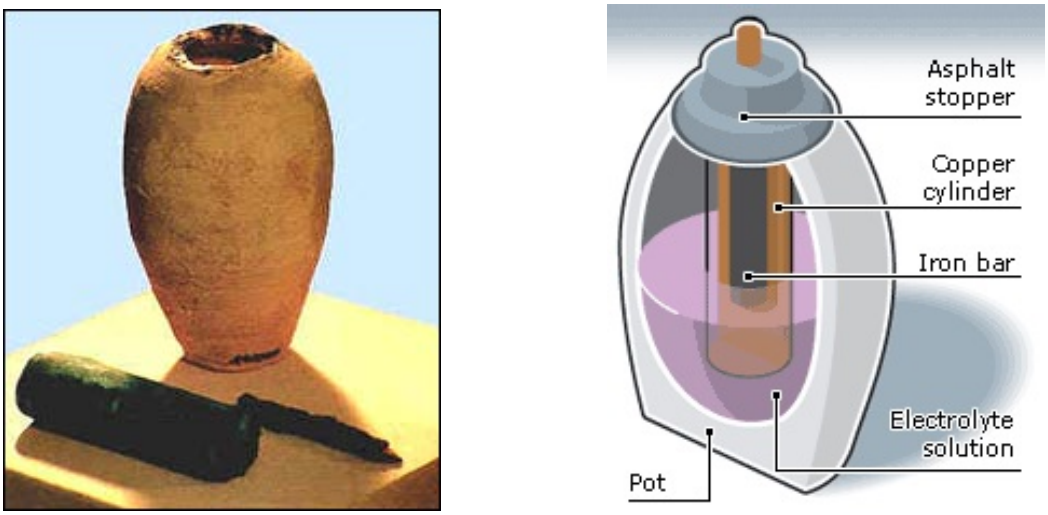

(a) (b)

FIGURE 2.1: (a) Set of excavated artefacts; (b) Schematic of the key components of the Baghdad battery [23].

that alcoholic spirits could be set alight by passing electricity through water; however, while Kleist was trying to prove his theory of electricity that treated electricity as a fluid [24], Musschenbroek and Cunaeus, working in Leiden (the eponym for the device), the Netherlands, were, in their own words, "[trying] to increase the power and longevity of electricity" [25]. The earliest Leyden jars, shown in Figure 2.2a, consisted of a hand-held glass jar filled with water, with a metallic nail passing through the cork stopper to contact water in the jar. The water in the jar is charged by electrostatic generators through the metallic nail; the hand holding the jar and the water act as plates such that, on charging the water, opposite charges accumulate on the hand holding the jar. Discharge is done by touching the nail with a finger, causing charges to leave the water through the metallic nail to the hand holding the jar, neutralizing the charges from water (as they are of opposite signs), usually resulting in shock.

To a reader versed in energy storage devices, it should be obvious that Figure 2.2b is, in fact, what is now called a *capacitor*; however, the term "battery" was first used to describe an assembly of Leyden jars connected in series or in parallel to enhance the properties of an individual jar. It was Benjamin Franklin, who, in a letter to Peter Collinson in 1749, first coined the term to describe multiple Leyden jars connected in series [28, 29]:

> Upon this We made what we call'd an *Electrical Battery* [italics in original], consisting of eleven Panes of large Sash Glass, arm'd with thin leaden Plates, pasted on each Side, placed vertically, and supported at two Inches Distance on Silk Cords . . . .

Nowadays, "battery" is strictly used to refer an assembly of devices (cells) that store and release energy by spontaneous chemical reactions by its components, not to just any

(a)

(b)

(c)

FIGURE 2.2: (a) Early water-filled Leyden jar [26]; (b) Latter Leyden jar that used metallic plates [27]; (c) A "battery" of four Leyden jars connected in parallel (Courtesy: Museum Boerhaave, Leiden.)

assembly of energy storage devices[2]. In this sense, the first true battery ever constructed was by Allessandro Volta, professor of experimental physics at the University of Pavia, Italy, in 1800 [21]. It was called the *Voltaic pile* (see Figure 2.3), and it consists of two electrodes – zinc and copper – which are stacked serially and separated by a layer of cloth or cardboard paper soaked in brine (the electrolyte) [30].

More practical batteries emerged, like the Daniel cell invented by a British chemist John Frederic Daniel in 1836, the porous pot cell invented by a British instrument maker

[2]Strictly speaking, while "cell" refers to a *single* device that interconverts chemical and electrical energy, "battery" refers to an *assembly* of such devices, typically connected in series. In this work, however, this distinction is disregarded and the terms are used interchangeably.

FIGURE 2.3: Volta's electric pile on display in the *Tempio Voltiano* in Como [21].

John Dancer in 1838, the Poggendorff cell invented by a German scientist Johann Christian Poggendorff in 1859, and the gravity cell invented by a Frenchman named Callaud in 1860. All these inventions were improvements on the Voltaic pile, and they were non-rechargeable in the sense that once their active components were expended, they couldn't be made to supply any more current. The first rechargeable battery was the lead-acid battery invented by Gaston Planté in 1859; the cell was recharged by applying current in an opposite direction (opposite to how it flows during discharge) [21]. The lead-acid battery is still used today in automobiles for ignition.

Subsequently, other batteries were developed between 1859 and mid-1900s. But the first great leap in rechargeable batteries is the lithium-ion battery (LIB) developed by an English chemist Michael Stanley Whittingham in 1976 [31]. The development was made after a series of studies on the fundamental properties of Li_xTiS_2 due to his team's finding that titanium disulfide (TiS_2) could be used as the cathode of a high-energy-density reversible battery with lithium anode [32]. Besides TiS_2, several other sulfides were pursued, but most of them had voltages less than 2.5 V vs. metallic lithium anode. Since then, other groups the world over have been pursuing oxide cathodes [33]; these pursuits led to to the commercialization of the first LIB in 1991 by Sony.

The need to solve the challenges faced by earlier LIBs has led to the second great leap in battery science and technology, *viz.* the use of nanoscale materials to manufacture battery components. The Introduction (1) has already presented some of the challenges and the approaches being taken, and this is, in fact, still the state of the art; as we go

through sections in this work, we should recognize this *leitmotif*.

2.2 The Science and Engineering of Batteries

In the foregoing section, the course of development of energy storage devices was cursorily reviewed, mainly emphasizing developments in batteries. There are other ways energy can be (and is being) stored, like in capacitors, fuel cells, solar thermal energy, hydrogen storage in solids (metal hydrides and carbon nanostructures), and so on; however, most of these storage systems tend to have low gravimetric and volumetric energy density[3], therefore requiring massive and bulky systems, if they were to be constructed for the various storage requirement. It's obvious, then, they are unsuitable for most modern devices (mobile phones, laptops, automobiles) in which energy storage is required; nevertheless, in instances when size is not an issue – supply of electrical energy to the grid, for instance – they present some advantages. We shall no more consider any of these, as they are outside the purview of this work[4].

Now, what is a battery? A battery is a device that uses electrochemical oxidation-reduction (redox) reactions to directly convert the chemical energy of an electrode material (the active materials) into electrical energy. Batteries can be *rechargeable* or *nonrechargeable*, depending on whether the redox reactions that lead to the supply of electrical energy can be reversed by applying electrical energy to reform the reactants (electrodes!). Non-rechargeable batteries are also called *primary* batteries, and the reactants can't be reformed once they are expended; in that case, they are said to be "dead." As expected, the rechargeable batteries are also called *secondary* batteries, and by supplying electrical energy to reverse the cell reactions that initially provided the electrical energy during discharge, they are recharged.

Fundamentally, the electrochemical principles of all batteries are the same – whether nonrechargeable or rechargeable. To elucidate these principles, we shall consider the types that can be said to be archetypical of each class, *viz.* the Leclanché cell and the lithium-ion battery (LIB), respectively. But, first, we should take a quick detour to applied thermodynamics.

[3]These terms refer to the amount of energy stored per unit mass and volume, respectively. All relevant battery jargons will be fully defined in Section 2.2.2.

[4]This section is a synthesis of some textbooks – Refs. [33–37] – discussions with R. Rupp, and the author's experience. Citations are made only in areas that, from the author's judgement, presents a certain author's opinion or are from journal publications. But if you, my dear reader, find errors, the author is the culprit.

2.2.1 A Detour to Applied Thermodynamics: Electrochemistry

Since the application of thermodynamic principles to designing the first steam engine that led to the industrial revolution, leapfrogging much of the western world into an era of immense plenty [38], there's been no aspect of applied thermodynamics that has been, arguably, as pivotal to economic growth as electrochemistry[5]. Electrochemistry is the study of the relationship between chemical change and electrical work [37]. We can see that this relationship is in two directions: either electrical work leading to chemical change, or chemical change leading to electrical energy. Batteries operate in the latter direction, and the systems in which these changes occur is the *galvanic* or *voltaic* cell; thus, a battery is basically a voltaic cell.

a. Notations

An electrochemical process is *always* associated with the movement of electrons between species in a redox reaction; the chemical specie that *loses* electrons is said to be "oxidized" and that which *gains* the lost electrons is said to be "reduced." We see, then, that oxidation and reduction processes always occur concomitantly. Since each specie, in a sense, causes the reaction that the other undergoes, the reduced specie is said to be the "oxidizing agent," and the oxidized specie the "reducing agent." A voltaic cell (or galvanic cell) uses a chemical reaction to produce electrical energy; because the chemical reaction spontaneously occurs, the change in its Gibbs free energy is negative, i.e., $\Delta G < 0$. Figure 2.4 shows the basic construction of a battery (or voltaic cell). It consists of two electrodes, which conduct electricity between the cell and the surroundings, in contact with electrolytes that contain ions that participate in the redox reactions at the electrodes.

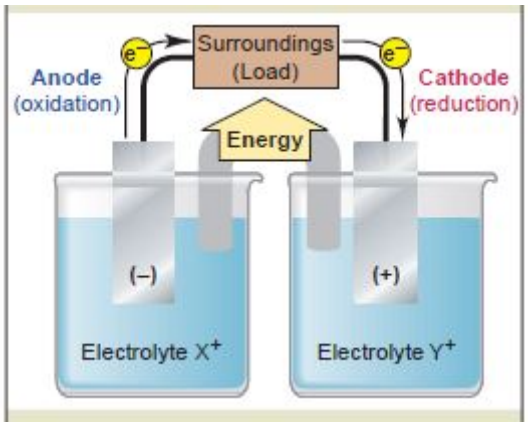

FIGURE 2.4: Schematic of a basic battery (Adapted from Ref. [37]).

[5]This is purely the author's opinion and it's no doubt open to debate. But once you consider the applications of electrochemistry to *almost* all aspects of energy storage, to metal extraction and refining, to sensors, etc., you might sway his way.

An electrode is the cathode or anode depending on the half-reaction that occurs there: when oxidation occurs at an electrode, that electrode is the anode, and the electrons lost there travel through wires to an external load, to the cathode, where reduction occurs. By convention [6], the cathode of a voltaic cell is the positive electrode and the anode the negative electrode, and each redox reaction occurring at the electrodes is called a *half-reaction*.

Let's consider Figure 2.4 to be a hypothetical voltaic cell, whose anode is a metal X in contact with an electrolyte containing its ions X^+, and the cathode a metal Y in contact with an electrolyte of its ion Y^+. The respective half-reactions are:

Oxidation half-reaction

$$X \rightarrow X^+ + e^-$$

Reduction half-reaction

$$Y^+ + e^- \rightarrow Y$$

Overall (cell) reaction

$$X + Y^+ \rightarrow X^+ + Y \qquad \Delta G < 0$$

Now, electrons are being transferred in the X/Y^+ reactions, but electrical energy wouldn't have been generated if the X/Y^+ pair were in the same beaker; physically separating and connecting them by an external circuit ensures that the electrons travel through the external circuit to the other specie. This electron flow is the observed current. The separation of half-reactions is the essential idea of a battery[7]; when X loses electrons, the resulting cation X^+ enters the solution, while the lost electrons passes through the anode to the connecting wire to the cathode, where Y^+ in solution accepts them and reduces to Y atoms; therefore, as the cell operates, electrons are continuously generated at the anode, leading to an excess of electrons (thus a negative charge) relatively to the cathode, where the electrons are consumed. This is the basis of the sign convention of the electrodes in a voltaic cell. Furthermore, we may observe a narrow tube bridging both electrolytes. This tube is called a "salt bridge," and its purpose is to complete the circuit, assuring charge neutrality during redox reactions. We know that, initially, the oxidation half-cell contains a neutral solution of X^+ and anions, A^-, say, but as X atoms loses electrons, the electrolyte will develop a net positive charge, as X^+ enters the solution. In the same vein, the reduction half-cell leads to a net negative charge during cell operation, as Y^+ combines with the lost electrons, leaving the solution to form Y atoms on the cathode. The resulting charge imbalance in both half-cells would stop the cell from running; so, to avoid this, both electrolytes are

[6] Actually, this convention is not merely arbitrary – we shall soon see that it's related to the nature of the phenomena causing the electrons to flow. *La patience!*

[7] The reader may recall that in the Volta's electrical pile, electrolytes are soaked in clothes. These clothes act to electrically separate the electrodes from each other; therefore, they are called "separators" in real batteries, and they act to electronically isolate the electrodes from each other while assuring ionic contact.

ionically bridged with the salt bridge, which contains ions that can shuttle between both electrolytes and complete the circuit, thereby assuring charge balance in both half-cells. In practical batteries, there's usually no need for a separate salt bridge, as the presence of a "separator," soaked in the electrolytes as both electrodes, already allows the shuttling of ions to assure charge balance, while assuring their electrical isolation.

The standard notation [35] for describing our hypothetical cell is

$$\mathrm{X(s)\,|\,X^{+}(aq)\,|\,|\,Y^{+}(aq)\,|\,Y(s)}.$$

The key components of this notation are

- The anode half-cell is written to the left of the cathode half cell.
- The single vertical line represents a phase boundary and the nature of the phases are written in brackets next to the specie. If there's more than a specie within a phase, the species are separated by commas.
- Half-cell components usually appear in the same order as in the half-reaction, and the electrodes appear at extremities of the notation.
- The double vertical line is used to separate half-cells, and also represents the phase boundary on either side of the salt bridge.

One might wonder why such an assembly produces electrical energy. In such a set-up consisting of two different materials, the electrode which acts as cathode or anode depends on the relative ease with they give up electrons. X is the anode because it loses electrons easier than Y; we say that electrons at X experience greater *electrical potential* than at Y [37], leading to a *net* flow of electrons from X to Y when the circuit is closed. Thus, *the spontaneous reaction occurs due to the difference in the abilities of these materials to give up their electrons and the ability for electrons to flow through the circuit.*

b. Cell potential E_{cell}

In light of these, we can confidently deduce that the purpose of a battery or voltaic cell is to convert the free energy change of a spontaneous reaction into the kinetic energy of electrons (the electrical energy) moving through an external circuit. The electrical energy is, in fact, proportional to the difference in electrical potential of both electrodes [35, 37]. This difference is called the *cell potential* E_{cell} or *voltage* or *electromotive force (emf)*. Its unit is the volts V($1V = 1J/C$).

The E_{cell} measured is affected by changes in concentration as the reaction proceeds and by energy losses due to heating of the cell and external circuit; therefore, in order to compare the output of different cells, a *standard cell potential* E°_{cell} is used. E°_{cell} is the

potential measured at a specific temperature (298 K) when no current is flowing and all components are in their standard state: 1 atm for gases, 1 M for solutions, the pure solid for electrodes [35, 37]. Since the overall cell is constituted of half-cells, the potential of each half-cell contributes to the overall potential; the potential of each half-reaction (when all the components are in their standard state) is called its *standard electrode potential* $E^{\circ}_{half-cell}$. Conventionally, $E^{\circ}_{half-cell}$ is written for *reduction* reactions; for instance, the reduction half-reactions for our cell are

$$\begin{aligned} \mathrm{X}^{+} + \mathrm{e}^{-} &\rightarrow \mathrm{X} \qquad E^{\circ}_{anode} \\ \mathrm{Y}^{+} + \mathrm{e}^{-} &\rightarrow \mathrm{Y} \qquad E^{\circ}_{cathode} \end{aligned}$$

Recall that the overall cell reaction is the sum of both half-reactions, and it involves the oxidation of X at the anode, not its reduction. Since electrons flow from the anode to the cathode, the cathode must have a more positive $E^{\circ}_{half-cell}$ than the anode; therefore, for every voltaic cell,

$$E^{\circ}_{cell} = E^{\circ}_{cathode} - E^{\circ}_{anode}, \tag{2.1}$$

which, by definition, must always be positive for a spontaneous process. It's important to note that $E^{\circ}_{cathode}$ and E°_{anode} are relative quantities, and they are usually measured with respect to some *reference* electrode. Most thermodynamics and physical chemistry textbooks have these values, typically reported with respect to the standard hydrogen electrode (SHE); but, irrespective of the reference electrode with respect to which *both* $E^{\circ}_{cathode}$ and E°_{anode} are quoted, the value of E°_{cell} remains the same. The easier it is for a material to lose electrons, the more negative $E^{\circ}_{half-cell}$ is.

The Gibbs free energy of a spontaneous reaction is negative, i.e., $\Delta G < 0$, and we have just seen that the E°_{cell} is always positive for a spontaneous reaction; therefore,

$$\Delta G \propto -E_{cell}.$$

Since ΔG gives the maximum work a system can do on its surrounding at constant pressure, and we know that electrical work is the product of charge and potential, then the amount of charge driven is the constant of proportionality. One mole of electrons has a charge of about 96,485 C, which is the so-called *Faraday constant*, denoted F; we can thus write that

$$\Delta G = -nFE_{cell}, \tag{2.2}$$

where n is the number of mole of electrons involved in the redox process. In our case, it's one in both electrodes. If the cell in question has all its components in the standard state, then Equation 2.2 is

$$\Delta G^{\circ} = -nFE^{\circ}_{cell}.$$

Moreover, there's a link between $DeltaG^\circ$ and the *equilibrium constant* K[8]:

$$\Delta G^\circ = -RT \ln K, . \tag{2.3}$$

where R is the universal gas constant (8.314 J/mol.K) and T is the temperature. On equating 2.2 and 2.3, and making E°_{cell} the subject of formula, we yield

$$E^\circ_{cell} = \frac{RT}{nF} \ln K \tag{2.4}$$

In practical batteries, the reactant concentrations are very far from standard-state values; how then are we to determine the value of E_{cell}, the cell potential under nonstandard conditions? A fundamental result of thermodynamics is that ΔG equals the sum of ΔG° (the free energy change when the system moves from standard-state concentrations to equilibrium *plus* $RTlnQ$ (the free energy change when the system moves from nonstandard- to standard-state conditions)[35, 37]:

$$E_{cell} = E^\circ_{cell} + RT \ln Q, \tag{2.5}$$

where Q is called the *reaction quotient*. For a reversible reaction $\mathrm{aA + bB + \cdots \underset{k_{rev}}{\overset{k_{fwd}}{\rightleftharpoons}} cC + dD + \cdots}$ at *non*equilibrium conditions, $Q = \frac{[\mathrm{C}]^c[\mathrm{D}]^d\ldots}{[\mathrm{A}]^a[\mathrm{B}]^b\ldots}$[9]. Substituting 2.2 into 2.5 and rearranging to make E_{cell} the subject of formula, we yield

$$E_{cell} = E^\circ_{cell} - \frac{RT}{nF} \ln Q. \tag{2.6}$$

This is the famous *Nernst equation*[10]. Thus, from the overall cell reaction of our own hypothetical cell (see 2.2.1), $Q = \frac{[\mathrm{X}^+]}{[\mathrm{Y}^+]}$. Only species whose concentrations can vary are included in determining Q; therefore, the pure solids are not included. With the Nernst equation, we can write how the cell potential of our hypothetical battery will vary with the concentration of the species:

$$E_{cell} = E^\circ_{cell} - \frac{RT}{nF} \ln Q = E^\circ_{cell} - \frac{RT}{nF} \ln \frac{[\mathrm{X}^+]}{[\mathrm{Y}^+]}. \tag{2.7}$$

[8] For a reversible reaction $\mathrm{aA + bB + \cdots \underset{k_{rev}}{\overset{k_{fwd}}{\rightleftharpoons}} cC + dD + \cdots}$ at equilibrium, $K = \frac{k_{fwd}}{k_{rev}} = \frac{[\mathrm{C}]^c[\mathrm{D}]^d\ldots}{[\mathrm{A}]^a[\mathrm{B}]^b\ldots}$, where k_{fwd} and k_{rev} are the rate constants for the forward and reverse reactions, respectively.

[9] $Q = K$ *only at equilibrium!*.

[10] A clarification about this is in order. For accuracy, the Nernst equation is expressed in activities of components $a_i = \gamma_i \frac{[i]}{[i^\circ]}$, not their concentrations, where γ_i is the *activity coefficient*. Because it's typically difficult to determine the activities, concentration is used and the potential takes a new value, the *formal potential* E'_{cell}. These values are usually more or less close, so this difference is typically ignored; besides, it doesn't do much to the understanding of the concepts presented here.

This result is vary important, and it accounts for why the voltage of a battery reduces with usage. Some conclusions can be drawn from Equation 2.7:

- When [X^+] > [Y^+], $Q > 1$ $\ln Q > 0$, and $E_{cell} < E^\circ_{cell}$.
- When [X^+] < [Y^+], $Q < 1$ $\ln Q < 0$, and $E_{cell} > E^\circ_{cell}$.
- When [X^+] = [Y^+], $Q = 1$ $\ln Q = 0$, and $E_{cell} = E^\circ_{cell}$.

Figure 2.5 shows how the cell potential varies for an overall reaction $\mathrm{Zn(s)} + \mathrm{Cu^{2+}(aq)} \rightarrow \mathrm{Zn^{2+}(aq)} + \mathrm{Cu(s)}$ with initial concentration values [Zn^{2+}]=$1.0 \times 10^{-4} M$ and [Cu^{2+}]= $2.0 M$ at 293.15 K: As expected from Equation 2.7, the plot is linear with $\ln Q$, decreasing as

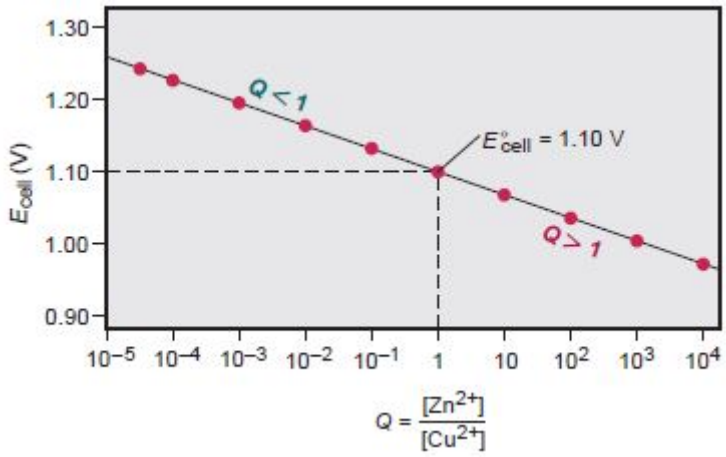

FIGURE 2.5: Cell potential variation for Zn^{2+}/Cu^{2+} (Adapted from [37]).

Q (or [Zn^{2+}]); at some point, Q will be so high that $\frac{RT}{nF} \ln Q$ equals E°_{cell}, causing the cell voltage to be zero. Zero cell voltage implies the overall cell reaction is at equilibrium; at this point, we say the battery is "dead," but it should be possible to increase the potential of a rechargeable battery (close) to its initial value by applying current. Figure 2.6 shows the way potential varies during a full charge-discharge cycle for a LIB [34]; the voltage induced are due to periodic small current pulses slowly applied at the standard state. When there's no external load in our circuit, i.e., when no current is flow, the potential measured is called the *open-circuit voltage* (E_{ocv}). It's obvious that this is the maximum voltage of the cell under specific conditions. Once a current begins the flow, the potential measured will be less than this value for reasons we shall see next.

c. Polarization and internal impedance

Recall that ΔG is the maximum electrical energy a cell can provide and it's related to E_{cell} through Equation 2.2. It would be desirable that all of ΔG be converted to electrical work; however, this is not possible due to polarization once current i begins to flow through the

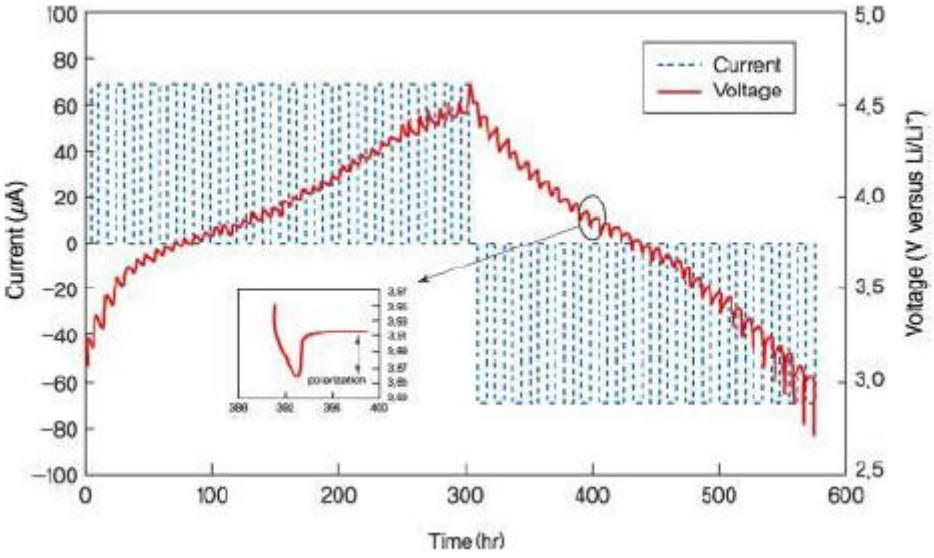

FIGURE 2.6: Charge-discharge voltage of a LIB and OCV profile [34].

electrodes once a load is connected. The losses due to polarization once current begins to flow are *activation polarization*, which drives the electrochemical reaction at the electrode surface, and *concentration polarization*, which arises from the concentration differences of the reactants and products at the electrode surface and in the bulk as a result of mass transfer; these polarizations consume part of the total energy and are given off as heat, making it impossible to attain the theoretical energy value. The polarization is quantified by the *overpotential* η, which is the difference between the actual potential measured E_{cell} and E_{ocv}:

$$\eta = E_{cell} - E_{ocv}. \tag{2.8}$$

The relationship between i and η is [36]

$$i = i_{\circ} exp \frac{-\alpha F \eta}{RT}, \tag{2.9}$$

where $i_{\circ}$ is the current when η is zero, and α is the *transfer coefficient* ($\alpha \approx 0.5$ [35]). Figure 2.7a shows the variation during charge and discharge.

In addition to polarization, *internal impedance* reduces the cell voltage (or energy) from the theoretical value; it's called *ohmic polarization* or iR *drop* and, as its name suggests, its value is proportional to the current drawn from the cell. The total impedance is the sum of the ionic resistance of the electrolyte, the electronic resistance of the active mass, the current collectors, contact resistance, etc. When a cell is connected to an external load, the cell voltage, accounting for all factors that reduce it is [36]

$$E_{cell} = E_{ocv} - [(\eta_{ct})_a + (\eta_c)_a] - [(\eta_{ct})_c + (\eta_c)_c] - iR_i, \tag{2.10}$$

where $(\eta_{ct})_a$ and $(\eta_{ct})_c$ are the activation polarization or charge-transfer overpotential at the anode and cathode, respectively, and $(\eta_c)_a$ and $(\eta_c)_c$ are the concentration polarization at anode and cathode[11], respectively, and R_i is the internal cell resistance. All of them are related to the current supplied, albeit in more complex ways than the iR drop; at low currents, their effects are minimal and we attain a cell potential close to E_{ocv}, thereby delivering close to the theoretical energy value. Figure 2.7b shows the variation of cell potential and current.

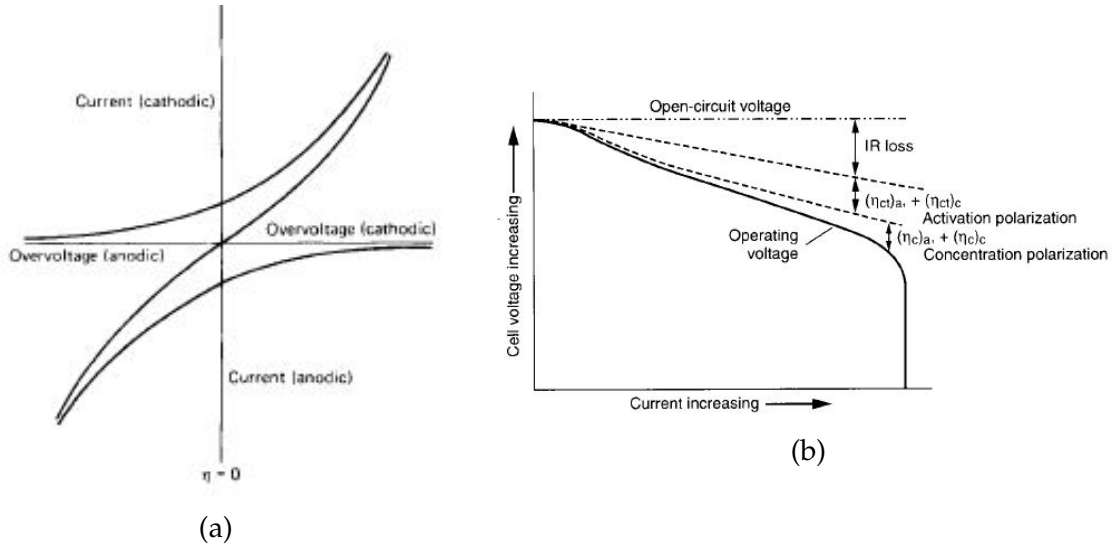

FIGURE 2.7: (a) Current-overpotential relationship and (b) cell polarization as a function of operating current [36].

d. Current

Current is the rate of flow of electric charges; because the flowing charges result from electrochemical reactions, the current must be related to the rates of these reactions. The rates of electrode reactions depend on the rates of electron transfer and of diffusion[12] of electroactive species between the electrolyte and electrode. Like in all chemical reactions, the slower rate is the limiting rate. Let's consider the cathode of our hypothetical cell, this time assuming that it involves n electrons; the electrode (half-cell) reaction occurring there, as we have seen, is

$$\mathrm{Y} + \mathrm{ne}^- \underset{\mathrm{k_{rev}}}{\overset{\mathrm{k_{fwd}}}{\rightleftharpoons}} \mathrm{Y}^{n-}, \tag{2.11}$$

and the net reaction rate is

$$v_{net} = v_{fwd} - v_{rev} = \frac{i}{nF} \tag{2.12}$$

[11] That is, resulting from the difference between the concentrations of species at the electrode surface and bulk of the electrolyte.

[12] Convection and migration are other possibilities, but they are negligible compared to diffusion [35].

At equilibrium, when the rates of forward and backward reactions are the same, the net rate is zero and the current is zero, confirming what we have seen earlier.

e. Capacitance of an electrode

The foregoing treatment is on the basis that there's no thermodynamic constraint on charge transfer between electrodes and the electrolyte; charge transfer results in redox processes, and, since they are governed by Faraday's law, charge-transfer processes are called *faradaic processes*. There are conditions under which charge transfer doesn't occur, perhaps due to thermodynamic or kinetic constrains; however, other processes such as adsorption or desorption can occur; these processes, too, can cause external current to flow – at least, transiently – when cell conditions change. Because they are not due to charge transfer, and hence don't follow Faraday's law, they are called *nonfaradaic processes*. In all cell operations, both processes occur; so, in treatment of electrochemical data, the contribution of nonfaradaic processes should be accounted for.

There are certain electrodes in which no charge-transfer processes occur – or are negligible – over a wide potential range; they are said to be *ideal polarizable electrodes* (IPE). Since charges do not cross the IPE interface when a potential is applied, they behave like capacitors, storing charges at the electrode-solution interface. Recall that the capacitance of a capacitor C with stored charges q at an interface under a potential difference of E is

$$C = \frac{q}{E}. \tag{2.13}$$

When a potential is applied across a capacitor, charges will accumulate on the metal face until Equation 2.13 is satisfied. The current flow due accumulation of charges is the *charging current*.

The electrode-solution interface has been proven experimentally to behave like a capacitor: at every potential, there exists a charge q^M on the electrode and a charge q^S in the solution. The signs of these charges depend on the potential across the interface and composition of the solution; however, $q^M = -q^S$ always. The charges on the electrode (as excess or deficiency of electrons) reside in a very thin layer of the metal surface (<0.1 Å), while the charges in the solution is an excess of cations or anions [35].

The whole array of charged species existing in the electrode-solution interface is called the *electrical double layer*. Figure 2.8 shows the structure of the electrical double layer[13]; at a given potential, the electrode- solution interface is characterized by a double-layer capacitance C_d, typically in the range of 10 to 40 $\mu F/cm^2$ [35]. Unlike real capacitors,

[13]IHP and OHP stand for the inner and outer Helmholtz plane, respectively. They correspond to the loci of the specificically adsorbed ions.

however, whose capacitances are independent of the voltage across them, C_d is often dependent on potential.

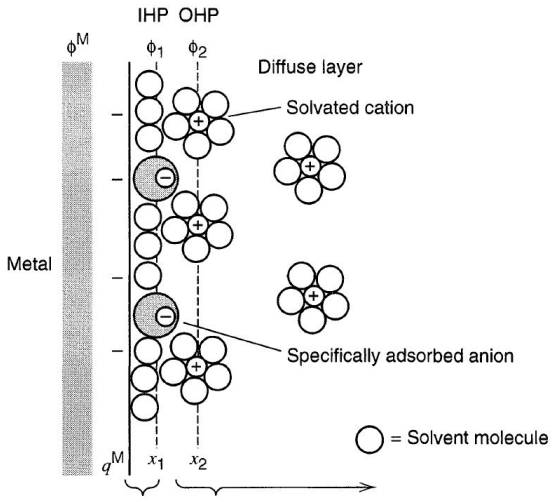

FIGURE 2.8: Model of the electrical double layer [35].

Finally, perturbations on the double layer results in different evolutions of the dependent variable(s) in question. We shall see in Section 2.2.3 that battery performance are experimentally evaluated by cycle tests. For a cycle test done at constant current, i.e., galvanostatically (which is typically the case), a *current step* is imposed on the system; in addition to the voltage variation due to redox reactions in a battery, iR drop, polarization, etc., there's also a capacitive effect. The potential[14] due to the capacitive effect is

$$E_d = \pm i(R_s + t/C_d), \tag{2.14}$$

where R_s is the overall resistance of the circuit, t is the charging time (which is inversely proportional to the applied current); it's obvious then that the capacitive effect increases at lower current. For other scenarios, see Ref. [35].

2.2.2 Battery Characteristics

In the previous subsections, we saw certain parameters used to characterize batteries, *viz.*, Equations 2.1, 2.2, 2.8, etc. Now, we shall consider some others that are rather more definitional than stemming from thermodynamic considerations.

- **Capacity**: The capacity of a battery is the total amount of charge delivered when completely discharged under given conditions. The *theoretical* capacity C_T is the

[14] The positive sign is for the charging current, while the negative is for discharge; thus the potential is added during charging and reduced during discharge.

total amount of electricity evolved from the electrochemical reaction; it depends on the amount of material present, and its unit is the C or Ampere-hour Ah. Since Faraday's number amount of charge F (96,487 C or 26.8 Ah) is delivered by one mole of electrons, then the C_T is defined as

$$C_T = nF. \tag{2.15}$$

The practical capacity C_P of batteries is usually much smaller than C_T, because not 100 % of the reactants are converted in electrochemical reactions. Since the theoretical capacity is an extensive property, it's typically reported per mass (Ah/g), volume (Ah/cm^3), or area (Ah/cm^2) of active materials; that way, materials can be easily compared, irrespective of the amount available. Because the number of moles of electrons is used in determining the C_T, the gravimetric theoretical capacity can be easily by dividing by the molar mass.

Moreover, as the charge or discharge rate (i) increases, the practical capacity further reduces due to the iR drop. The charge or discharge rate is denoted by C_{rate}; to define it, we should see that the time required to practically charge or discharge a battery, t, say, is

$$t = \frac{C_P}{i}$$

with t is in hours. Hence, the C_{rate} is quoted as "C/t" rate; for instance, if t is 1, we say it's "1C" rate, meaning the total capacity is charged or discharged in one hour; if t is 2, it's C/2, meaning half of the capacity is charged or discharged in an hour; if t is 0.5, then it's 2C, meaning the full capacity is discharged in half an hour, or its full capacity is discharged twice in an hour, and so on.

- **Energy density**: This is a very important battery characteristic: it's the amount of energy stored per unit mass or volume or area of active material. Recall that Equation 2.2 gives the relationship between the cell potential and the maximum energy that can be delivered by n mole of reactants. It should be obvious that the actual energy is less than the maximum due to overpotential when current starts to flow, as we have already seen. Accounting for overpotential, the practical energy is:

$$\epsilon_p = -nF(E_{ocv} - \eta) \tag{2.16}$$

Thus, we can determine the energy density by dividing this value by the molar mass of reactants involved in the reaction:

$$\text{Energy density} = \frac{\text{Energy}}{\text{molar mass}} = \frac{-nF(E_{ocv} - \eta)}{M} = C_P(E_{cell} - \eta) \quad \text{in Wh/g.} \tag{2.17}$$

1 Wh is 3600 J.

- **Power**: The power of a battery is the energy that can be derived (or discharged) per unit of time: it's the product of current i and electric potential. Again, the practical power, on accounting for overpotential, is

$$P = \frac{\text{energy density}}{\text{charge or discharge time}} = i(E_{ocv} - \eta). \tag{2.18}$$

  When current increases, the power increases until a maximum value, beyond which it begins to drop, because of reduction in E_{ocv} (or increase in η due to polarization). Polarization is related to the diffusion of ions and the internal resistance of a battery [34]. To improve power, it is necessary to enhance the diffusion rate of ions and the electrical conductivity.

- **Cycle life**: Cycle life is the number of charge-discharge cycles a battery can achieve before its capacity is depleted. In general, it depends on many factor, like the stability of electrodes, concentration of ions in electrolyte, conditions under which the battery is used, even aspects relating to battery packaging, etc. [34].After N charge-discharge cycles, the *capacity retention* is C_N/C_1, where C_1 is the capacity after the first cycle and C_N is the capacity after N cycles. The *relative capacity decrease* is $(C_1 - C_N)/C_1$. Finally, battery cycle life is strongly affected by the *depth of discharge* (DOD), which is the percentage of the original capacity that has been discharged; typically, cycle life is increased if DOD is small.

2.2.3 Electroanalytical Techniques

In this section, a cursory explanation of some relevant electroanalytical techniques, *viz.* cycling test and cyclic voltammetry, will be given, as they are relevant to understanding discussions in subsequent sections.

Cycle test

Cycle tests are done to simulate the behaviour of batteries under predefined conditions. In this test, a certain input parameter is imposed to charge and discharge the battery multiple times, while monitoring the evolution of the battery's capacity, cell potential, etc., as these variables are dependent on the charge-discharge parameters. Typical charge-discharge conditions are constant power, constant current, and constant external resistance [34]. Depending on the output variables of interest, other constraints may be imposed.

Figure 2.9a is a plot of some batteries' voltages as functions of capacity (which is basically time[15]) when discharge is done at constant current. The battery voltage when discharge is complete is called the *cutoff voltage*. In the case of curve I in Figure 2.9a, the battery voltage is hardly influenced by reactions occurring within the battery during discharge; Curve II shows two flat regions due to change in the reaction mechanism; In curve III, the reactants, products, and internal resistance of the battery are continuously changing throughout the discharge process. In addition, Figure 2.9b shows how potential varies for different current densities. It should be clear by now that the decrease in potential with increase in current is due to polarization. Finally, although the effects of temperature hasn't been emphasized thus far, it has an immense effect on the performance of batteries. Recall that we saw in Section 2.2.1 that rate of electrode reactions is dependent on the diffusion of chemical species; all things being equal, diffusion increases with temperature; thus, at higher temperature, we should expect higher voltage at high temperatures. This is indeed what's observed. Figure 2.9c accentuates this. However, at high temperature, self-discharge or some side reactions may be initiated, which can have adverse effects on a battery's performance.

Cyclic voltammetry

Cyclic voltammetry (CV) is perhaps the most popular and versatile electroanalytical technique commonly employed in the study of electrode processes. It provides information about a host of parameters, which will be perfunctorily presented hereafter; however, for a detailed treatise on the theory of cyclic voltammetry, see Refs. [39] and [40].

Simply put, a CV is done by applying a linearly changing voltage (a voltage ramp) to an electrode according to

$$E = E_i \pm \nu t \tag{2.19}$$

where E_i is the initial voltage, nu is the scan rate (in V/s), and t is the time. The voltage variation with time is shown in Figure 2.10a; Figure 2.10b shows examples of curves one can get for different electrodes that undergo Nernstian process, i.e., whose voltage evolution follows Equation 2.6. These curves are called *cyclic voltammograms*; we shall now use Fig 2.10c to state some characteristics of a CV curve.

The *peak currents* $i_{p,i}$ results from a surge in the diffusion of ions from the bulk of the electrolyte onto the electrode surface after all the ions initially on the electrode surface are consumed (resulting in higher concentration gradient); it can be shown [35, 36, 41] that the peak current is

$$i_{p,i} = \pm \frac{0.447(Fn)^{3/2} A C_\circ (Dv)^{1/2}}{(RT)^{1/2}} \tag{2.20}$$

[15] $C = it$!

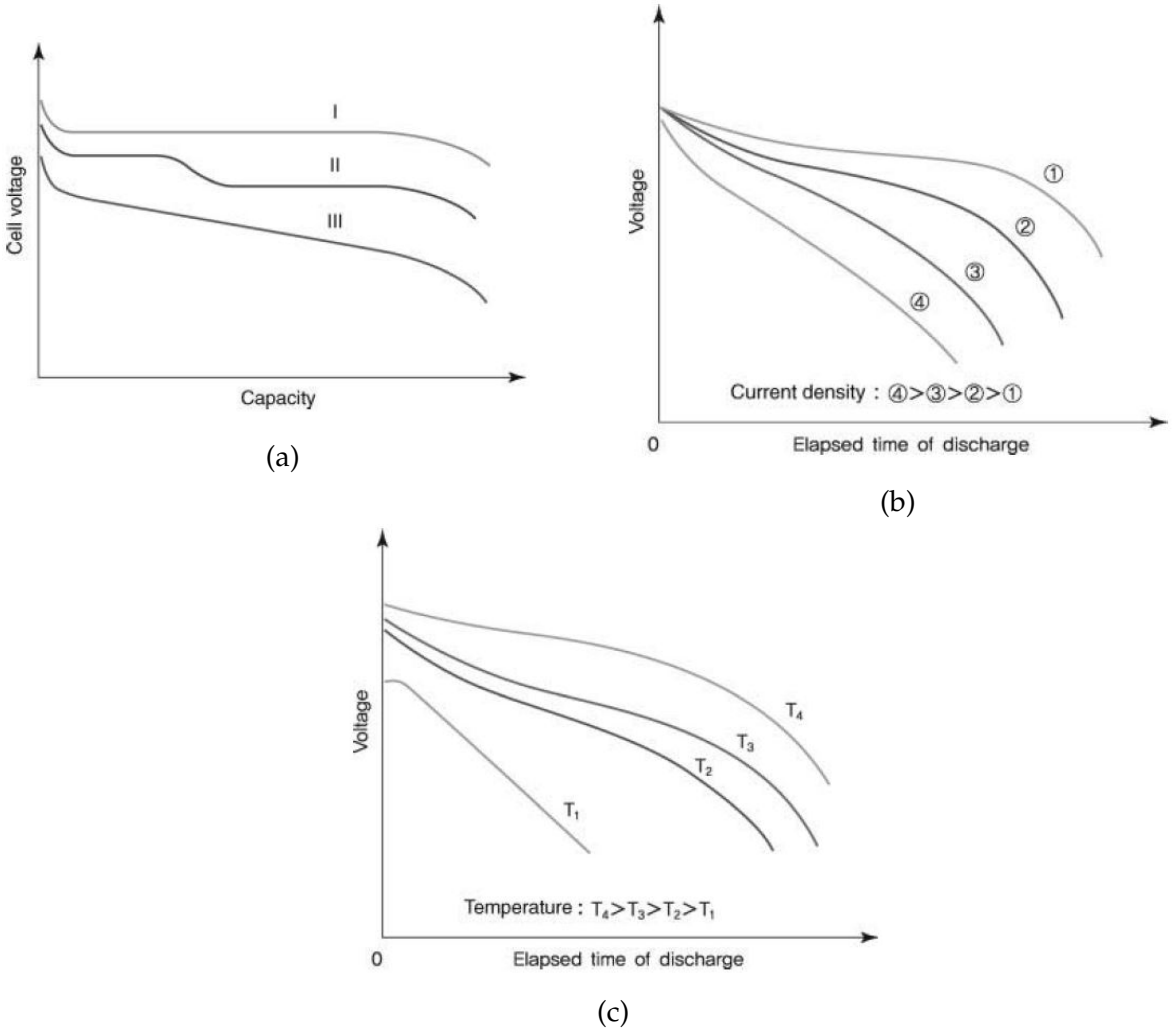

FIGURE 2.9: (a) Discharge curves of different electrochemical reactions (b) Effect of current density on battery voltage (c) Effect of temperature on battery voltage [34].

where A is the area of the electrode, $C_\circ$ is the ion's bulk concentration in the electrolyte, and D is the diffusivity of the ions; it's obvious that by merely doing CV, transport properties can be determined[16]. Although we might prefer high scan rates in order to have larger currents, we increase the capacitive effect at the electrode-electrolyte interface, which may overshadow the actual redox capacitance. Typically, this effect is negligible for scan rates below 1 mV/s [36].

Furthermore, midway between the peak potentials $E_{1/2}$ is a very good approximation of the electrode potential; thus, in practice, $E_{1/2}$ is used as the potential for a reversible electron transfer reaction. The separation of the peaks results from the need of the ions to diffuse to and from the electrode.

[16] "$\pm$" is added to the equation to give the reader leeway in the choice of sign convention for the electrodes. Also, in some publications or books, the index of n and F is $1/2$, not $3/2$; this results from the fact that different numerical methods are used to derive the relationship; but since they are constants, it's inconsequential to data analyses, as we can still monitor the variables of interest.

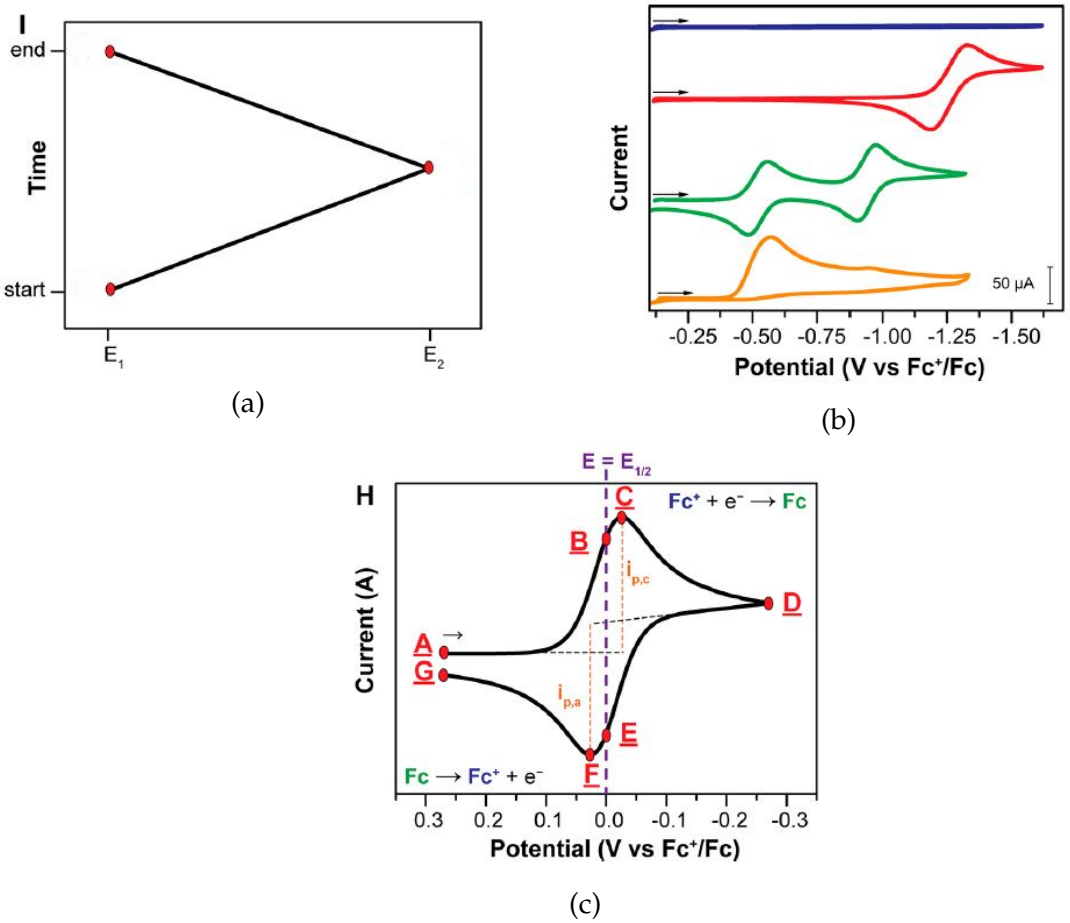

FIGURE 2.10: (a) Applied potential as a function of time for a generic cyclic voltammetry experiment (b) Sample CVs for various Nernstian reactions (c) CV showing salient points (All adapted from [41])

Finally, we can also determine the nature of the reversibility of an electrode process by the *peak-to-peak separation* ΔE_p. For a *reversible* process,

$$\Delta E_p = \frac{2.3RT}{nF}. \tag{2.21}$$

For a *quasi-reversible process*, the peaks are not sharp and are larger than the value given by 2.21. Of course, a completely *irreversible* process would have a peak in only a scan direction.

2.2.4 Primary (Nonrechargeable) Batteries: Leclanché Cell

Section 2.2.1 details the thermodynamic principles required to understanding the working of a battery. But, as every engineer knows, cognizance of scientific principles alone is not enough to get a device functioning as consumers would hope: many limitations still exist, like the cost of production, environmental concerns, the ability of a device to withstand

extreme conditions, and so on. However, it's sufficient to comprehending the working of *real* devices and why certain engineering choices are made. Let's now consider the Leclanché cell.

Leclanché cells, a type of zinc-carbon cells, are the most commonly used primary batteries worldwide; they are cheap, mainly used in portable radios, flashlights, and other moderate light drain devices. It was initially created because of the need to provide a more reliable and easily maintained power source for telegraphic offices [36]. It uses a zinc anode, manganese dioxide cathode, electrolyte of ammonium chloride and/or zinc chloride in water, and starch paste separator. Carbon is usually mixed with manganese dioxide to improve conductivity and retain moisture. As the cell is discharged, the zinc is oxidized and manganese dioxide is reduced. Its overall cell reaction is

$$\mathrm{Zn} + 2\,\mathrm{MnO_2} \longrightarrow \mathrm{ZnO \cdot Mn_2O_3}. \tag{2.22}$$

In spite of the fact that Leclanché cells have existed for a long time, there are still some disputes as to the actual electrode reactions occurring [42]; this is mainly because its cathode MnO_2 is a non-stoichiometric oxide, and is thus better represented as MnO_x, where x is typically 1.9+. Several factors affect the efficiency of the reactions within the cell: cell geometry, discharge rate, discharge temperature, depth of discharge, diffusion rate, type of MnO_2 used, etc. Theoretically, its specific capacity is 224 Ah/kg, based on the simplified cell reaction; however, because of the complex nature of its reactions, its capacity never exceeds 96 Ah/kg [36].

Figure 2.11 shows the cutaway of various geometries on the market. In the cylindrical battery, the zinc serves as both the cell case and the anode; the carbon rod is both the current collector and positive electrode. The inside-out cylindrical construction (Figure 2.11b) does not use zinc anode as the container, which makes it more efficient, and less likely to leak. The flat cell design allows for more cathode space, because the package and electrical contacts are minimized; this results in a doubling of the volumetric energy density compared to the cylindrical construction. The typical discharge curve of a Leclanché cell discharge is shown in Figure 2.11d.

2.2.5 Secondary (Rechargeable) Batteries: Lithium-ion Batteries

Lithium-ion batteries (LIBs) are the most popularly used rechargeable batteries – they are being used almost exclusively in mobile phones, laptops and electric vehicles (EVs) [33]. This results from their unparalleled energy and power density among rechargeable batteries due to their chemical nature: For one, lithium has the most negative electrode potential of all elements, implying that, by its nature alone, it should be involved in a battery with the best cell potential; for another, Li is the third least dense element and

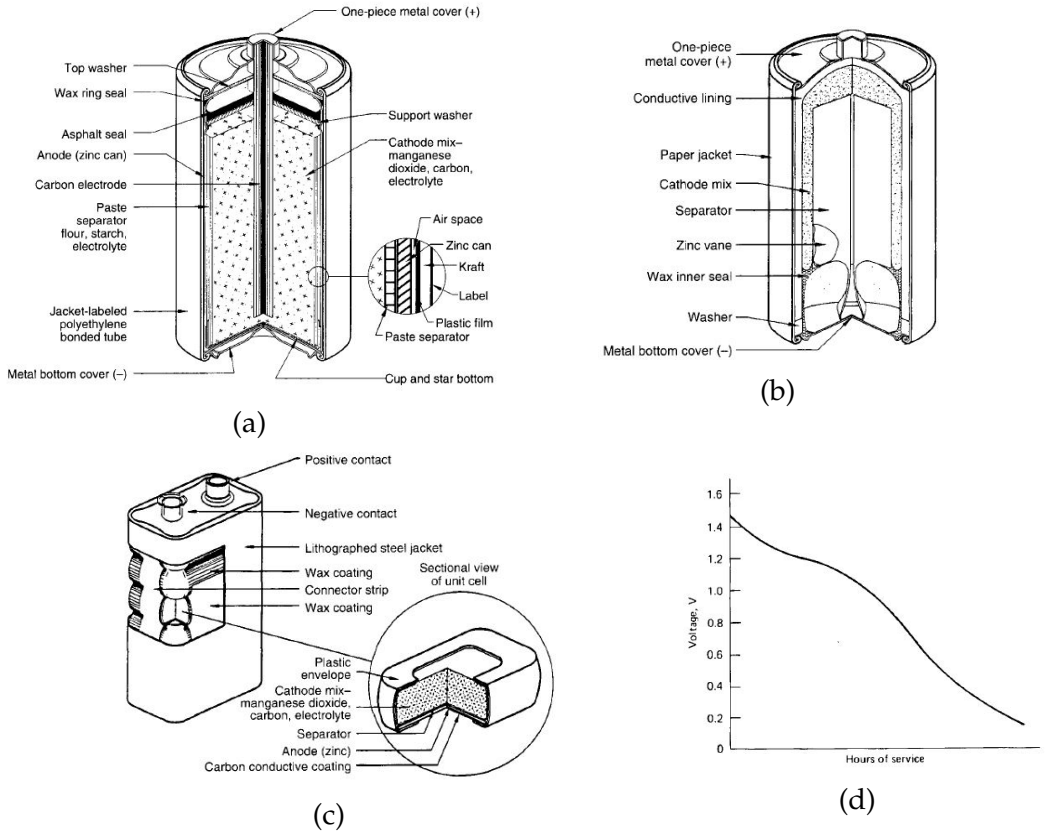

FIGURE 2.11: Typical cutaway views of (a) Cylindrical Leclanché battery, (b) Cylindrical Leclanché battery – inside-out construction, (c) Leclanché flat cell, (d) Typical discharge curve [36].

has one of the smallest ionic radii of any single charged ion, making it possible to have batteries therefrom with high gravimetric and volumetric capacity and power density. Finally, although multivalent ions have larger capacity per ion, the extra charge makes them diffuse more sluggishly, limiting their performance, and making it even more difficult for them to overthrow Li as choice metals for batteries.

Basically, a LIB consists of electrodes connected ionically by Li^+-containing electrolytes, electrically isolated from each other by a separator, which is typically a microporous insulating polymer that allows for exchange of Li^+ between the electrodes but not electrons, and electrically connected externally to a load. Electrolytes can be liquid, gel, polymer, and ceramic [43]. Figure 2.12 illustrates the working principle of LIBs; the principle is the same for every one on the market – the only differences are in the materials of construction.

The electrode materials in Figure 2.12 are common among LIBs, and batteries are typically assembled in the discharged state [43]; during charging, $LiCoO_2$ (lithium-cobalt-oxide or LCO) is "forced" to release electrons by an external current to carbon (in the form of graphite, C) through the external connection, which is also accompanied by movement of Li^+, through the electrolyte, from LCO to C. These accumulated charges at

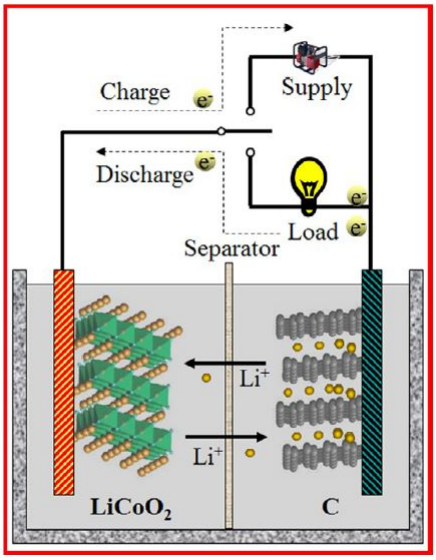

FIGURE 2.12: Illustration of the working principle of a LIB [43].

C is the energy released during discharge: when an external load is connected, electrons flow from C to LCO, also accompanied by the flow of Li^+ through the electrolyte in the same direction [17].

This mechanism of Li^+ shuttling between electrodes is called the "rocking-chair" mechanism [34]. Considering both electrodes, the theoretical capacity of Figure 2.12 can be easily calculated to be around 100 Ah/kg; in practice, however, other materials, like binders, electrolyte, etc., are, in addition, taken into consideration, which reduces this value. With a potential of 4.1 V, its theoretical specific energy is 410 Wh/kg, but in practice, its specific energy 150 Wh/kg [36].

The electrode materials of LIBs undergo three types of reactions with lithium, *viz. insertion*, *alloying*, and *conversion* reactions. Figure 2.13 schematically shows the relative structural changes the electrodes undergo during these reactions.

Materials in which *intercalation* or insertion reactions occur are mostly the cathode materials. LCO (shown in Figure 2.12) is the most common of this family of cathode materials. In order to save cost, another member of the family, $LiFePO_4$ (LFO), has reached commercial stage as a cathode material; when used in conjunction with an anode intercalation compound belonging to the same family, $Li_4Ti_5O_{12}$, it offers advantages of safety, reduced cost, and toxicity [44]. According to Ref. [33], some of the requirements that intercalation compounds of the form $Li_xM_yX_z$ (where M is a transition metal and X is anion) must satisfy are high lithium chemical potential to maximize cell voltage; this implies

[17] I am wary to assign the tag "cathode" or "anode" to either electrode; this is because either electrode can be the cathode or anode, depending on the process it undergoes. The standard in the treatment of galvanic cells is that the electrodes are labelled according to the discharge process; this makes sense, because not all galvanic cells are rechargeable; therefore, in this LIB, C is the anode, since oxidation occurs there during discharge, and LCO the cathode, as it's reduced during discharge.

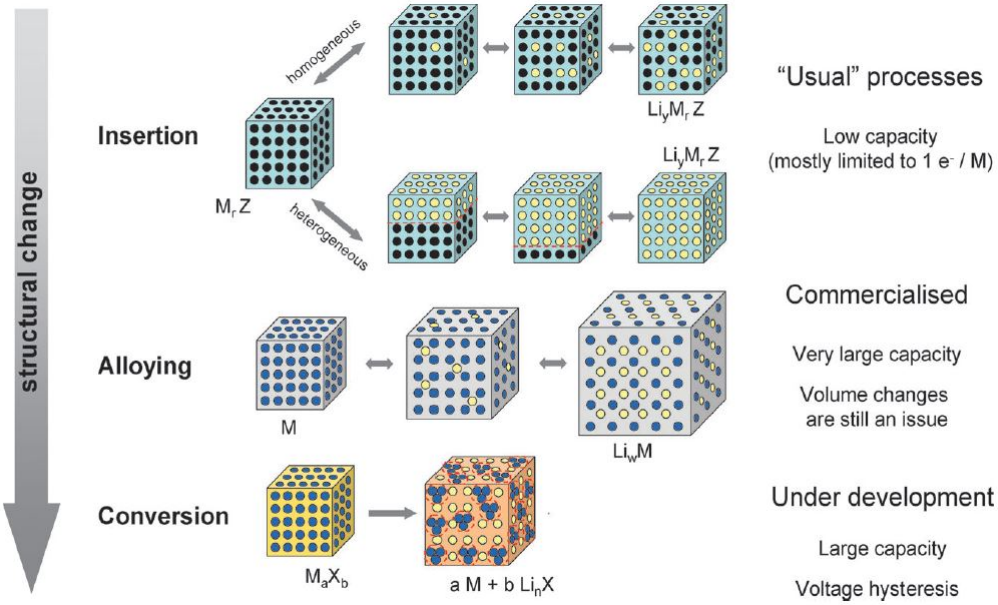

FIGURE 2.13: Schematic representation of different reaction mechanisms in LIB electrode materials; black circles are voids in the crystal structure, blue circles are metal ions, and the yellow circles are lithium ions [44].

that M should have a high oxidation state; it should allow for an insertion/extraction of a large amount of lithium to maximize cell capacity; lithium insertion/extraction should be reversible, and it shouldn't be associated large changes in the structure of the host material, in order provide good cycle life, among others.

Alloying electrodes have very high capacity – as high as 4200 Ah/kg in Si, for instance [45] – but they undergo substantial volume changes during alloying, limiting their use in practical devices. Conversion reaction refers to reactions in which a binary transition metal reacts with lithium. Electrodes that undergo conversion reactions have high energy densities, including those transition metal compounds that have been hitherto disregarded as intercalation compounds due to their low vacancy concentration [46]. The major drawback to conversion reaction electrodes is the presence of large voltage hysteresis during charge and discharge. Figure 2.14 summarizes the average discharge potentials and specific capacities for all types of electrodes.

A host of electrolytes are used in LIBs – liquid electrolytes, solid polymer or gel electrolytes, and inorganic solid electrolytes. Liquid electrolytes suffer from limited temperature range (-20 to 50 °C), loss of capacity, safety problems due to flammability, and relatively low ionic conductivity. Solid polymer, or gel, electrolytes, which is basically polymers embedded with liquid electrolytes, avoids lithium dendritic growth, easily processable, safe, and cheap; Its demerit, however, is that it has low ionic conductivity at low temperature. The use of inorganic solid electrolytes LIB is still in its infancy; the challenge is that, so far, it's been impossible to get a solid electrolyte that simultaneously

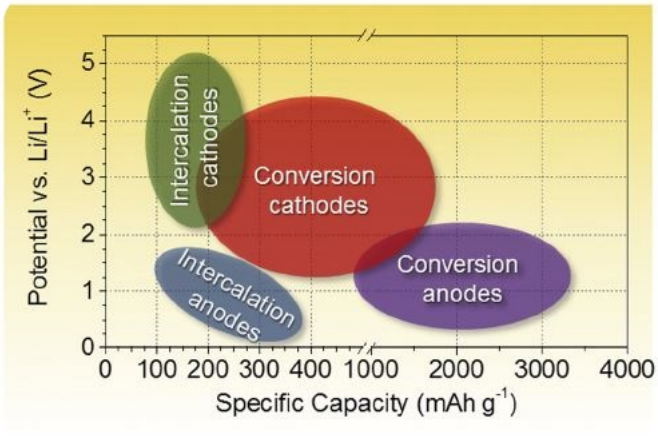

FIGURE 2.14: Overview of the average discharge potentials and specific capacities for all types of electrodes [43].

has good ionic conductivity and electrochemical stability: it's usually one or the other. All solid state electrolytes offer higher thermal stability than liquids, low rate of self-discharge, and ability to operate over a wide temperature range [44].

Finally, Figure 2.15 shows the discharge profiles of intercalation cathodes, conversion cathodes, and some anodes, respectively.

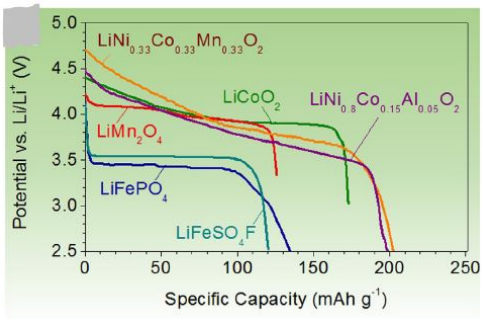

(a)

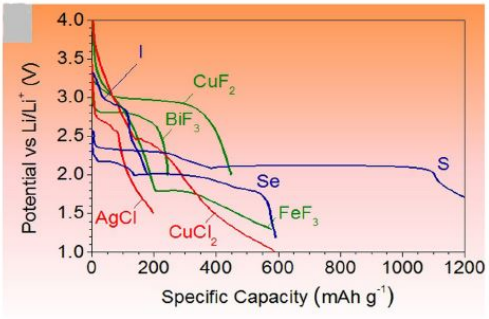

(b)

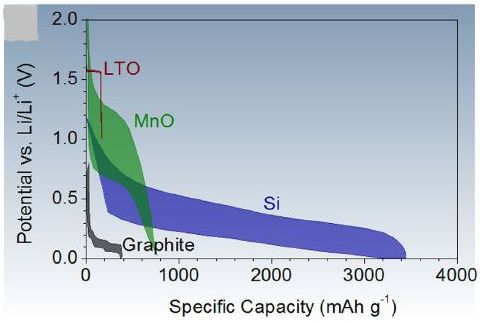

(c)

FIGURE 2.15: (a) Typical discharge profiles of intercalation cathodes (b) typical discharge profiles of conversion cathodes (c) anode charge–discharge profiles at low charge/discharge rates, showing voltage hysteresis. (All adapted from ref. [43].)

2.3 Microbatteries

Batteries that are required for large-surface area-to-volume devices, like those associated with solar cells, smart cards, implantable medical devices, micro-electromechanical systems (MEMS), CMOS backup, etc., are better specified by their areal capacity, i.e., the amount of charge stored in a unit area of the device (in Ah/cm^2). Such batteries are called *microbatteries*; the typical required characteristics are power density of 10^2 – $10^3 \mu W/cm^2$ in the temperature range of -20 – 80 °C, capacity of $10^3 \mu Ah/cm^2$, operating voltage range of 2–3 V, cycle life of 10^4 (especially for aerospace applications), and thickness of no more than 3 mm (including packaging) [47]. The possibility to have batteries at such small scale results from the advantages that using nanostructured battery components and certain architecture confer on them. We now consider them.

2.3.1 Size Effects

In the early twentieth century, Albert Einstein's *chef-d'œuvre*, the theories of *Special and General Relativity* [48], parallelized the ability to think in four dimensions [18] with "genius." This was, perhaps, further bolstered by the fact that Herbert Marcuse used the term "One-dimensional" in a rather derogatory sense to human intellects in his highly influential book *One-Dimensional Man* [49]. But, as even you my dear reader may attest, the mantra in most scientific laboratories, technology workshops, etc., today is "nano." It has now become fashionable among us scientist[19] to speak about reduced dimensions – words like "0D," "1D," "2D" are frequently used – but it's for good reason[20]: nanomaterials offer a wide range of unique chemical, mechanical, electrical, thermal, and optical properties (Ref. [54] is a good review of some of them). In energy storage application, especially as electrode or electrolyte materials, these unique properties are pronounced.

As electrode materials, they offer better accommodation of the strain of ion insertion/removal, improving cycle life; possibility of reactions not possible with bulk materials, making it possible to use novel electrode reactions besides the typical intercalation reaction; higher electrode/electrolyte contact area, leading to higher charge/discharge rates; and short-path lengths for electronic and ionic transport, permitting operation with low

[18] *"Ha, one dimension higher than mere mortals can sense!"*

[19] You need not roll your eyes: of course, I, too, am a scientist!

[20] In so far as I can recall, there've been, at least, four Nobel Prizes relating someway to nanoscience and -technology: the prize in physics to Ruska and Binnig & Rohrer (together) in 1986 "for fundamental work in electron optics, and for the design of the first electron microscope," and "for their design of the scanning tunneling microscope," respectively [50]; the prize in chemistry to Curl, Kroto, and Smalley in 1996 "for their discovery of fullerenes" [51]; the prize in physics to Geim and Novoselov in 2010 "for groundbreaking experiments regarding the two-dimensional material graphene" [52]; and the prize in chemistry to Sauvage, Stoddart, and Feringa in 2016 "for the design and synthesis of molecular machines" [53]. So – to answer the question you're asking yourself – yeah, "nano" is a big deal!

electronic and/or ionic conductivity at higher power. Nevertheless, there are still disadvantages, like an increase in undesirable electrode/ electrolyte reactions due to higher surface area, leading to self-discharge, poor cycling and short cycle life; inferior packing of particles, leading to lower volumetric energy densities unless special compaction methods are developed; and sometimes synthesis might be more complex than for their bulk counterparts [6, 8, 45, 46, 55, 56].

A prominent example is in the use of nanostructured materials as anode. Recall that in Section 2.2.5 we saw that materials that undergo alloying reactions with lithium, e.g., Si, have very high capacity, but their use is limited because they undergo large volumetric changes – 400 % for Si, for example [57] – during cycling, which leads to cracking and pulverization of such materials, hence low cycle lives. It has been proven [57, 58] that use of nanowires circumvents this issue, and there's minimal capacity fade with increasing number of cycles. Figure 2.16 presents some of the cycling properties of Si nanowires.

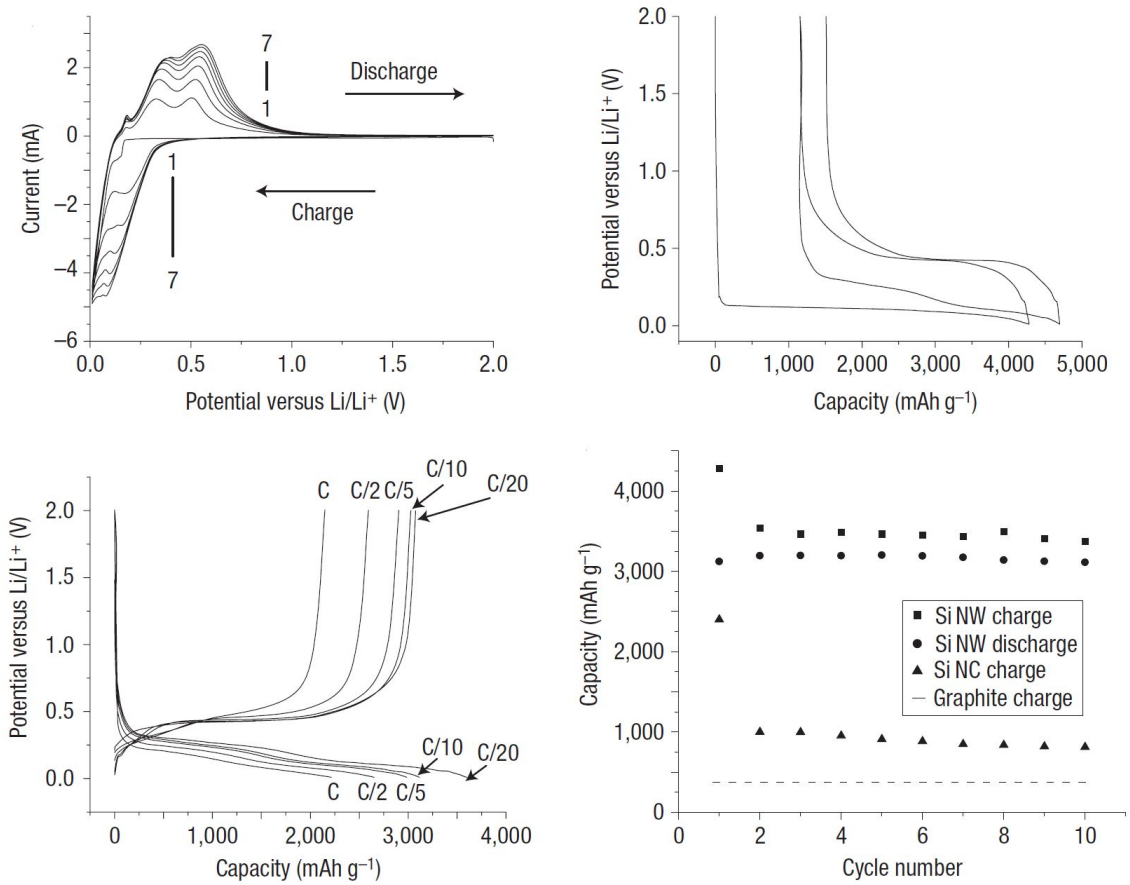

FIGURE 2.16: Cycling performance of Si nanowires (Adapted from Ref. [57]).

Another example of the advantage of nanostructured materials, this time in a cathode material LCO, is shown in Figure 2.17. As size reduces, the substantial increase in charge/discharge rate (power density) is evident. The reader might be tempted to think

that the increase in power density is a result of transition to a predominating capacitive behaviour, but the electric double-layer contribution has been shown to be negligible in such nanocrystalline LCO [59], proving that it's purely a nanosize effect; besides, its cyclic voltammogram (CV) shows the existence of clearly defined redox peaks. The drawback, however, is the loss in capacity, as 2.17 shows.

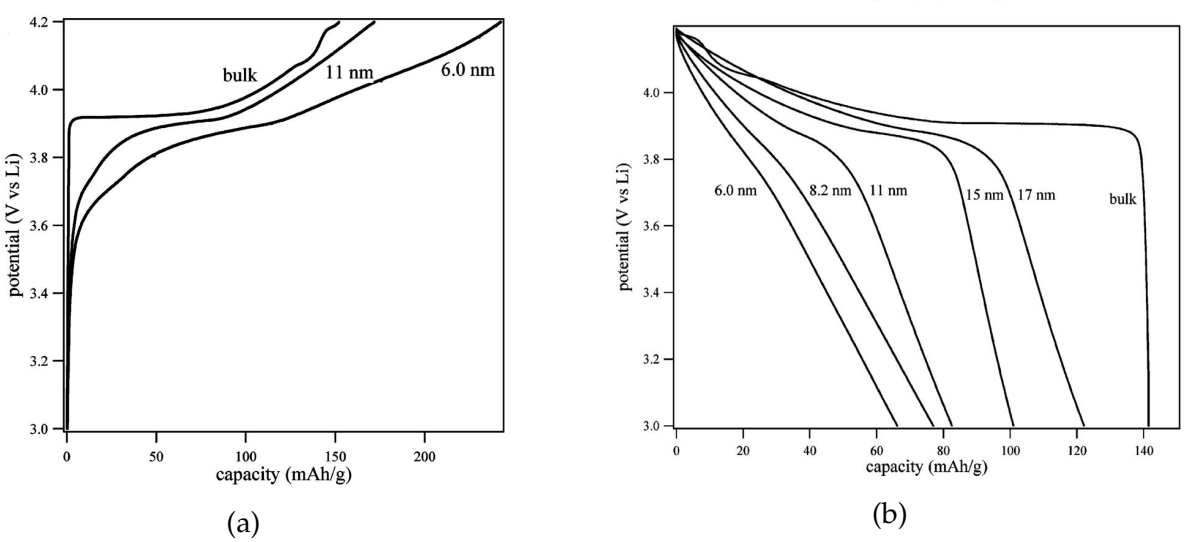

FIGURE 2.17: (a) First charge curves for LCO (bulk, 11 and 6 nm) (b) Second discharge curves for LCO in various size. (Adapted from ref. [59].)

As we have seen, solid electrolytes are particularly interesting for battery applications, as they present many propitious properties, like improved operation safety, ease of fabrication, etc. Polymer electrolytes are the most promising, and the most desirable are those formed by solvent-free membranes [60] – poly(ethylene oxide) (PEO) and a lithium salt $LiPF_6$, for example; however, they have poor ionic conductivities at low temperature, which has prevented their use in many practical batteries till date [44]. It has been shown that dispersing nanoscale inorganic fillers in such polymer electrolytes considerably enhances their ionic conductivities [61].

2.3.2 Architecture Effects

The emergence of solid electrolytes has allowed the possibility to design primary and secondary thin-film microbatteries, with thicknesses varying from the nanometer to micrometer scale. When the thickness of the film is in the nanometer scale, it is said to have a *2D architecture*; within a few micrometers, it's said to be *mesoscopic* [15, 47, 62, 63]. Thin film batteries with thicknesses within the nanometer scale, i.e., the ones of 2D architecture, are very simple, easy to fabricate, cheap and offer all the advantages of nanostructured materials that we saw in Section 2.3.1; however, because they contain very small amounts

of active materials, they can only store and provide a limited amount of energy per unit area, mass, or volume.

Many of such large-surface area-to-volume devices require much more areal capacity than 2D microbatteries can provide. Areal capacity can be enhanced by increasing the thicknesses of components to the mesoscopic scale (to have more materials); but this further increases the diffusion length of ionic species, reducing the power density of the batteries. It's obvious, then, that it's challenging to simultaneously achieve high areal energy and power density in such batteries.

To surmount this challenge, batteries made of *three-dimensional (3D) nanostructures* (called 3D batteries, irrespective of its architecture) are proving to be better alternatives to mesoscopic batteries [9, 13–16]. This is because by using 3D structures on the same footprint area (as a thin film's), we can increase the amount of active materials and still retain the short ion-transport distances associated with nanostructures (in addition to all other advantages of nanostructures). Therefore, with such architecture, high areal energy and power density batteries can be simultaneously attained; moreover, the energy density can be easily tailored by adjusting the height of the 3D nanostructures. Figure 2.18 shows some of the electrode architectures that are being used. The advantage of these architectures is that the inter-electrode distance is shortened, making ions to have to travel much shorter distances, thereby reducing the overall ohmic cell resistance, which ultimately results in improved battery performance [14].

2.3.3 State of the Art

Although thin-film batteries are also microbatteries, only the state of the art in 3D microbatteries will be considered, since it is the interest of this work. In particular, we shall consider one very similar to the 3D battery fabricated in this work[21].

Very recently, a "dispense-print" process, which allows for extreme miniaturization into glass chips and electronic packages, was employed to fabricate a lithium-ion microbattery (active area of 6×8 mm^2) with interdigitated electrodes [64]. Carbon-coated $Li_4Ti_5O_{12}$ was used as the anode, while $LiNi_{1/3}Co_{1/3}Mn_{1/30}$ was used as the cathode; first, either laser ablation or wet-etching chemistry was used to create cavities in a glass substrate, then the electrode materials were prepared in a slurry form and micro-dispensed into the cavities in the substrate. An interdigitated electrode architecture was used that comprised 4 cathode and 5 anode channels arranged in an alternating structure. Figure 2.19a shows the cross-sectional view of the process sequence for the microbattery fabrication and Figure 2.19b shows the finally fabricated battery. The capacities of the resulting batteries ranged from 0.15–0.3 mAh, and several 100 cycles were achieved.

[21] It might interest you to know that that this state of the art battery was published in May 2018. It's literally *the* state of the art.

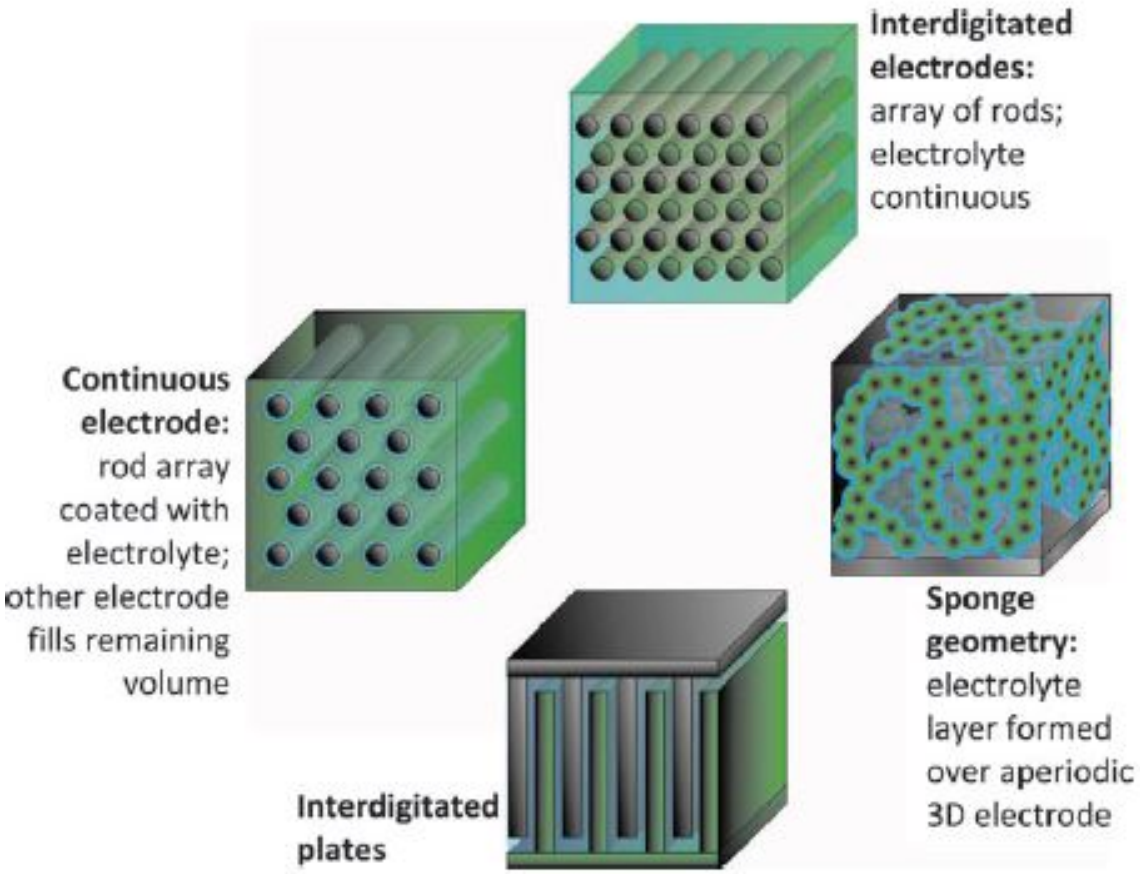

FIGURE 2.18: 3D microbattery architectures (Adapted from Ref. [15]).

2.4 Polyaniline: Electrochemistry and Syntheses

In this section, we consider the science of polyaniline, which belongs to a very interesting class of materials, *viz.* conducting polymers, works on which, in fact, culminated into Heeger, MacDiarmid, and Shrikawa's winning the 2000 Nobel prize in chemistry [65]. Polymers are particularly attractive for battery applications, because of favourable properties, such as high strength-to-weight ratios, toughness, low cost, molecular tailouring of desired propertie, etc. [66]. Appendix A presents the solid-state physics of conducting polymers for an interested reader.

2.4.1 Electrochemistry of Polyaniline

Figure A.7a shows the structure of polyaniline (PAni); the values of n and m[22] correspond to the different intrinsic oxidation states of PAni. In the most stable forms of PAni, the value of n can vary from 0, its fully oxidized state *pernigraniline (PN)*, to 1, its fully reduced state *leucoemeraldine (LM)*. When n is 0.5, PAni is in its most stable form called emeraldine

[22]Note that $m = 1 - n$.

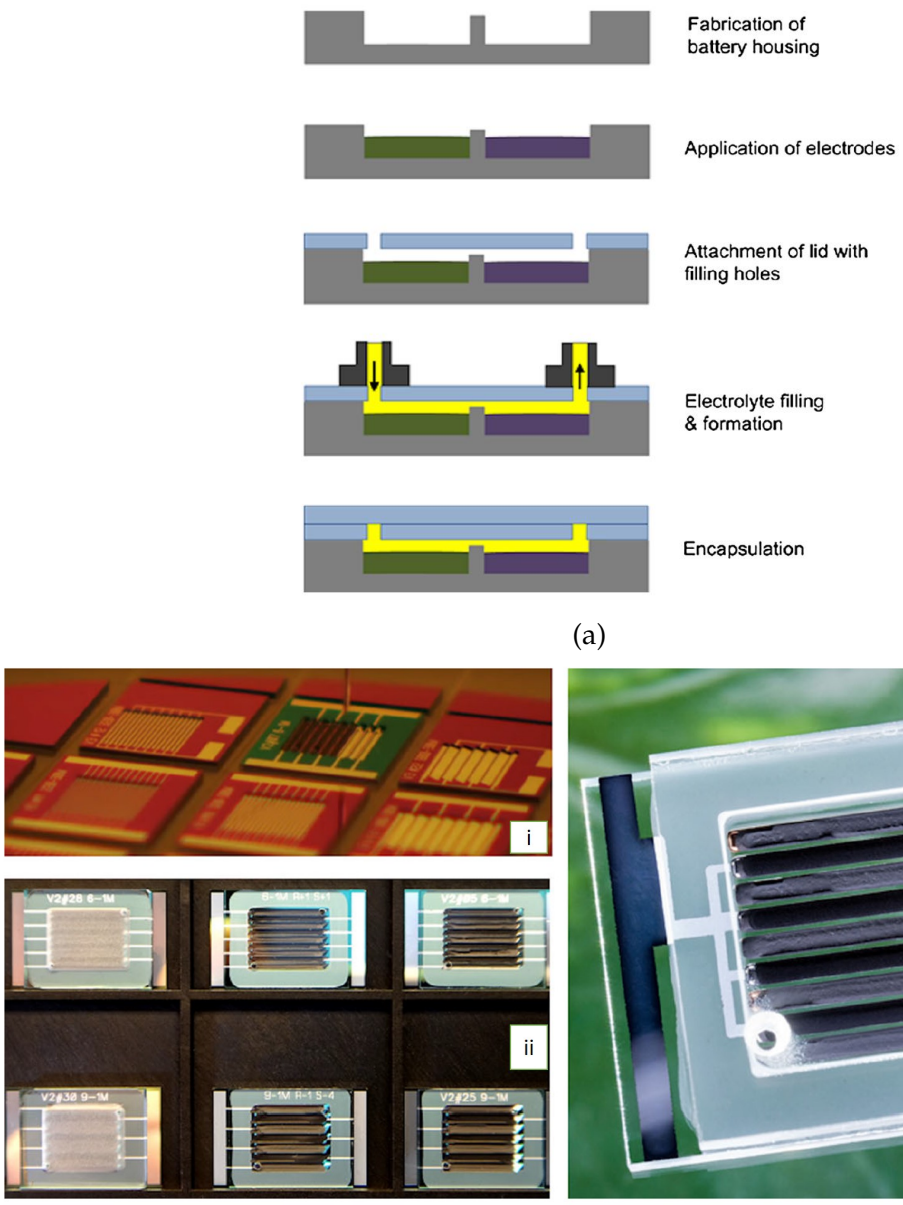

FIGURE 2.19: (a) Process sequence of microbattery fabrication by the dispense-print process; glass substrate, anode, cathode, lids and electrolyte are in grey, green, violet, blue, and yellow, respectively. (b) (i) Picture of the electrodes (in slurry form) being dispensed into the silicon cavities; (ii) and (iii) micro-battery cells with interdigitated electrodes packaged with a glass lid having electrolyte-filling holes and a final seal lid (cathode: 4 black fingers; anode: 5 grey fingers) (Adapted from Ref. [64].)

base (EM), and after doping to increase its conductivity, it's called the emeraldine salt. As Figure 2.21 shows, in the reduced structure, there are only benzenoid repeating units and all N atoms are amine functions, while in the oxidized form, benzenoid and quinoid forms coexist and all N atoms are imine functions. In addition, other, less stable states exist, and are all shown in Figure 2.21. Table 2.1 summarizes the physical properties of the different

oxidation states of PAni.

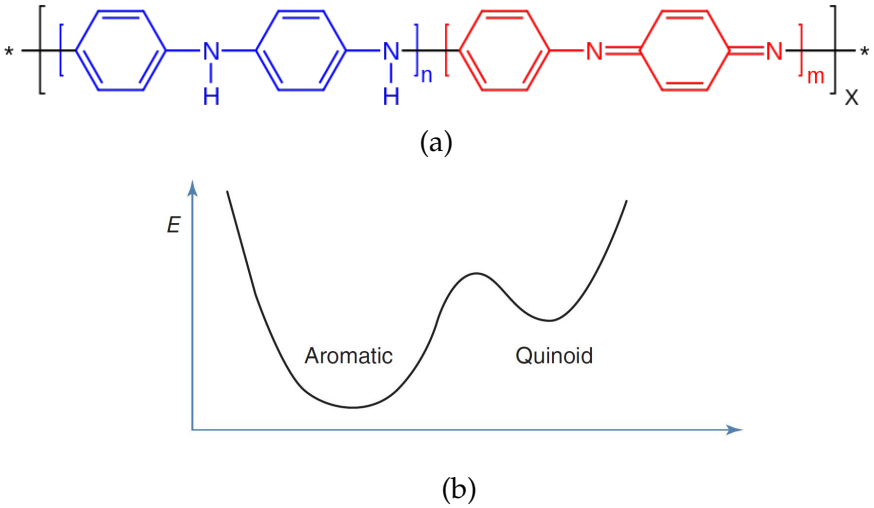

FIGURE 2.20: (a) General polyaniline structures, n+m = 1, x = half degree of polymerization (Adapted from Ref. [67]); (b) the nondegenerate ground states of polyaniline. (Adapted from Ref. [68].)

TABLE 2.1: Properties of the intrinsic oxidation states of PAni (Compiled from Refs. [69] and [70]).

Name	Value of n	Properties
Leucoemeraldine (LM)	1	Completely reduced state, white/clear, colourless, strong reducing agent.
Nigraniline	0.75	Black. Oldest synthetic pigment.
Emeraldine (EM)	0.5	Most stable and generally formed from polymerizations. Blue for the base, but green when doped to form its salt.
Protoemeraldine	0.25	Brown.
Pernigraniline	0	Blue/violet. Not stable: easily undergoes reduction easily. It's the only conjugated polymer, besides polyacetylene, that has degenerate ground states.

Only the emeraldine base becomes substantially conducting after acid doping (to form the emeraldine salt); doping has only marginal effects on the conductivity of all others. The change from one oxidation state to another can be effected by oxidizing and reducing agents, or by electrochemical methods [69].

Cyclic voltammetric studies, mass change with quartz microbalance, and *in-situ* absorption spectra have shown that the redox mechanism of PAni is the same in both aqueous and nonaqueous media [71, 72]. Figure 2.22a shows the representative cyclic voltammograms (CVs) of PAni, and 2.22b shows the corresponding redox mechanisms

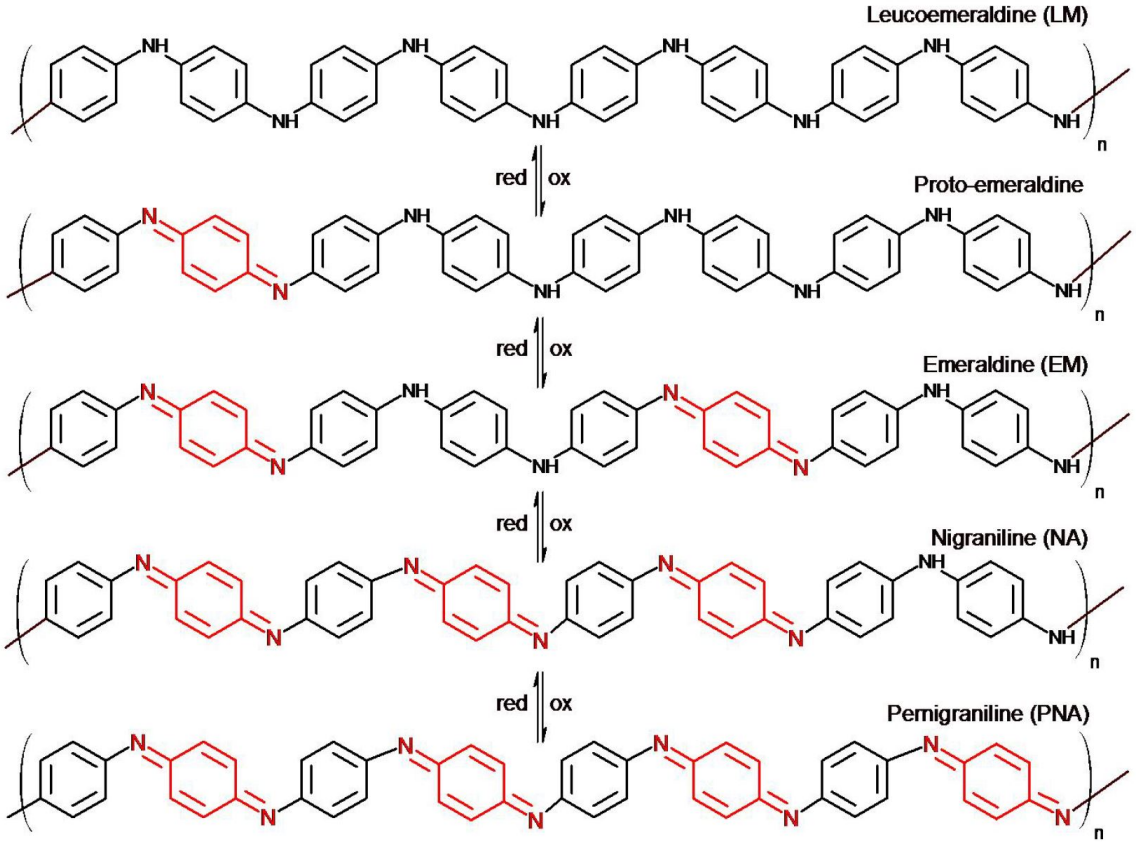

FIGURE 2.21: Octameric representation of the PAni redox states [69].

that lead to the peaks in the CVs. In general, in the first oxidation step, a radical cation at N-position is formed; in the second oxidation step, a diimine structure is formed via the cation structure, and the concomitant anion insertion leads to a doping level close to one electron per aniline unit. It's also important to note that the anion alone, not solvated anion, is inserted [72].

2.4.2 Syntheses of Polyaniline

The physical and chemical properties, morphology, degree of crystallinity, porosity, conductivity, etc., of PAni depend on the method of synthesis. Various methods exist with which to synthesize PAni, but the three most common methods are *chemical oxidative*, *electrochemical polymerization*, and *electroless deposition* methods. Some other, less used methods are enzymatic and plasma methods [69]. Here, the chemical oxidative and electrochemical polymerization method will be cursorily presented, but the electroless deposition method will be presented in more detail, as it is the method used for syntheses in this work.

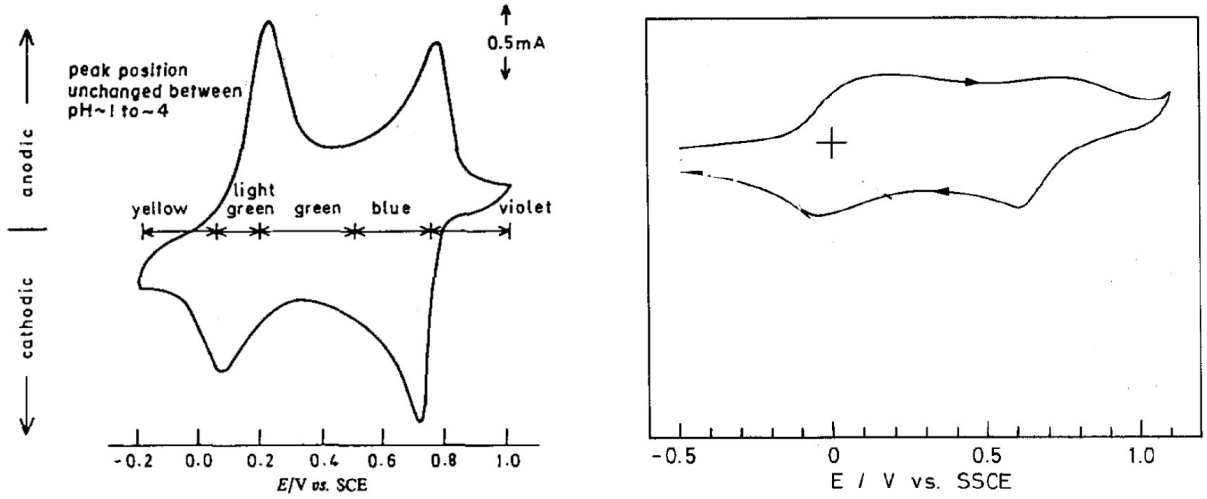

(a)

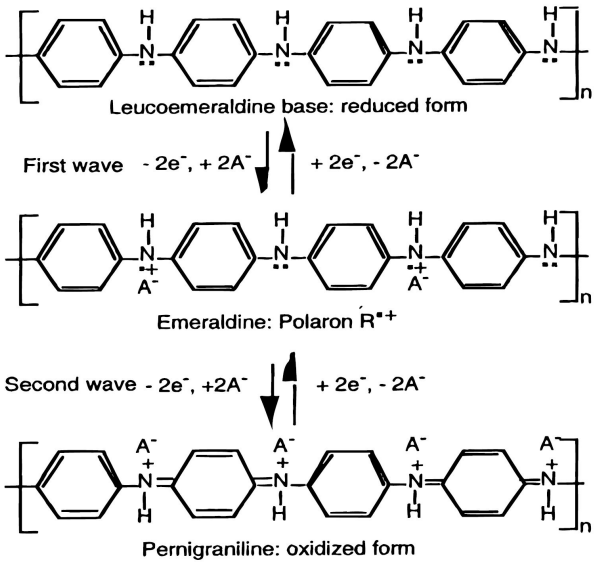

(b)

FIGURE 2.22: (a) Cyclic voltammograms of PAni in (left) 1 M aqueous HCl (Adapted from Ref. [73]) and in (right) 0.5 M $LiClO_4$ (Adapted from Ref. [72]); (b) Redox process of PAni [74].

Chemical oxidative polymerization of aniline

Chemical polymerization of aniline to form polyaniline is a bulk reaction process that forms PAni precipitates by taking advantage of the insolubility of PAni in aqueous solvents [69]; a plethora of methods exist with which PAni is produced by chemical oxidation. The variations in these methods are in the choice of solvent, acid used for doping, the oxidizing agent, reaction conditions, etc. In general, these methods lead to different properties of the resulting polymer.

Polymerization is effected at low 0 °C, since the molecular weight of the resulting polymer increases at low temperature; in addition, a solvent of high dielectric constant,

together with low temperature, is required to stabilize the cationic chain, favouring polymerization initiation and propagation. Low oxidizing agent concentration is also required to obtain a polymer of large molecular weight, since fewer side reactions occur [69]. An example of synthesis parameters is to use 0.1 M aniline in 0.1 M $(NH_4)_2S_2O_8$ and 1 M H_2SO_4, at 0 °C [75].

Electrochemical polymerization

Electrochemical polymerization occurs by the use of an electrical current to oxidize aniline molecules in an acidic solution onto an anode surface. The rate of polymerization, film morphology, conductivity of resulting polymer, etc., are dependent on the electrochemical parameters employed [69]. This method is particularly useful for controlling various properties of the resulting film.

PAni film is grown by cyclic voltammetry within a voltage range, typically between 0.2 and 1.2 V vs. Ag/AgCl.

Electroless deposition

Electroless deposition (ED) is a process in which aniline slowly polymerizes on the surface of a catalyst – typically platinum or palladium – in an aqueous acid solution of aniline. ED proceeds by an electrochemical mechanism that involves the reduction of dissolved oxygen as cathodic, and oxidation of aniline as anodic, half-reactions at the metal/solution interface [75].

The mechanism of polymerization involves, first, reaction initiation by catalytic oxygen reduction, then PAni growth by autocatalysis. This results in clean deposition only on the surface of the film, but not on the bulk of the solution. Typical reactants concentrations are 0.4 M aniline and 0.4 M H_2SO_4 aqueous solution. The reaction system is maintained at constant temperature and under oxygen saturation to ensure reproducibility of results. X-ray photoelectron spectroscopy (XPS) studies have proven that the chemical composition of PAni produced by electroless deposition is the same as the chemical oxidative and electropolymerization methods, albeit with different morphologies. Figure 2.23 shows the difference in the morphologies of PAni prepared by the three methods.

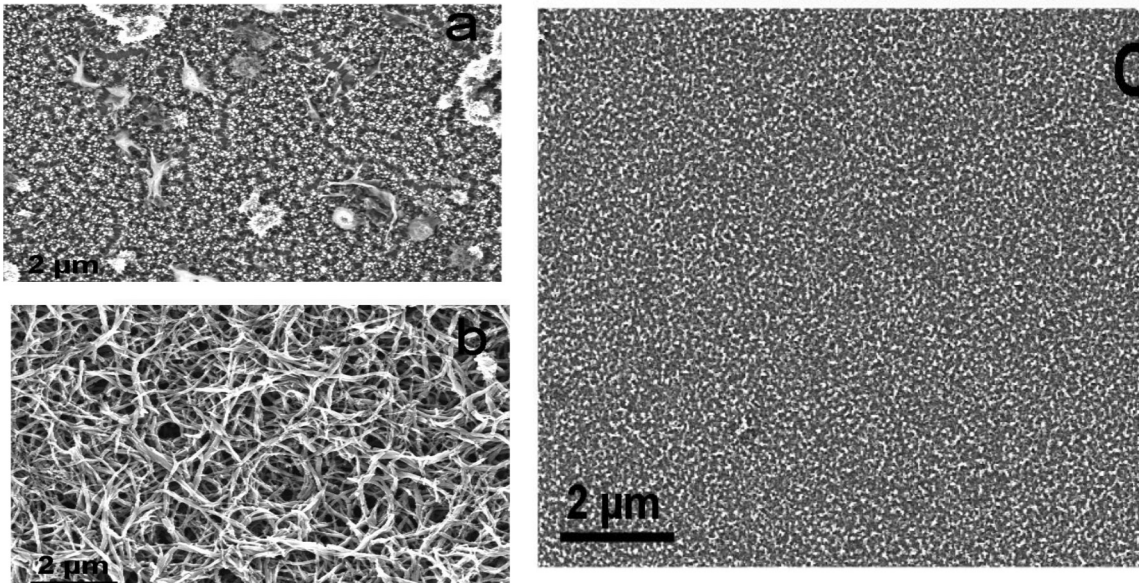

FIGURE 2.23: Scanning electron micrographs of PAni prepared by (a) Chemical oxidative polymerization; (b) electropolymerization; (c) electroless deposition (Adapted from Ref. [75]).

3 Experimental

This chapter details the experimental methods and materials employed – all the way from syntheses of electrode components and fabrication of devices to performance tests. Initially, growth of polyaniline (PAni) by electroless deposition an on a planar surface was studied in order to determine the required growth parameters, and the results therefrom were employed on the 3D nanowire network (3DNWN) after the synthesis of the nanowires; subsequently, suitable cells for different electrochemical tests were conceived and fabricated (if need be); then, electrochemical tests were carried out to determine the potential difference within which the battery will operate, and to determine the appropriate electrolyte that can operate within this potential and not degrade the components of our battery. Finally, the interdigitated architecture was effected on bare Pt 3DNWN by a laser-assisted patterning technique; these nanowires were subsequently functionalized with PAni. Alongside, various characterization techniques – like scanning electron microscopy (SEM) and atomic force microscopy (AFM) – were used to track and instruct the progress of the work[1].

3.1 Functionalization of Planar Surface with Polyaniline

The aim of this experiment was to find the optimal growth parameters to obtain a thin film of ~ 50 nm on a planar surface, so that same can be transferred to grow PAni shells on the platinum Pt nanowires (see Section 3.3). Section 2.4.2 describes the electroless deposition method of synthesis of PAni on a flat Pt substrate; here, we shall only consider the practical aspects of the technique.

Even though Pt was used for the electroless deposition (because it's more catalytically active in electroless deposition [69]), it has been reported that palladium (Pd) substrates also catalyse the reaction [75, 76]. Typically, the amount of PAni deposited on the metal surface is affected by the monomer concentration, the nature of the acid medium, and the oxygen content in the reaction medium; so, it made sense to follow prescriptions given in the literature to obtain a predefined PAni thickness and ascertain that similar results would be gotten.

[1] Perhaps it should be stated here that, because many of the experiments carried out were on systems hitherto untested, quite a tortuous path, requiring a large dose of engineering ingenuity, was followed to ensuring that accurate results were obtained.

Electroless deposition, as its name implies, proceeds without an external current or voltage but via an electrochemical mechanism in which *the same* substrate, at different times, acts as the anode and cathode of the electrochemical reactions involved. Initially, oxygen, bubbled into the acidic solution containing the monomer, is reduced on the substrate (thereby acting as a cathode in this instance), then the aniline monomer in the solution is subsequently oxidized to form polyaniline on the substrate. Figure 3.1a shows the reaction:

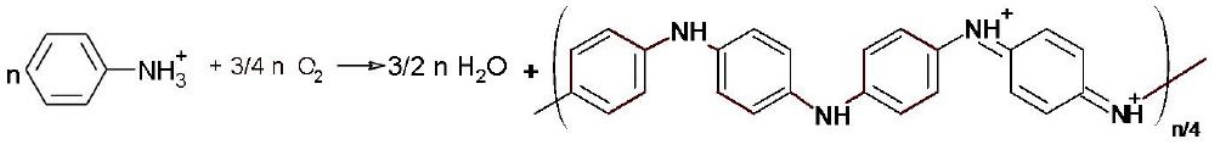

(a)

(b)

FIGURE 3.1: (a) PANi electroless polymerization reaction [69]; (b) Reactor for PAni deposition on Pt substrates. Oxygen can be seen to be bubbled through the solution, and the hoses are connected to a chiller which thermostats the reactor.

Initially, a 10-nm titanium (Ti) adhesion layer was sputtered on 4-inch-diameter silicon wafers, then 100 nm of Pt was sputtered on this adhesion layer. The sputterings were effected in the PLASSYS MP500S sputtering machine, which, for Ti, was at 15 °C, 50 sccm Ar flow rate, 100 mA applied current for 1 min 57 s to get 10 nm of Ti adhesion layer. Then Pt was sputtered under the same conditions, except this time for 9 mins to get 100 nm of Pt film[2]. The Pt-covered substrates were cut into suitable sizes for the reactor, then immersed in an aqueous solution of 0.4 M H_2SO_4 and 0.4 M aniline monomer (gotten from Sigma-Aldrich) as per the prescription of Refs. [75] and [69]. While oxygen from the atmosphere might do for the initial reduction on Pt substrate, the aniline solution was saturated with oxygen to ensure reproducibility. Also, the solution was thermostated to

[2]These deposition conditions are based on calibration studies that have been prevously done on the system.

ensure the reaction temperature was constant throughout the reaction time. Figure 3.1b shows the setup for the electroless deposition procedure.

It was found that as-prepared Pt substrate loses its catalytic activity if left unused for some time – very likely due to formation of a thin film of oxide on its surface. For this reason, each time before electroless deposition was performed, few nanometers of film was plasma-etched off its surface; this was carried out by exposing the film to argon plasma created by applying power of 100 W into argon gas at a pressure of 5 mTorr for a maximum of two minutes.

The first growth was carried out at 50 °C for 3, 5, 7, 9, and 11 hours. After it became clear that such "extreme" conditions were unnecessary to meet the thickness target of 50 nm, growth was repeated, but this time at only 25 °C for varying times of 2, 4, 5, 6, and 7 hours. Within minutes from the start of experiment, green colouration of the surface of the Pt, which deepened with time, were observed, confirming the growth of PAni. Images of the resulting films were then taken and their thickness determined by scratching its surface and measuring with an atomic force microscope (see 3.10 for details). In addition, for comparison of battery performance, thick films were also grown at 50 °C for 5 hours to give a 2 μm -thick film.

Besides surface cleaning of the substrate each time before electroless deposition, the chemicals were used as received – no further purification was done on them.

3.2 Fabrication of Pt 3D Interconnected Nanowire Network (3DNWN)

The synthesis of 3D interconnected nanowire network involved three steps, *viz.* production of porous polycarbonate template, cathodic electrochemical deposition in the template, and dissolution of the template to reveal the nanowires.

3.2.1 Production of track-etched polycarbonate template

The porous polycarbonate (PC) templates used for the electrochemical deposition of 3D interconnected nanowire network are manufactured at the Cyclotron Resource Centre here in Louvain-la-Neuve by it4ip, a spin-off of the university, by a sequential two-step process. Figure 3.2a depicts the process called *track-etching* technology [77]; it involves bombarding 20 μm polycarbonate templates with heavy, energetic ions (typically Ar^{9+} at 5.5 Mev/amu) under vacuum (10^{-2} mbar) at room temperature [78]. The template is bombarded at angles α of +25° and -25° (shown in Figure 3.2b) to the normal of the template surface.

This bombardment leads to the scission of chemical bonds in the polymer, leaving latent tracks as the ions pass through the irradiated polymer; the resulting tracks are then

etched to reveal the pores with 0.5 M NaOH aqueous solution at 70 °C for an etching time that depends on the intended pore size. Templates produced by this method are unique, because the pore size and density can be precisely controlled by varying different parameters. Besides PC, polyimide and polyester porous templates can also be made by the track-etching technology [77].

For this work, the pore size was 230 nm and the template's volumetric porosity ∼ 23 %. After the templates were received from its manufacturers, an adhesion layer of 5 nm Cr was sputtered on its surface, then 50 nm Au film was evaporated on it to serve as the cathode in the electrochemical deposition step[3].

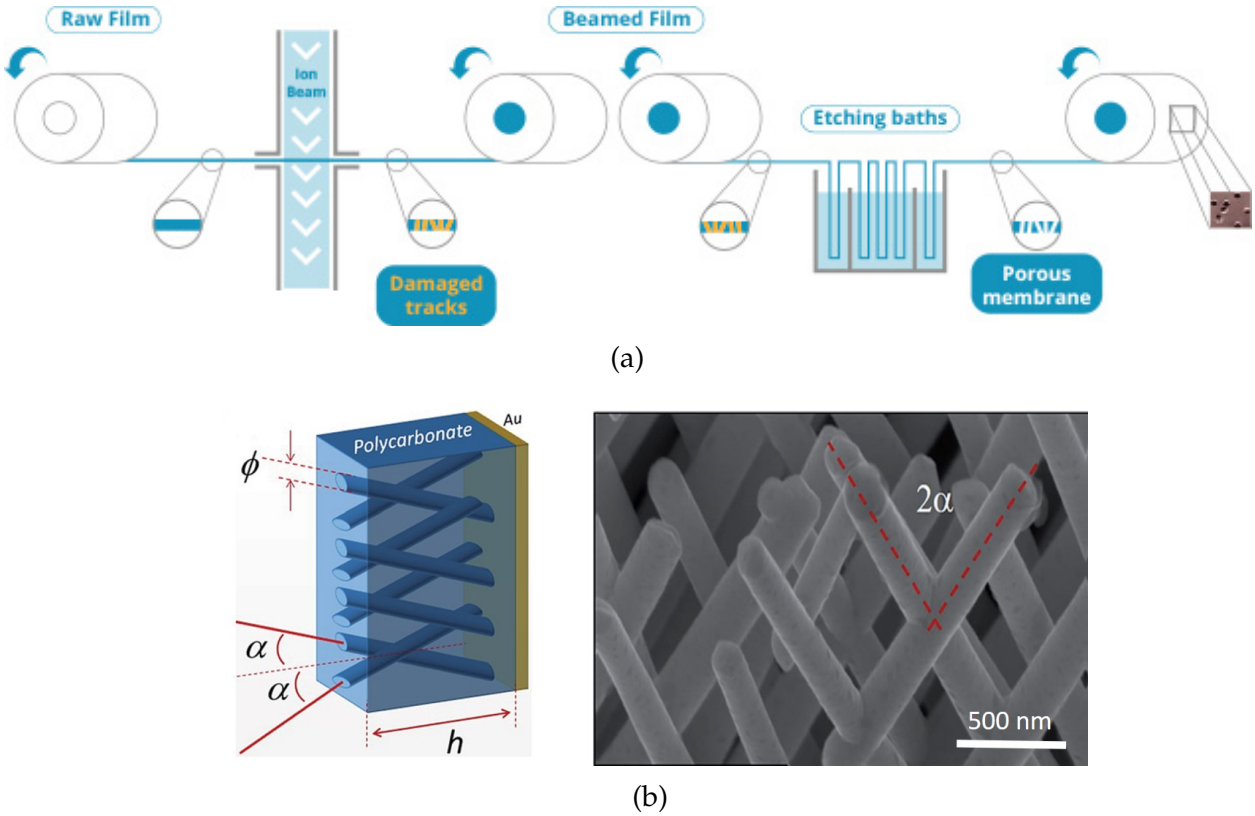

FIGURE 3.2: (a) Schematics of the track-etching technique to produce nanoporous templates [77]; (b) Schematic representation of a PC template with crossed cylindrical nanopores oriented at angles $\alpha = \pm 25°$ normal to the PC surface [78].

3.2.2 Cathodic electrochemical deposition of Pt 3D interconnected nanowire network (3DNWN)

Electrochemical deposition (or electrodeposition, ECD) is the process of depositing metals by means of electrolysis onto an electrode. In particular, *cathodic* electrochemical deposition

[3]The choice of Cr and Au film thicknesses were based on previous studies that had been undertaken to determine the optimal growth conditions for good Pt nanowire adhesion (P. van Velthem, private communication).

was used, in that the electrode on which deposition occurred was the cathode of the electrochemical setup. The *three-electrode* cell (Figure 3.3a) was used for the ECD process; in this arrangement, the current is passed between the *working* and *counter or auxiliary* electrodes. The working electrode (WE), as its name suggests, is the electrode of interest – the one wherein electrochemical processes to be monitored occurs; the counter electrode (CE) only acts to complete the electrical circuit; thus, since its electrochemical properties do not affect the behaviour of the WE, any convenient electrode can be used, but, preferably, it should be one that is inert and doesn't produce substances by electrolysis which can reach the WE and interfere with the reactions there. Potential measured at the WE is measured relative to the reference electrode (RE), whose tip is positioned very close to the WE, by a high-impedance potential difference-measuring device [35].

The cathodic ECD was effected potentiostatically, and the following reactions occur at the electrodes:

$$\text{Cathode:} \qquad \mathrm{Pt^{2+}(aq) + 2\,e^- \longrightarrow Pt\,(s)} \tag{3.1}$$

$$\text{Anode:} \qquad \mathrm{H_2O \longrightarrow \frac{1}{2}O_2 + 2\,H^+ + 2\,e^-} \tag{3.2}$$

During potentiostatic cathodic ECD, the current i varies with time t, and the total charge Q after time t is

$$Q = \int_0^t i dt. \tag{3.3}$$

The progress of electrodeposition performed potentiostatically is monitored by an $i - t$ curve[4], which exhibits four regimes as shown in Figure 3.3b. The initial stage is the *nucleation* stage, and it's exhibited as a plummet in current on the $i - t$ curve, which results from the creation of an electrochemical double layer as the nanowires nucleate. The second stage is the *growth* stage, at which the nanowires grow within the pores of the template; it's exhibited as a regime of constant current until it fills up the pores, after which the current soars, corresponding to the *cap* stage where the nanowires first outgrow the pores. If electrodeposition continues, the overgrown nanowires form a film over the template and the current continues to rise until it asymptotes, corresponding to the *overfilling* stage [79].

Electrodeposition is an electrolytic process and the amount of material deposited through an electrolytic process is given by Faraday's first law of electrolysis: the amount of substance produced at each electrode is directly proportional to the quantity of charge flowing through the cell. It's given mathematically as

$$Q = nFN \tag{3.4}$$

[4]Called a *chronoamperometrogram* – but this is certainly a mouthful.

where n is the change in the charge of the metal, F is Faraday's constant and N is the number of moles of metal deposited. By calculating the area under the $i-t$ curve, Q is determined and by relating to Equation 3.4, the number of moles, hence mass, of metal deposited can be easily determined.

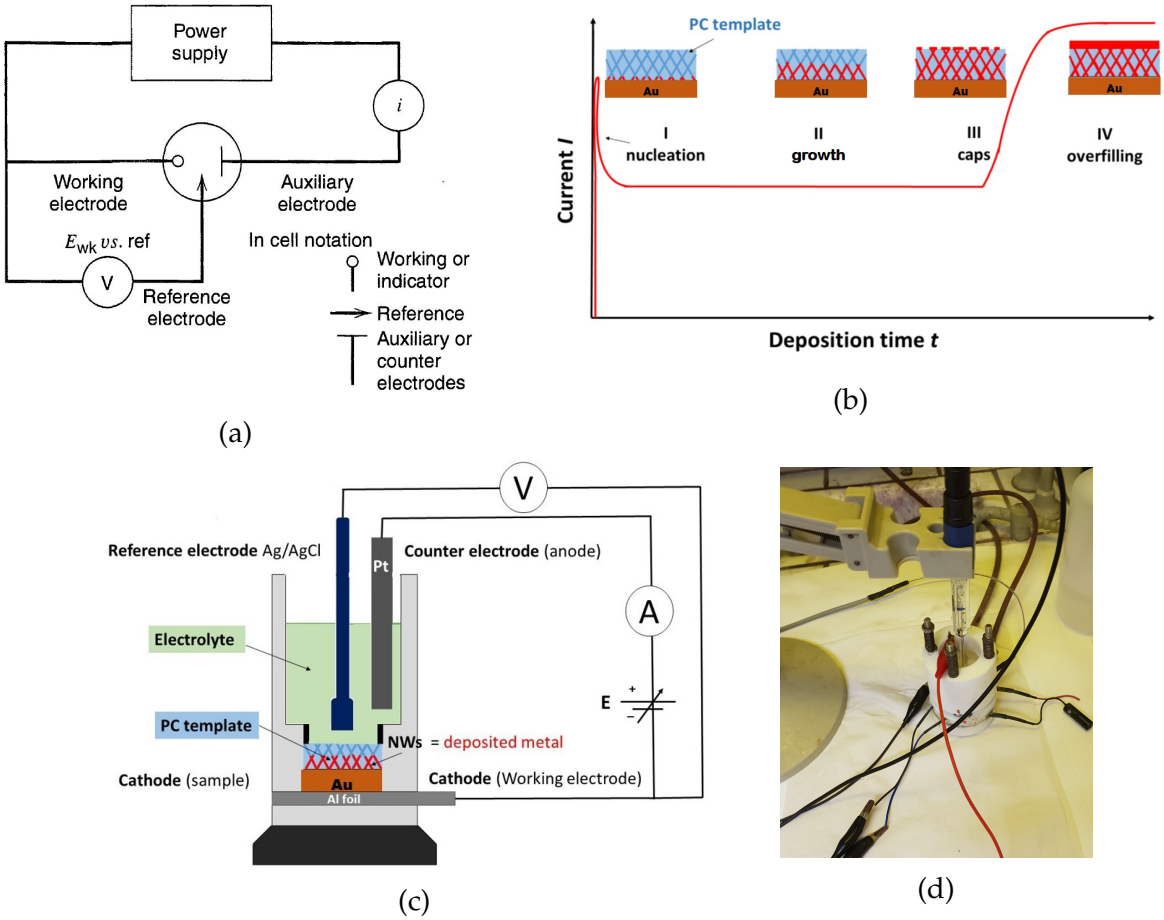

FIGURE 3.3: (a) Three-electrode cell and notation for the different electrodes [35]; (b) Typical $i-t$ curve for electrochemical deposition (Adapted from Ref. [80]); (c) Schematic representation of the electrodeposition setup (Adapted from Ref. [80]); (d) Photograph of an operating electrodeposition cell, showing the Ag/Ag^{+} reference electrode, external connections to potentiostat, and thermocouple.

Figures 3.3c and 3.3d show the schematic of the ECD cell setup and of an assembled operating cell, respectively. The body of the cell is made of Teflon™. Two types of substrates were used for ECD – Si and quartz. Four-inch diameter Si wafers, stored in extremely inert conditions, were gotten from the clean room; then an adhesion layer of 5 nm Cr and 100 nm Au thin film were deposited onto the surface of the as-received Si wafers. A 7-mm diameter template (prepared in Section 3.2.1) was used on every 1 cm $\times$ 1 cm Si substrate. The circular template was gently placed on the substrate with its Au-coated face in contact with the Au face of the Si substrate. The cell was then assembled as shown in Figure 3.3d. Al foil was used as the current collector of the WE

(the substrate) to the potentiostat; the RE was Ag/AgCl (0.197 V vs. standard hydrogen electrode SHE), and the CE was the Pt strip shown. All ECD were carried out in continuous mode on Potentiostat/Galvanostat Model 263A from Princeton Applied Research at a deposition potential of - 0.3 V (as per studies by Ref. [81]). The electrolyte was a 10 g Pt/l Platinum-DNS-Bath from Metakem.

Furthermore, based on previously undertaken studies (P. van Velthem, private communication), it has been shown that the adhesion of Pt nanowires depends on both electrodeposition temperature and the thickness of Au film on the template. We have seen in Section 3.2.1 that 50 nm Au film on the template was the best for adhesion. Concerning deposition temperature – we know that ECD rate increases with temperature, but this leads to the formation of nanotubes rather than nanowires, which results in poor nanowire adhesion; thus, to solve this problem, while retaining a reasonable ECD rate, ECD was carried out at two temperature regimes: first at 25 °C for $\sim$ 1500 s, which, although a slow ECD rate, ensures that nanowires (rather than nanotubes) are formed at the outset of the ECD process. After this period, the temperature of the system was increased to 50 °C, which leads to a rise in current, hence ECD rate, until completion.

Recall that the charge Q gives the amount of deposited material; this makes it easy to limit the height of the nanowires by setting the total charge to be obtained in an ECD session. Again, P. van Velthem (private communication) has shown that 1 C of total charge corresponds to approximately 1 μm of nanowire height for deposition in a 7 mm-diameter PC template, and this fact has been confirmed several times by the author during the course of the work; therefore, by setting (on the Potentiostat's software) the total charge to 10 C, 10 μm of nanowire height was always attained. This was the height of nanowires used on all electrodes[5].

After ECD, the cell was disassembled, and the sample removed and placed in a flat beaker containing dichloromethane CH_2Cl_2 (from VWR Chemicals) in order to dissolve the template. Afterwards, the sample was rinsed by gently placing it in another flat beaker containing distilled water, then removed and left to dry. One had to be careful at this stage, because manhandling the sample could lead to nanowire detachment from the substrate. For instance, during cell disassembling, the O-ring typically remains stuck to the substrate, as can be seen in Figure 3.4a; to avoid detachment of the nanowires, everything in Figure 3.4a was placed in dichloromethane and the O-ring detaches on its own while the template dissolves, leaving the nanowire network behind. Figures 3.4a and 3.4b show the deposited nanowires before and after dissolution of the template, respectively.

ECD was initially done on Si substrate for deposition studies, because it's easier to handle and more readily available; however, quartz was the required substrate for the

[5]A word on this is in order. The nanowires are not standing normal to the substrate but inclined at some angle; thus, the height referred to here is the height of the template that has been filled, not that of an individual nanowire.

laser patterning (see Section 3.6) to form the interdigitated structure, since laser patterning is possible only on an insulating substrate. Exactly the same procedures – from metals deposition to template dissolution – were used on quartz substrates. It was observed multiple times that ECD didn't occur on quartz substrates (with deposited Au as cathode) unless it was initially etched (by the same Pt-etching procedure) for a minute before cell assembly.

(a) (b)

FIGURE 3.4: Substrates with 3D-NWN (a) before and (b) after template dissolution.

3.3 Functionalization of Pt 3D Interconnected Nanowire Network (3DNWN)

After successful nanowire growth, electroless deposition of PAni was done on the nanowires following the procedure of Section 3.1. Note that plasma etching was also done on samples that had been prepared long before electroless deposition.

3.4 Cyclic Voltammetry of Polyaniline Thin film in Aqueous and Nonaqueous Electrolytes

Section 2.2.3 presents the essentials of cyclic voltammetry (CV); CV was done for two reasons: the first was to identify the potential range within which cells made from PAni electrodes can be cycled; the second was to study the electrode redox kinetics of PAni during cycling to give an idea of its behaviour.

CV of PAni was initially done in 1 M H_2SO_4 at a scan rate ν of 5 mV/s in an open cell at room temperature, using a three-electrode cell, with PAni film as the WE, Pt wire

as the CE, and saturated calomel electrode[6] (SCE, 0.242 vs. SHE) as RE. The second CV was done in 1 M $LiClO_4$ in acetonitrile in a Swagelok cell (shown in Figure 3.5a. Since PAni is conductive, it was directly connected to the potentiostat by contact with a current collector (like was done in Section 3.2.2); it was done by covering a very small area (just enough for electrical contact) of its surface with a stainless steel strip placed over the back of the substrate[7]. The Swagelok cell components, the metal strips (current collectors), the substrates to be tested, etc., were left in the Haraeus Vacutherm vacuum oven for 18 hours to remove all moisture, then assembled in the glovebox. After assembling, the cell was removed and CV was done outside with a BioLogic SP-300 potentiostat. Note that in both cases, PAni substrate used was one of the ones prepared at 25 °C for 5 hours.

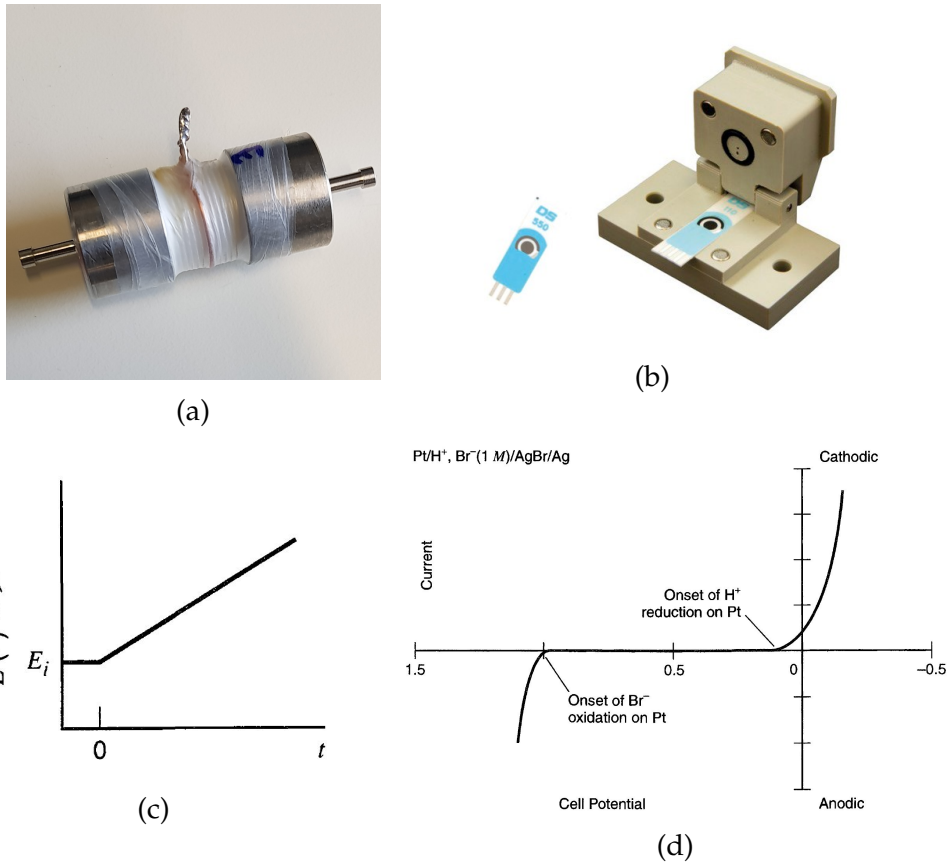

FIGURE 3.5: (a) Assembled Swagelok cell for CV in nonaqueous electrolyte; (b) Screen-printed electrode used for stability window measurement; (c) Linear potential sweep or ramp; (d) Schematic current-potential curve for the cell $Pt/H^+,Br^-(1\ M)/AgBr/Ag$ [35].

[6]The saturated calomel electrode is the half-cell $Hg/Hg_2Cl_2/KCl$ (saturated in water).

[7]Stainless steel was used as the current collector, instead of strips of Al or Cu foil, because it was found that the two latter metals are stripped in the cycling potential range.

3.5 Determining the Stability Window of Non-aqueous Electrolyte

The stability or electrochemical window is the potential range in which an electrolyte/-solvent system does not undergo any oxidation or reduction reactions. *Linear sweep voltammetry* (LSV) is used to determine the electrolyte stability window; it involves applying a potential linearly with time, i.e., applying a voltage ramp, with a sweep rate ν ranging from 10 mV/s to 1000 V/s in conventional electrodes, and the potentials at which specific current densities are reached are identified as the electrochemical limits [35]. Figure 3.5c shows the input in LSV; we can see that it is akin to CV, but with no sweep reversal. The key is to sweep the potential of an inert working electrode, typically Pt, in the electrolyte of an interest to potentials as negative and positive as possible until a continuous increasing current is gotten; the range between the potentials that cause continuous increase in current is the *stability window*.

Typically, the potential at which a specific current density $J_{cut-off}$ is reached is used to define the cathodic and anodic limit of the electrolyte. The choice of $J_{cut-off}$ is somewhat arbitrary with values in the range of 0.01 to 5.0 mA/cm^2 [82].

The stability window of a nonaqueous electrolyte, 1 M $LiClO_4$ in acetonitrile solvent, was determined by the *screen-printed electrode* gotten from Metrohm (shown in Figure 3.5b), a three-electrode cell, with Pt working and counter electrodes, and Ag as the *pseudo*-reference electrode. The anodic potential was scanned from 0 to +3 V, and the cathodic potential was scanned from 0 to -2 V, both at a scan rate ν of 10 mV/s with a BioLogic SP-300 potentiostat. The electrolyte used was prepared, and the LSV itself was carried out, in the glove box from Innovative Technology, with an Ar atmosphere and O_2 and H_2O concentration of no more than 0.1 ppm. The screen-printed cell was left in the Haraeus Vacutherm vacuum oven for 18 hours at 70 °C to remove any moisture before use in the glovebox.

3.6 Laser-assisted Patterning of Pt 3DNWN to Side-by-side Interdigitated Electrodes

After fabrication of nanowires on quartz substrates, the initial spherical samples were patterned with a laser-assisted method to form side-by-side interdigitated electrodes with the 3DNWN.

In order to form the interdigitated electrodes, *Picosecond laser* technology (PL) was used for ablation of unwanted zones on the initial 3DNWN. PL is a micro-machining technique that involves *photoablation* – ablation that results from laser photons directly

breaking the chemical bonds in an exposed region of a material, thereby sublimating materials fron the said region – to make high-precision patterns on a material. Compared to other micro-machining techniques, it's a relatively cold process, therefore leading to a very small area of heat-affected zone (HAZ); it's very clean, leaves no recast material after ablation, and requires no need for post-processing [83]. It uses ultra-short pulses – in the picosecond domain or shorter (see Figure 3.6a) – which allows for instantaneous peak powers, and, because they have high fluence, they can drive multi-photon absorption that excites electrons in the material, directly breaking chemical bonds. Because its pulsewidth is shorter than the thermal diffusion rate in materials, heat from residual thermal effects is removed with the atomized material before the formation of a HAZ, resulting in a very small HAZ.

For this work, the *Oxford picosecond laser* was used; a small, constant pulse rate of 1 pulse per 5 μs (i.e., frequency of 200 kHz), was used to give an ultra-precise control of surface ablation. The laser beam wavelength was 355 nm; the operating power P was 3 W; the spot diameter was 10 μm; and the engraving speed was 200 mm/s. Figures 3.6b and 3.6c show the intended planar pattern and 3D architecture, respectively. As Figure 3.6b shows, the spacing between the digits are 100 μm [8], the width of each digit is 200 μm, and the length of each digit is 6 mm.

3.7 Cell Assembling

The thin- and thick-film electrodes were each assembled into coin cells, while the substrate containing the interdigitated electrodes was assembled in a custom-made cell. Before cell components assembling, all cell components were dried at 70 °C for 18 hours in the vacuum oven (just as in the previous cases). Assembling of coin cells containing thick and thin film electrodes was done in the glovebox, then brought out to be tested, while the assembling of the 3D battery (without electrolyte) was done outside before being placed in the vacuum oven. Only after assembly, drying and placing in the glovebox was the electrolyte added.

Figure 3.7a shows an exaggerated schematic of the assembled symmetric 13-mm coin cells. It contained two ~ 1 cm $\times$ 1 cm thick- and thin-film electrodes, respectively. Two pieces of 13-mm diameter Whatmann 1823-150 glass microfiber filters (the separator), soaked in 12 drops of 1 M $LiClO_4$-acetonitrile electrolyte, were used in both cases. Stainless steel was used as the current collector and it covered the PAni surfaces only slightly. The positive and negative cans (LIR2032) were made of stainless steel, and the assembly didn't contain a spring, because the thickness of the components were enough to make it tightly

[8] The inter-digit spacing has been exaggerated to enable clear dimensioning.

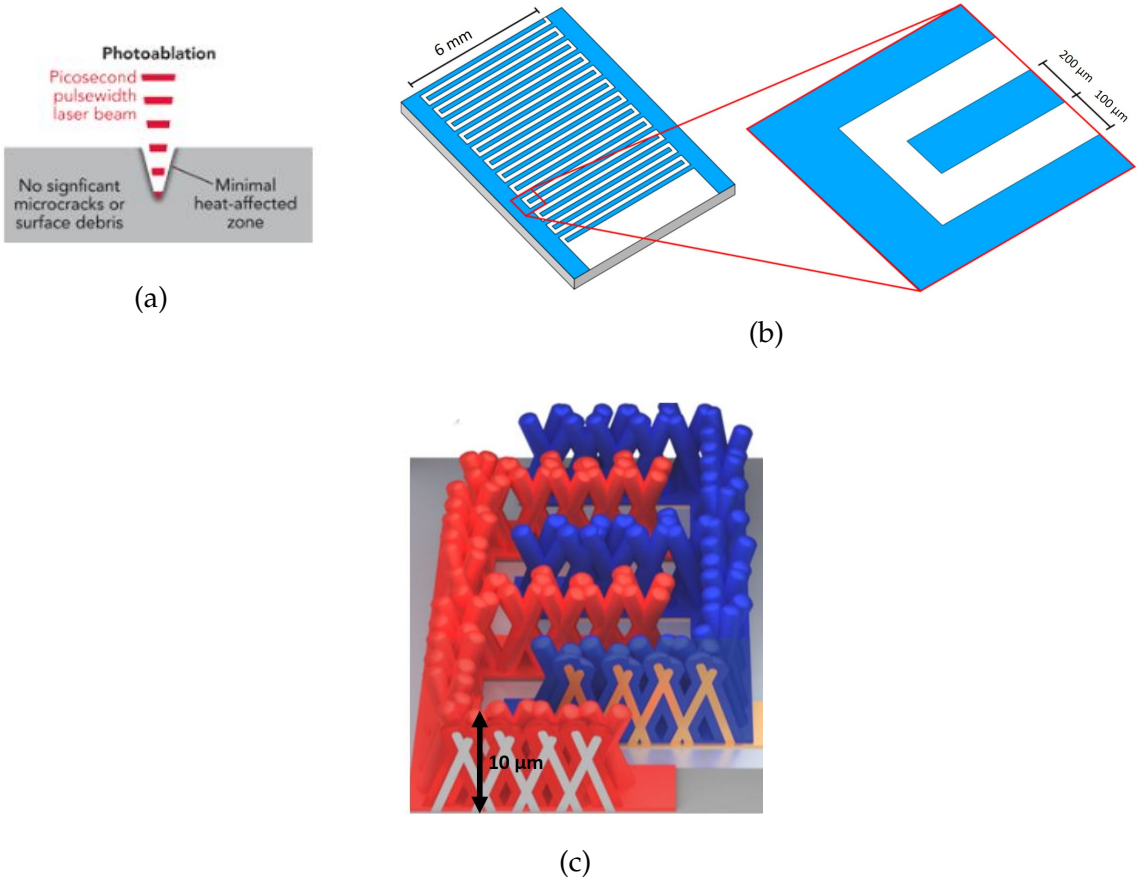

FIGURE 3.6: (a) Description of photoablation; (b) Intended planar pattern of the interdigitated architecture with relevant dimensions (Adapted from Ref. [84]); (c) Intended architecture of the interdigitated 3DNWN electrodes.

assembled. After assembly, tightening was done by pressing together with a pressure of 500 psi.

Figure 3.7b shows the custom-made cell for cycling the interdigitated cell. Each digit (electrode) was connected to an external energy source by attaching a copper wire with silver paint. In the glovebox, 12 drops of the electrolyte was put in the cell, covered with a rubber stopper, placed in Faraday cage, then connected to the potentiostat.

3.8 Galvanostatic Charge–discharge Cycle Testing

Section 2.2.3 presents the technical details of cycle tests, in general. The cycle test is the most important test to characterize the performance of batteries. To evaluate the performance of fabricated batteries, cycle test at constant currents, i.e., galvanostatically, were performed. The cycle tests on the thin-film battery were performed on the Neware battery testing system model BTS4000 Series, while the cycle tests on the thick film battery and 3D microbatteries were performed on the Arbin battery testing system model BT2043.

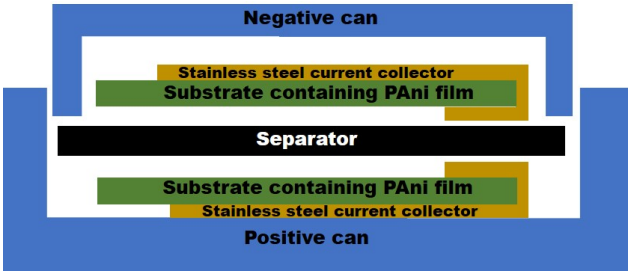

(a)

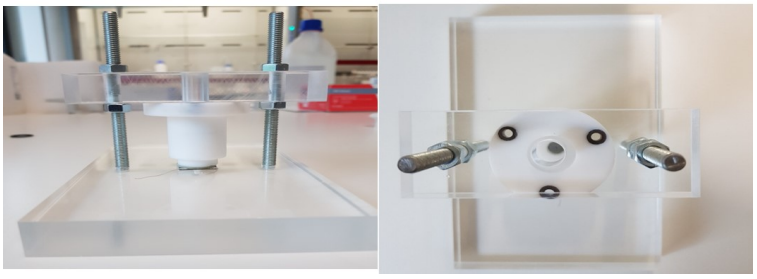

(b)

FIGURE 3.7: (a) Schematic of the assembled coin cell for the thin- and thick-film electrodes; (b) Front and plan view of the custom-made cell used for 3D battery cycle testing. On the left photograph, copper wire can be seen extending from the battery.

3.9 Scanning Electron Microscopy

Scanning electron microscopy (SEM) is a type of electron microscopy that produces images of a sample by scanning it with a focused beam of electrons. The electrons interact with atoms in the sample, producing various signals that contain information about the sample's surface topography and composition. The electron beam is generally scanned in a raster scan pattern, and the beam's position is combined with the detected signal to produce an image. It's the most common technique for the characterization of surfaces and of the morphology of nanostructures.

Figure 3.8a shows the schematic of an SEM; typically, the electrons leaving the electron gun are generated by thermionic emission from a tungsten filament, ceramics like CeB_6 or LaB_6, or field emission guns (FEG) for higher resolution. The electrons are accelerated towards the sample by potential in the range of 2 to 50 kV in a vacuum; the condenser lens then demagnifies the electron beam up to 2–10 nm, as it hits the surface of the sample. The detector counts the number of resulting particles, like secondary or backscattered electrons, and this information is transferred to a monitor, which displays the data. As Figure 3.8b shows, a number of interactions are possible, depending on the depth of sample probed, from which different information of the sample can be derived. The secondary electrons give information about the morphology or topography of samples; backscattered electrons give contrast in phase composition; the others give

different chemical information, depending on the depth, nature of the material and the sensitivity hoped for [85, 86].

For analyses carried out during the course of this work, the SEM used was JSM-7600F from JEOL, whose primary electron source is a Schottky Field Emission Gun (FEG), and has Semi-Inlens secondary electron detector and Backscattered electron detector. The acceleration potential was always 15.0 kV.

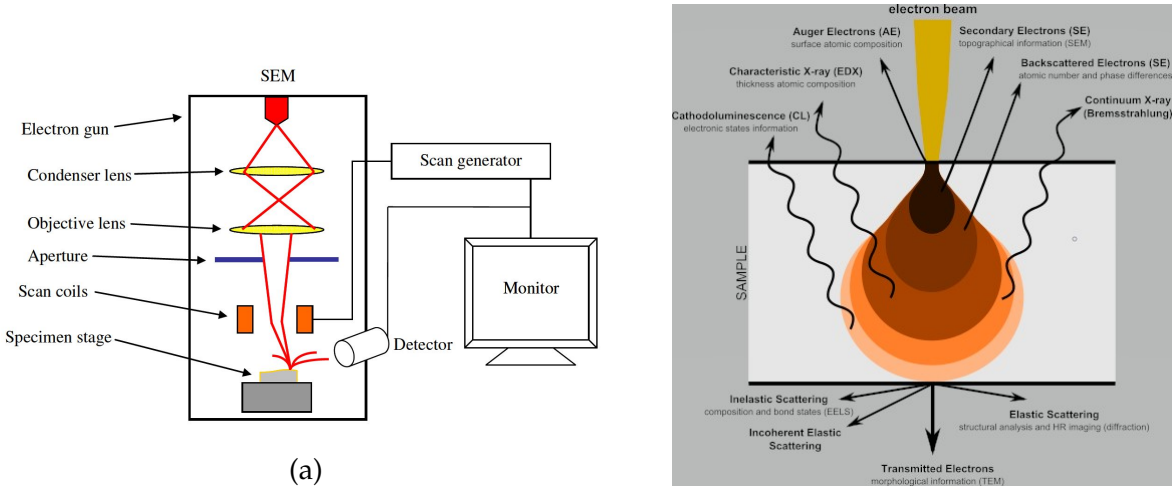

(a) (b)

FIGURE 3.8: (a) Schematic of the scanning electron microscope; (b) types of electron-matter interactions [85].

3.10 Atomic Force Microscopy

Atomic Force Microscopy (AFM) is an imaging technique used to measure surface topography, surface hardness, and elastic modulus, and used for depth profiling at the atomic level. It operates by measuring the forces between the sample (to be tested) and the tip of a probe, and this force depends on the probe geometry, spring constant of the probe, and the distance between the probe and sample. Its mode of operation is having a sharp probe tip, with atomic dimensions, scanning over a sample surface along with a feedback mechanism that enables piezoelectric scanners to maintain the tip at a constant force (to obtain information about topography), or at constant height (to obtaining the force information above the sample surface). The probe tip is brought close enough to the surface in order to detect the repulsive force between atoms in the tip and sample. Probe tips are typically made of Si_3N_4 or just Si [87, 88]. Figure 3.9 is a schematic of the basic operating principle of an AFM; the surface topography of a sample is tracked by monitoring the deflection of the cantilever, δz, which is measured as a function of tip position, often by using the back of the cantilever as a reflector for a laser beam. As the tip scans across the surface of the

sample, the cantilever is deflected along with the contour of the sample's surface; the laser beam is then deflected off into a dual-element photodiode. With this setup, picometer-scale displacements can easily be measured. The detection system collects the difference in light intensities between the upper and lower photodetectors and converts it into a voltage.

In this work, AFM was mainly used to determine the height of PAni electrolessly deposited at various growth conditions by scratching of the surface of the film with a razor blade. Icon Dimension Multimode Scanning Probe Microscope from Bruker was used for all AFM analyses.

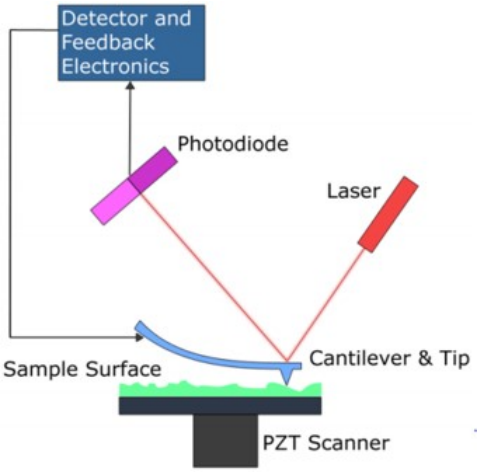

FIGURE 3.9: Schematic diagram of the working principle of atomic force microscopes Instruments [88].

4 Results and Discussion

In this section, the results of the experiments carried out (as described in Section 3) will be presented. At this point, we might find a recap of the goal of this work aidful. The purpose of this work is to fabricate and test a microbattery, whose electrodes are *symmetrical*, i.e., made of the same material, with an interdigitated architecture. To this end, we used electrodes made from 3D interconnected nanowire networks (3DNWN), and selected the active material to be polyaniline (PAni), a conducting polymer that has three main redox states – *leucoemeraldine*, *emeraldine*, and *pernigraniline* – depending on the fraction of benzenoid and quinoid states in the overall structure. The method of synthesis employed in this work – electroless deposition – produces PAni in the conducting, emeraldine-salt state, which is, in fact, the mid-redox state; thus, by applying a reducing or oxidizing current to emeraldine-salt electrodes (charging), the electrodes are reduced or oxidized to the leucoemeraldine or pernigraniline state, respectively, resulting in a substantial potential difference that can drive charges during discharge of the battery. Ideally, during discharge, both electrodes return to the emeraldine state, since reactions opposite to those that occur during charging should occur during discharging. As we shall soon see, the results indicate that this is indeed what occurs.

In so far as the literature review has shown, this work is the first attempt at undertaking such a task; in addition, because of the challenges with assembling full cells (microbatteries complete with both electrodes) with electrodes made of 3D nanostructures [89], most of the results in the literature are for half-cells, especially for alkali-metal (LI^+, Na^+) batteries, which are simply cycled against the pure form of the metals. Although the architectures and materials from many of these works are different form ours, they can still be used in comparison, because, if anything, they give an idea of the performance of microbatteries taken *in toto* (i.e., materials and architecture considered together). Nevertheless, results from Refs. [78] and [80] are relevant, because, although based on Li^+-ion half-cells, the working electrodes (half-cells) are made of the same 3DNWN like ours, albeit with different active materials, and synthesized by the same process.

4.1 Sample Fabrication

In this section, the results of the experiments leading to device fabrication are presented, with a discussion of observations.

4.1.1 Functionalization of planar surface with polyaniline

Our purpose here was to find the optimal growth parameters to electrolessly deposit PAni on the nanowires; since planar surfaces are easier to produce and handle, it seemed as the rational starting point. As was stated in Section 3.1, the first growth was carried out at 50 °C for 3, 5, 7, and 11 hours, then again at 25 °C for 2, 4, 5, 6, and 7 hours.

Figure 4.1a shows optical micrographs of the initially deposited PAni films taken with the AFM-integrated optical microscope. The scratch that was made to measure film thickness is obvious and, in all cases, the AFM cantilever and LASER beam can be seen. The LASER beam is seen because the all the pictures were taken prior to laser alignment. Furthermore, it can be seen that electroless deposition isn't uniform on the surface; since electroless deposition is a catalytic reaction, involving a number of surface reactions, it is likely that this effect arises from Pt surface poisoning due to adsorption of a range of chemical compounds. To confirm this, rather than chemically reactivating the catalyst surface, it was decided that slight surface etching, to remove the poisoned parts, might suffice to reactivate the surface, in line with recommendations from Ref. [70].

The results not being up to par led to growing new films after Pt etching, this time at lower temperature of 25 °C temperature for slower deposition rate [69] that would ensure more homogeneous growth. Figure 4.1b shows the optical micrographs of PAni film grown at 25 °C for different times; the green colour is proof that that resulting film is, indeed, PAni in the emeraldine salt state, and, as can be seen, is darker with increasing time, signifying that the thickness increases with time.

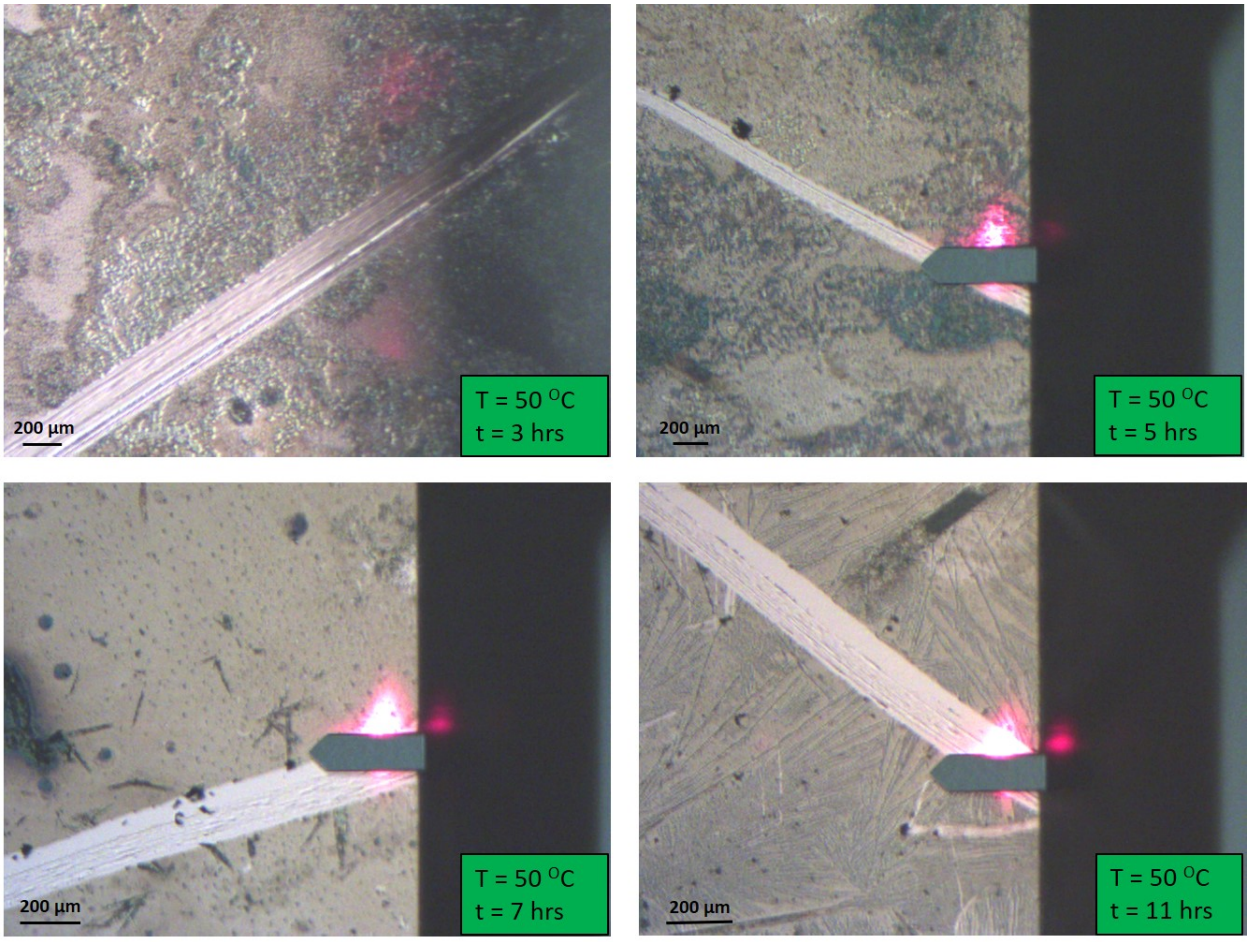

(a)

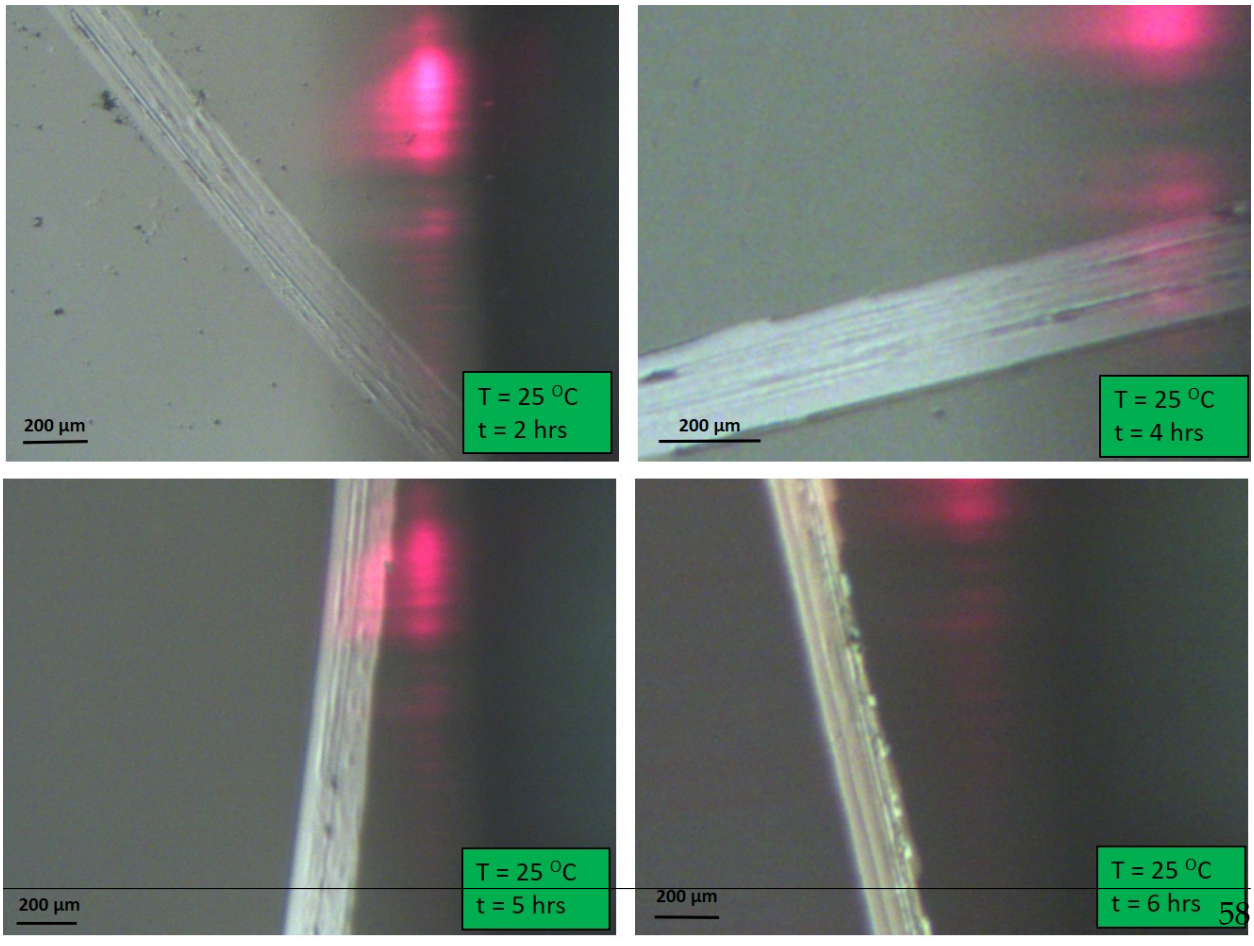

(b)

FIGURE 4.1: Optical micrographs of (a) Poorly electrolessly deposited, (b) Perfectly

Subsequently, film thickness was measured with the AFM by scanning in the neighbourhood of one side of the scratch made. Figure 4.2 serves as example to show the nature of analyses done on the AFM data: it's the 2D image profile of the PAni film, deposited at 25 °C for 2 hours, in the neighbourhood of the scratch. Data around the scratch and the PAni film are collected (the boxed region) and after the required image processing with the NanoScope Analysis (version 1.7) software, a clear height profile is gotten, as shown on the right of Figure 4.2. This sort of data was collected on several points and an average was taken to give the film thickness. Although several factors affect the accuracy of such AFM measurements, we can take the accuracy of these measurements to be $\pm$ 10 %. In the following sections, we shall see confirmations of this.

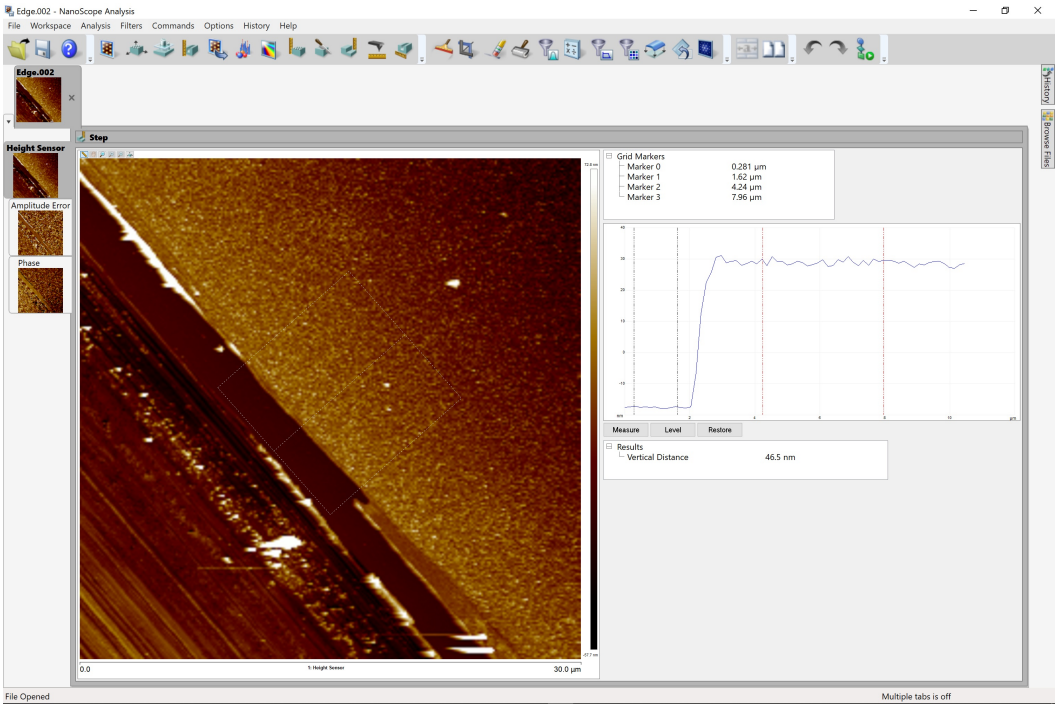

.

FIGURE 4.2: 2D AFM image profile of electrolessly deposited PAni in the neighbourhood of the scratch for height measurement

Table 4.2 presents the thickness of PAni electrolessly deposited on 100 nm of Pt on a Si substrate. These results are in agreement with published values [70, 75].

TABLE 4.1: Thicknesses of PAni films electrolessly deposited on Pt substrate at 25 °C

Deposition time (hours)	Thickness (nm)
2	42
4	50
5	94

4.1.2 Fabrication of Pt 3D interconnected nanowire network (3DNWN)

The porous polycarbonate (PC) templates used were received from it4ip, deposition of cathode thin films were done in the laboratory. Since the charge was set to 10 C, the height of the resulting nanowires was 10 μm, and we know beforehand the mass of electrodeposited Pt nanowires. From Equation 3.4, we can easily determine the mass of the electrodeposited Pt to be 10.1 mg. Furthermore, Figure 4.3a shows the $i - t$ curve for the electrochemical deposition (ECD) of PAni; clearly, the area under the curve is the total charge imposed (10 C), and it shows two temperature regimes, one at 25 °C for 1300 s and the other at 50 °C until the end of the process. As has already been noted, this was done to ensure good adhesion of the nanowires onto the substrate. Since the ECD was not done up to half the template thickness, only the first two stages of ECD – *nucleation* and *growth* – can be seen in Figure 4.3a.

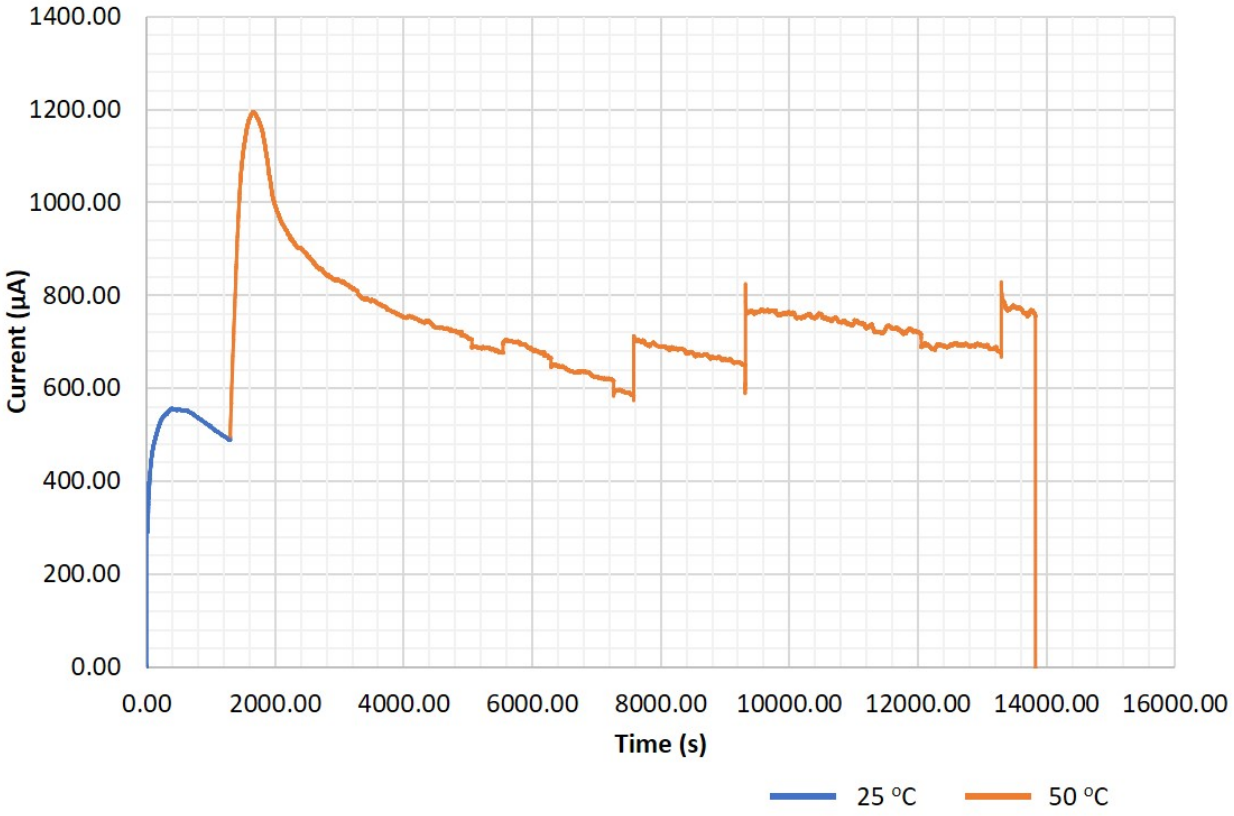

(a)

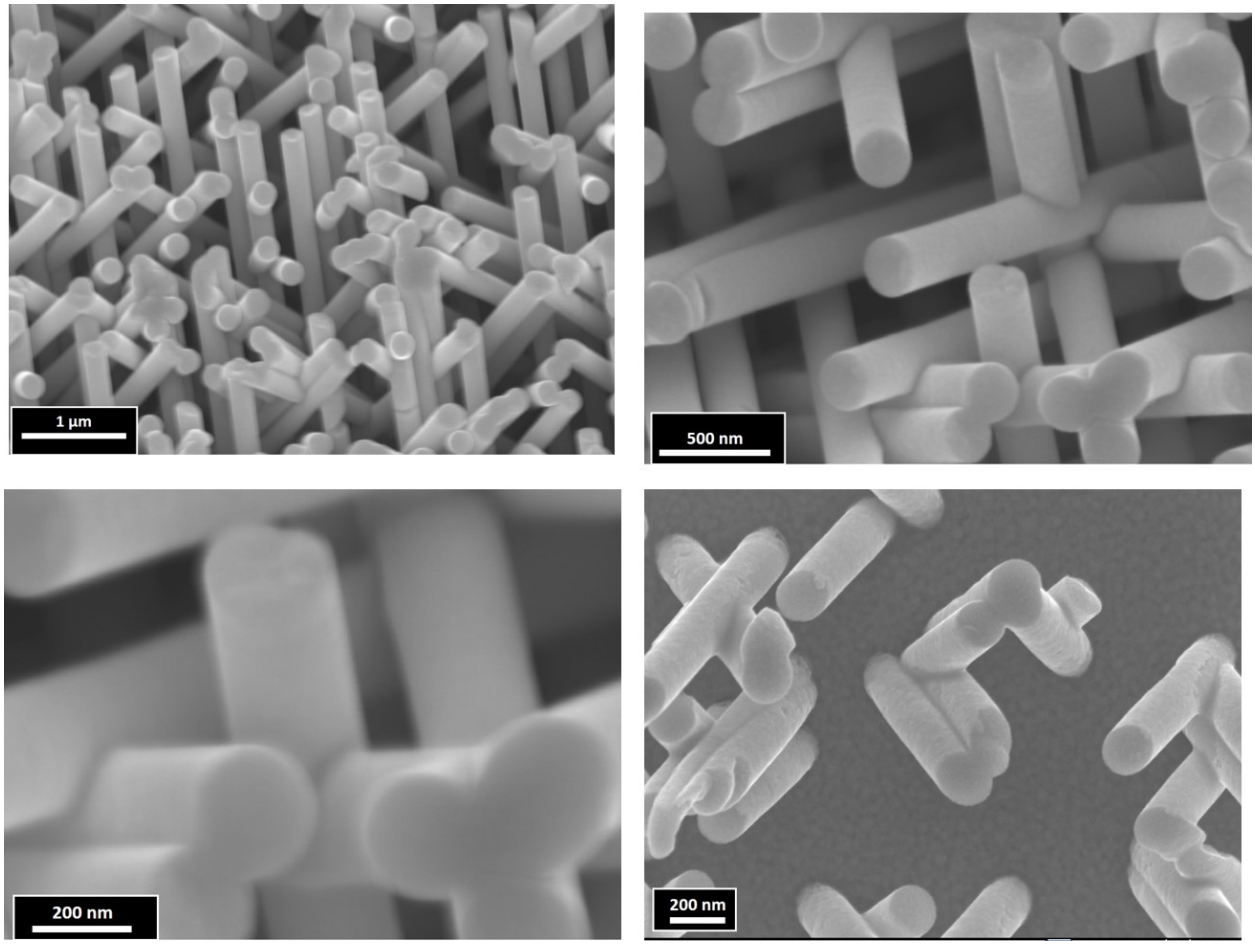

(b)

FIGURE 4.3: (a) $i-t$ profile of electrodeposited platinum nanowires; (b) SEM micrographs of the resulting nanowires; the bottom right micrograph is for nanowires electrodeposited to a charge of 1 C, in order to see the quality of adhesion of the nanowires onto the

Figure 4.3b shows the images of 10 C of Pt electrodeposited nanowires. The bottom right image is for 1 C (1 μm) at 25 °C throughout, in order to confirm the quality of adhesion of the nanowires on the substrate. As can be seen, the adhesion is of high quality if ECD is started at a low temperature.

4.1.3 Functionalization of Pt 3DNWN

After the fabrication of Pt 3DNWN, the next stage was the functonalization of the nanowires to the core-shell structure to determine the growth parameters that would result in the intended core-shell structure before reproduction on the interdigitated electrodes. The same setup as in the case of thin films were used, however with more careful handling to reduce the risk of nanowires detaching from the substrate. Electroless deposition was performed at 25 °C for 2, 4, 6, and 8 hours. Also, all samples used long after nanowire deposition were plasma-etched (with the same conditions as the Pt thin film before) before electroless deposition.

Figure 4.4 shows SEM micrographs of the 3DNWN core-shell network for PAni electrolessly deposited on Pt nanowires for 2 hours. It can be seen that PAni is uniformly deposited on the nanowires, with no exceptions, to form a clear core-shell structure. The resulting thickness of PAni shell over the nanowires is *50* nm.

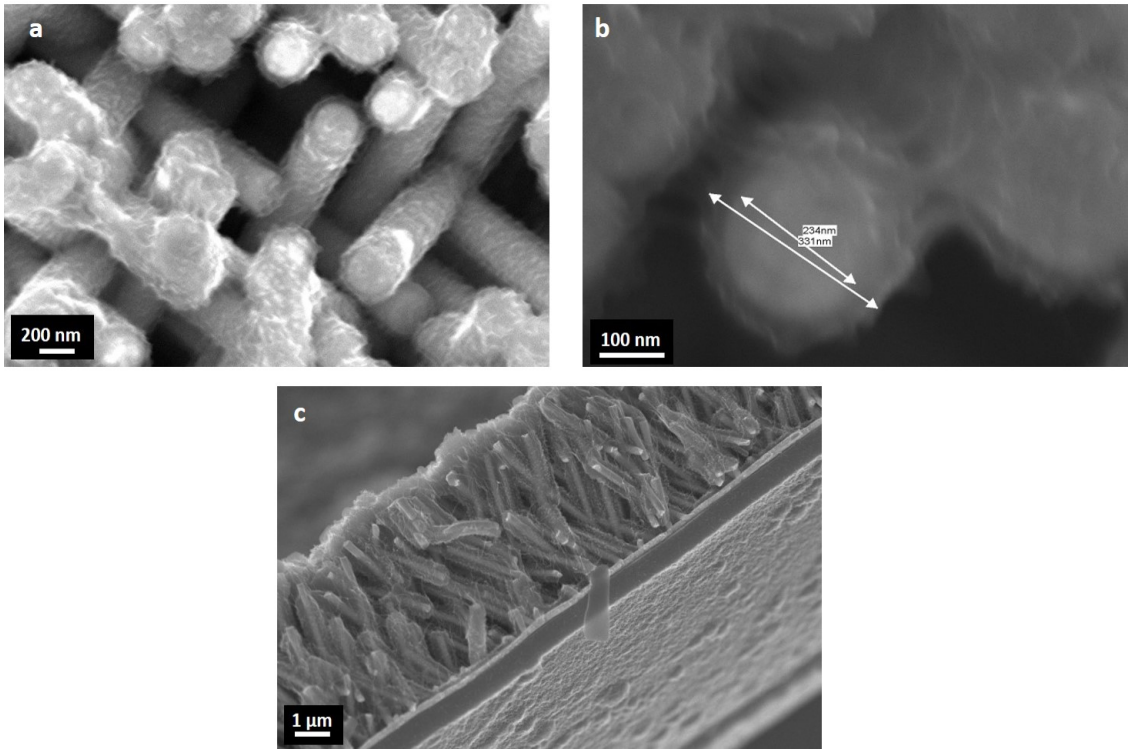

FIGURE 4.4: (a) Top view of functionalized Pt 3DNWN grown for 2 hours; (b) Magnification of functionalized Pt 3DNWN, showing the dimensions of the core-shell structure; (c) Side view of detached functionalized Pt 3DNWN deposited at 5 C to show that the the electroless deposition is uniform everywhere on the nanowire.

Figure 4.5 is the SEM micrograph for functionalization done in 4 hours. From the top view, bridging of PAni films from neighbouring nanowires can be observed in some regions; magnification shows that PAni doesn't fill up the entire sample, but only appears this way because of the interconnected nature of the nanowires. Within the network, there's still a lot of room for PAni while conserving the nanoscale structure of the core-shell nanowires. The thickness of the PAni shell in this case is *80* nm.

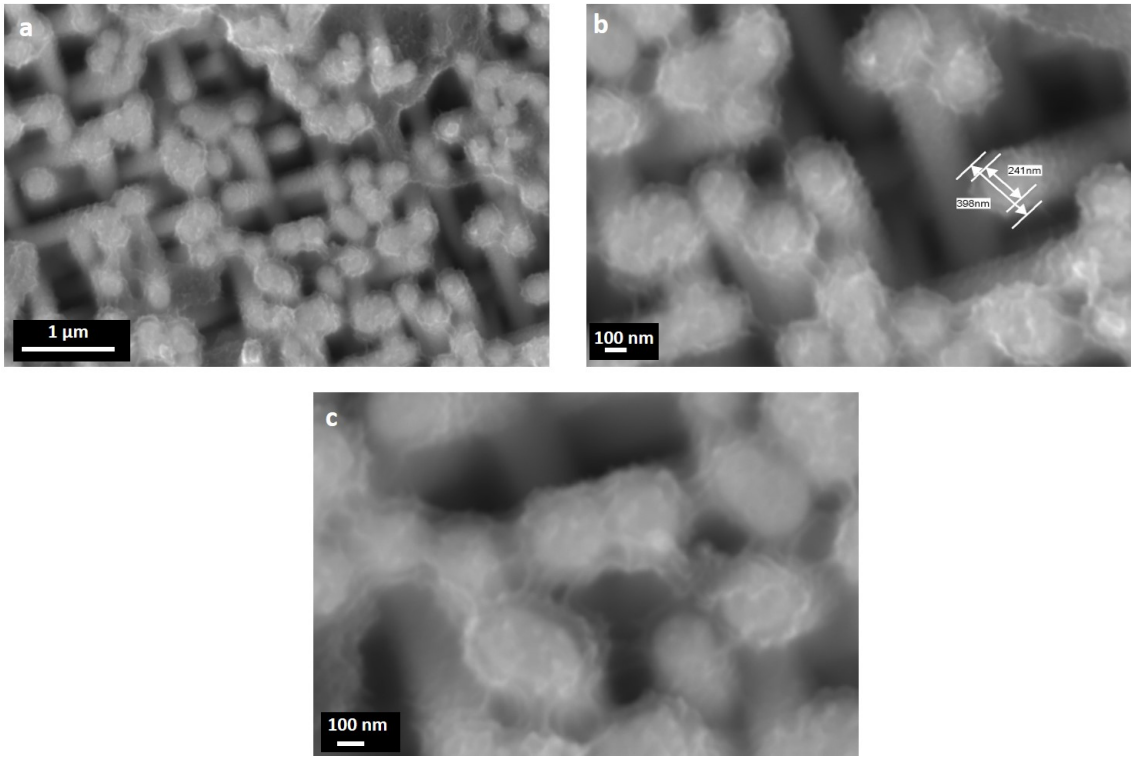

FIGURE 4.5: (a) Top view of functionalized Pt 3DNWN at 25 °C for 4 hours; (b) Magnification of functionalized Pt 3DNWN, showing the dimensions of the core-shell structure; (c) Larger magnification to accentuate to presence of ample room for PAni growth on the Pt nanowires in the volume.

Further deposition results in thicker shells as Figures 4.6 and 4.7 show; with time, complete merging of PAni shells, growing from neighbouring nanowires, occur. For PAni shell grown for 6 hours, again, the top view suggests that the entire volume is occupied, but the side view shows the presence of more room for PAni growth; however, as Figure 4.7 shows, further deposition of up to 8 hours leads to complete filling of the entire 3DNWN. Recall that for battery applications, the advantages of nanostructures, i.e., simultaneously having high energy and power density, is hoped to be explored; when the PAni shell is very thick, as in Figure 4.7, so much so that the 3DNWN core-shell is effectively a thick film, the resulting energy density will be certainly high, but at the cost of its power density, as the diffusion length for ions becomes considerable; hence, there is no need to grow PAni for a longer duration with this template. The thickness of PAni shell grown for 6 hours is *121* nm and *65* nm for that grown for 8 hours.

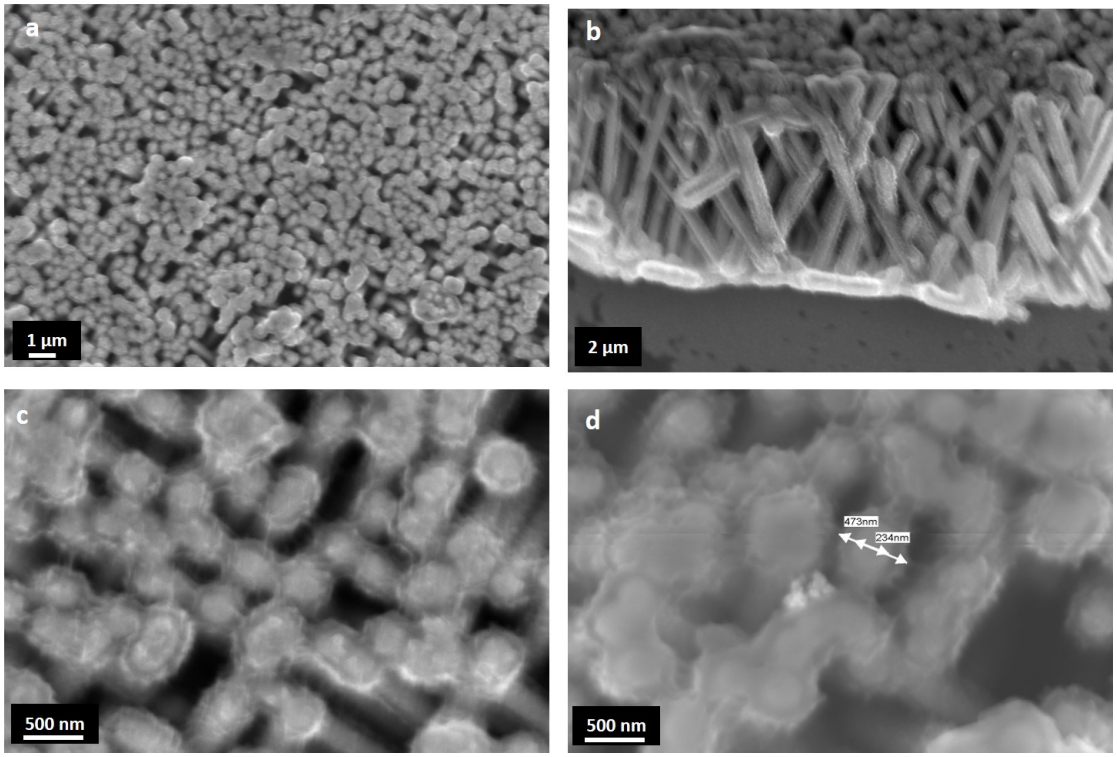

FIGURE 4.6: (a) Top view of functionalized Pt 3DNWN grown for 6 hours at 25 °C, showing further bridging of PAni core from neighbouring nanowires; (b) Side view of functionalized Pt 3DNWN, showing the presence of ample space for further PAni growth (c, d) Larger magnification to accentuate the presence of room for PAni growth on the Pt nanowires in the volume and the dimensions of the core-shell structure.

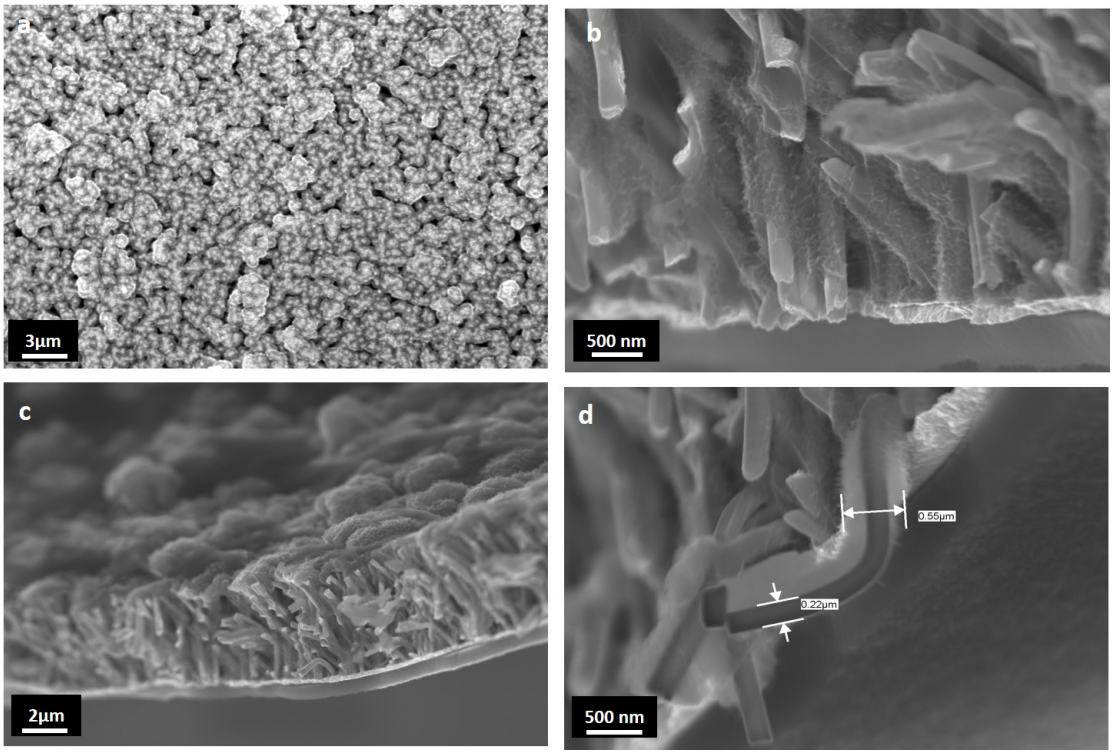

FIGURE 4.7: (a) Top view of functionalized Pt 3DNWN, which shows that the entire 3DNWN is almost completely filled with PAni; (b–d) Side views, at various scales, of the 3DWNW, to accentuate filling even within the network.

4.1.4 Laser-assisted patterning of Pt 3DNWN to side-by-side interdigitated electrodes and functionalization of the electrodes

It was agreed upon that the test system would be the core-shell 3DNWN with 50 nm shell. Before functionalizing the 3DNWN, it was first patterned to form side-by-side interdigitated electrodes, because patterning after functionalization leads to burning away of PAni shell, a polymer.

Figure 4.8 shows the optical micrographs of the Pt 3DNWN after patterning. It can be seen that the exact dimensions intended, as shown in Figure 3.6b was achieved. In addition, the separation between electrodes (100 μm, the same as the separation between consecutive digits) can be seen in Figure 4.8a; the substrate was ablated to its extrema – this was done to avoid electrical contact between the interdigitated electrodes, so short circuiting wouldn't occur during battery operation. The patterned samples were tested with a multimeter to ensure this.

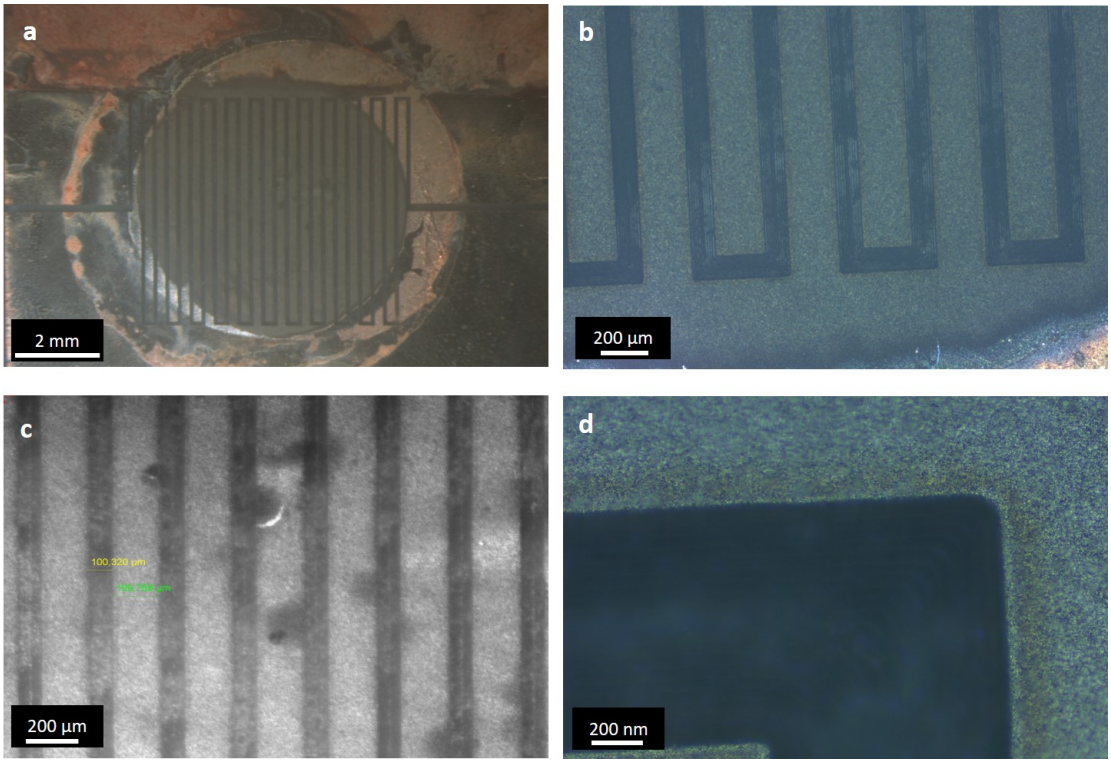

FIGURE 4.8: (a–d) Optical micrographs of LASER-patterned interdigitated electrodes of Pt 3DNWN before PAni functionalization.

The SEM micrographs of same are shown in Figure 4.9 to accentuate the heat-affected zone (HAZ); it can be seen that the HAZ is no more than 4 μm for each digit, with very sparse recasting of the ablated material, just as was claimed in Section 3.6. Therefore, we can be certain that the effect of patterning on the performance of the battery will be very negligible.

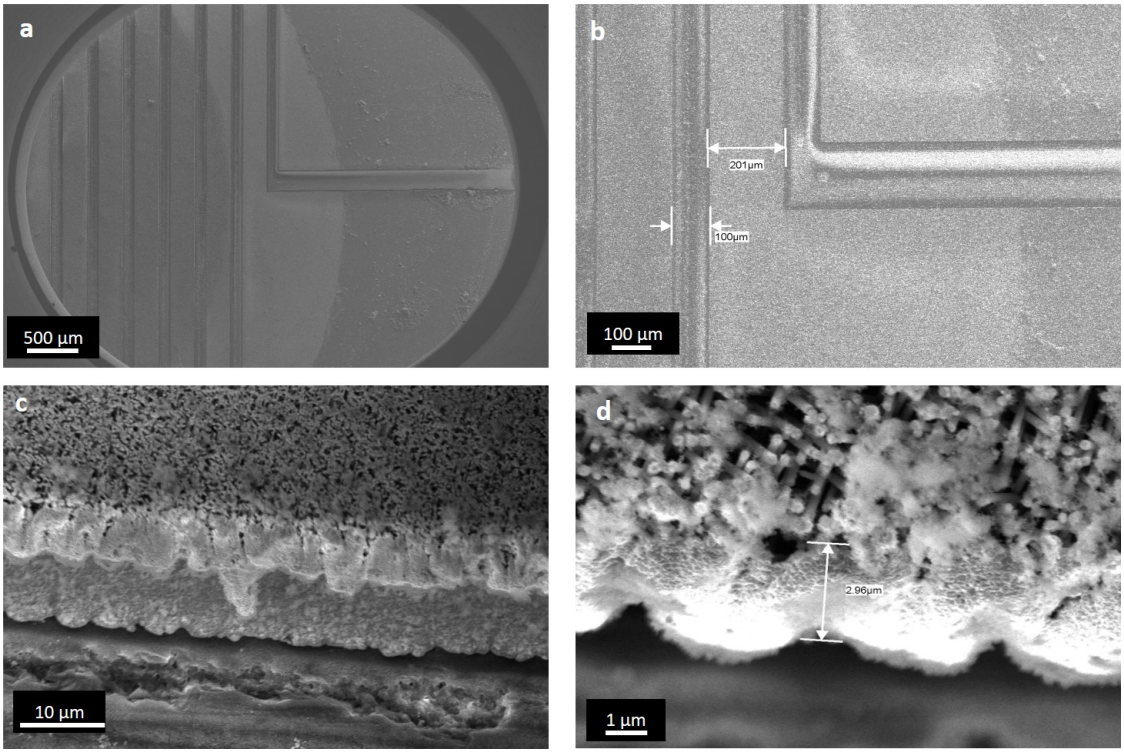

FIGURE 4.9: (a–d) SEM micrographs of LASER-patterned interdigitated electrodes of Pt 3DNWN before PAni functionalization.

After LASER patterning to form the side-by-side interdigitated electrodes, the next stage was the functionalization of the Pt 3DNWN by to form the core-shell structure. Figure 4.10 shows SEM micrographs after PAni functionalization at different magnifications; because of the difficulty with taking high-quality images after PAni functionalization, a very thin film of 5-nm (Au) was sputtered on the sample to make it more conducting. Nevertheless, from the diameter of each nanowire, it's obvious that there's a PAni shell, and the circled regions in the image show regions in which the Pt core is evident. It should be noted that no cell cycling was done on this system; it was only done to show that Laser-patterning has no effect on PAni electroless deposition on the nanowires.

In all cases, after PAni functionalization, gentle rinsing with distilled water is required because some conducting emeraldine salt crystals bridge the electrodes. A single tiny crystal in any of the electrical-separation troughs is enough to cause this, as unaided visual observation and multimeter-testing have shown. It's imperative to note, however, that one has to be very careful in doing this, lest the nanowires be delaminated from the substrate. Typically, the sample is put in a beaker containing distilled distilled water, gently stirred to remove any crystals from its surface, then brought out and allowed to dry in the fume box. Finally, Table 4.2 compares the thicknesses of PAni grown on the Pt thin film and nanowire, while Figure 4.11 shows an image of the battery, with connections, before packaging for cycling tests. Silver paint was used to attach copper wires that connect the

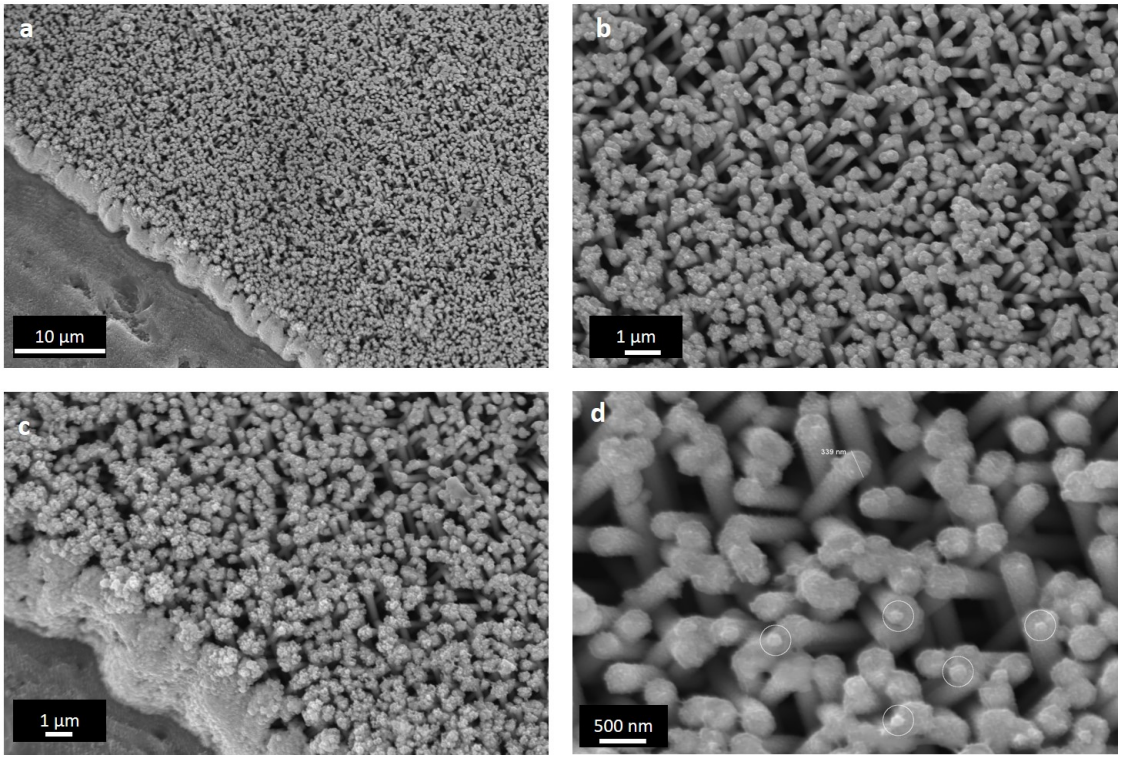

FIGURE 4.10: (a–d) SEM micrographs of LASER-patterned interdigitated electrodes of Pt 3DNWN after PAni functionalization.

battery to the battery testing system, and the green colour on the Au substrate is PAni electrolessly deposited on Au.

TABLE 4.2: Comparison of PAni thickness on 3DNWN and planar substrate electrolessly deposited at 25 °C

Deposition time (hours)	Thickness on planar Pt substrate (nm)	Thickness on Pt 3DNWN (nm)
2	42	50
4	50	80
5	94	
6		121
8		165

4.2 Electrochemical Tests

In this section, results and discussion of electrochemical tests will be presented. Where relevant, links from the preceding section will be made and expounded.

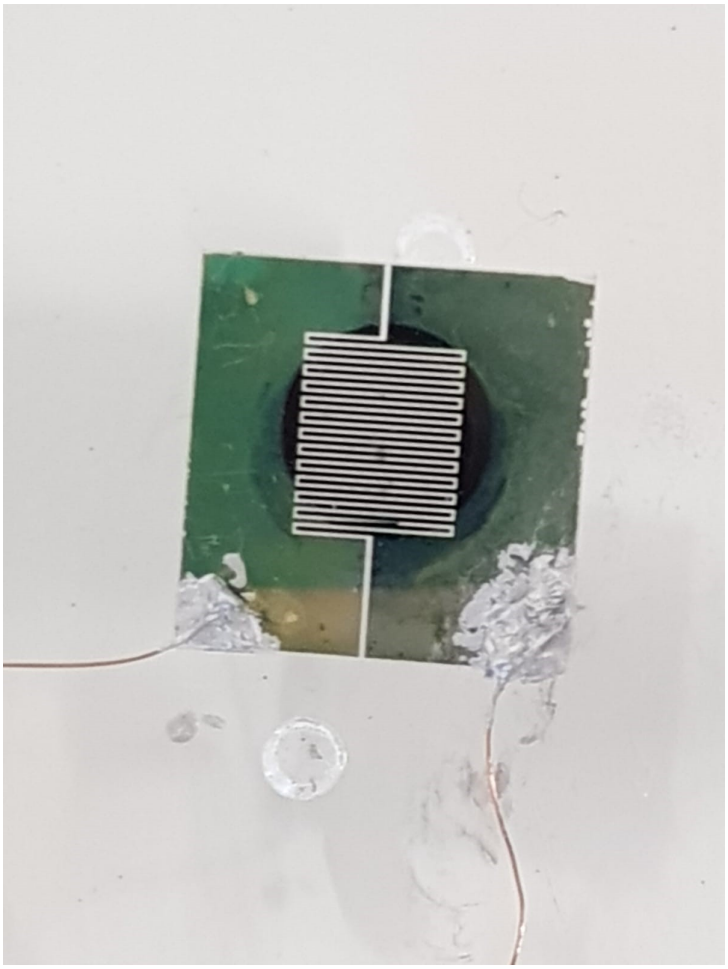

FIGURE 4.11: Image of symmetrical 3D battery with functionalized electrodes ready for galvanostatic cycling testing.

4.2.1 Cyclic voltammetry (CV) on PAni film in aqueous electrolyte

In the search of an electrolyte for our PAni microbatteries, it was expected that an aqueous electrolyte would do, because of the values of the redox potentials[1], and the narrow potential difference expected of the PAni battery. In light of this, CV was done on a thin film of PAni (PAni used was electrolessly deposited at 25 °C for 5 hours) in 1 M H_2SO_4 aqueous solution; as we have seen, the thickness of this film is 94 nm[2]. Figure 4.12 shows the resulting voltammogram:

The CV was performed multiple times as Figure 4.12 shows. There are two salient points from the voltammogram. The first is the presence of a mid-redox state at about 0.58 V (labelled B-B'); this has been ascribed to the formation of quinones (mostly benzoquinone) as a consequence of the hydrolysis (of emeraldine) in water in the following reaction [90–92]:

[1]The redox potentials of PAni oxidation and reduction.

[2]It should be stated that during the course of this work, CV was attempted on $\sim$ 40-nm PAni film, but no peaks were evident.

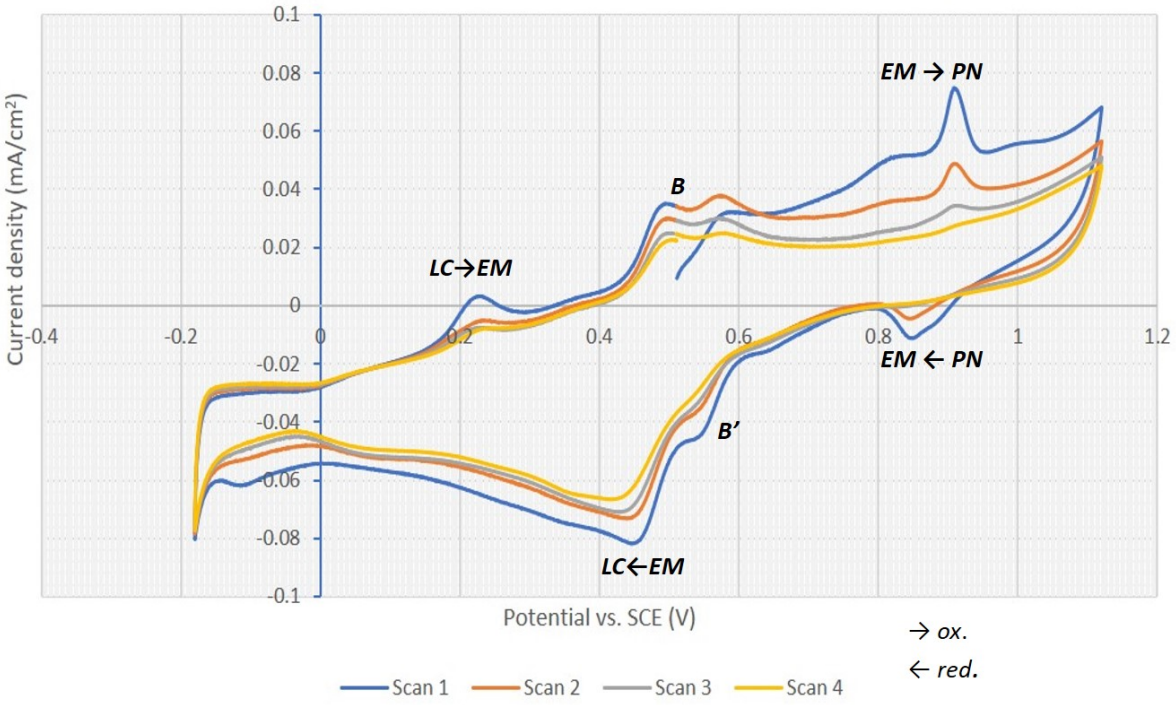

FIGURE 4.12: Cyclic voltammogram of PAni in 1 M H_2SO_4 aqueous solution at a scan speed of ν of 5 mV/s.

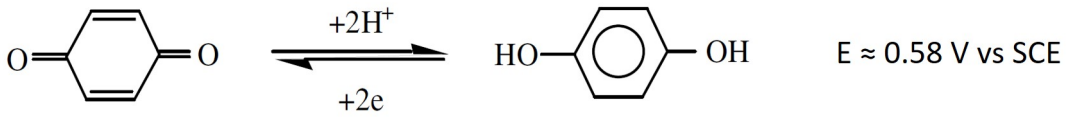

The second point is the sharp disappearance of the EM/PN peaks with further scans; this is likely a result of hydrolysis. To see why these degradations might occur, consider Figure 4.13 – called a Pourbaix diagram – which shows the potential stability window of water with pH at 25 °C; it can be easily derived for any temperature by the solution of the Nernst equation (Equation 2.6), considering the autoionization of water. Because the potential of the Pourbaix diagram is quoted vs. SHE, the the potential of Figure 4.12 has to be increased by 0.241 V, making the potential at the EM/PN peak 1.141 vs. SHE. Although it is expected that water is stable at this potential, the possibility of the oxidation of water at the EM/PN potential is still obvious, especially if the pH of the aqueous solution shifts to a higher value, which is usually the case in CVs done in aqueous electrolytes [93]. In any case, even if the pH were perfectly controlled during CV, and no decomposition occurred, the presence of an oxidation product besides EM/PN precludes the use of an aqueous electrolyte, because the symmetrical battery may then have to run on a lower potential. This is undesirable.

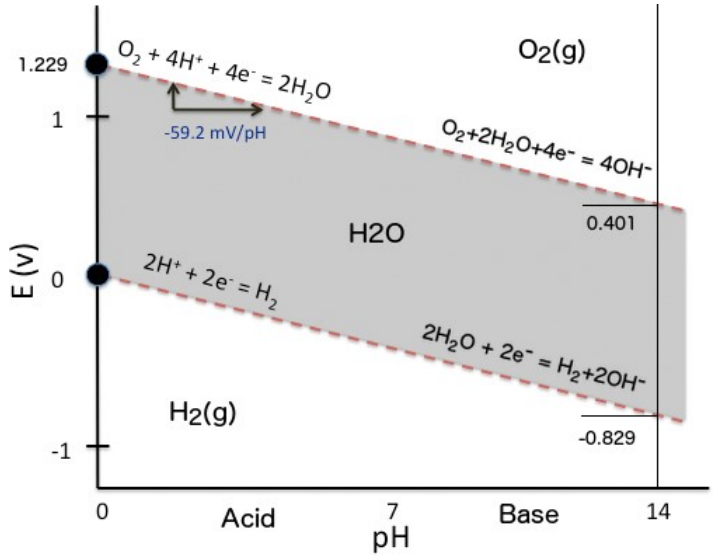

FIGURE 4.13: Pourbaix diagram for water at STP. The potentials are relative to SHE.

Consequently, the presence of a mid-redox state, which can lead to complexities in the operation of a PAni battery, and the degradation of the film with time, rules out the possibility of making an aqueous electrolyte-based PAni battery, as both of these factors will expectedly lead to loss of substantial capacity with battery cycling.

4.2.2 Cyclic voltammetry on PAni film in non-aqueous electrolyte

Following the realization that an aqueous electrolyte isn't useful for our purpose, CV was performed again, this time in a non-aqueous electrolyte. Figure 4.14 shows the result of the cyclic voltammetry performed on a sample containing 94-nm thick PAni film with a surface area of 0.81 cm^2 in 1 M $LiClO_4$ solution; this particular test was carried out in an open cell, not in the glove box; thus, the gradual disappearance of the pernigraniline oxidation peak is most likely an effect of the oxidation of water, which must have contaminated the electrolyte solution, just as described in the previous section. Although the pH of the contaminating water is unknown, it should be obvious that this possibility is, in fact, more and more likely at pH values that would be expected of ambient conditions. The degradation is not as abrupt as in the previous case, so we can be confident of its applicability in our battery. We shall soon see that this is indeed the case.

Now, to the matter at hand. The presence of two pairs of cathodic and anodic waves is evidence of two reversible, charge-transfer reactions within the potentials swept – -0.4 V to +1.2 V. A host of information about the nature of the redox processes at the peaks on their own or relative to each other can be determined[3]. First, we can define the usual standard electrode potential $E^{\circ}_{half-cell}$ (as described in Section 2.2.1). Recall that in Section

[3]The second scan is used for analyses here.

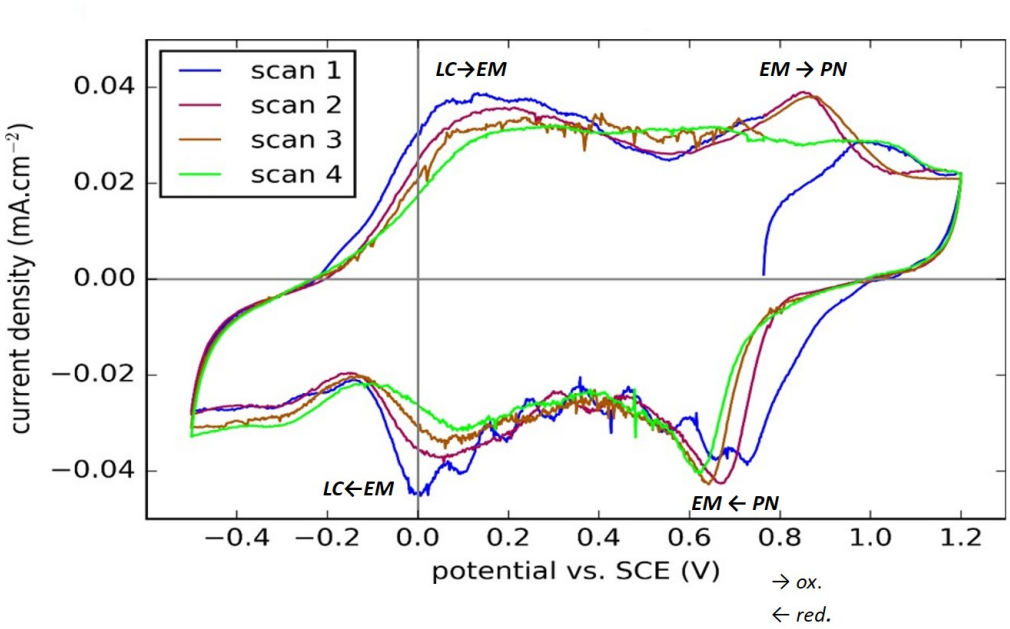

FIGURE 4.14: Cyclic voltammogram of PAni in 1 M $LiClO_4$ electrolyte in acetonitrile at a scan speed ν of 5 mV/s.

2.2.3, it was stated that midway between peak potentials $E_{1/2}$ is a good approximation of the electrode potential, causing $E_{1/2}$ to be used in practice to determine the electrode potentials; hence, from Figure 4.14, the standard electrode potentials for the different redox couples of PAni are *+0.76 V* for the *EM/PN* redox couple and *0.105 V* for the *LC/EM* redox couple, both vs. SCE. Since SCE is +0.241 V vs. SHE, then $E^{\circ}_{half-cell}$ of both states are +1.0 V and +0.346 V vs. SHE, respectively. Consequently, any stable battery made using the PN/EM redox couple at the cathode and EM/LM at the anode will have an E°_{cell} of 0.66 V.

Furthermore, this large value of $E^{\circ}_{cell} \gg 125$ mV implies that the successive electron transfer reactions involves a singular molecular orbital, and that no large structural changes occur upon electron transfer [35]. The CV can also give information about the nature of the reversibility of the processes. One of the hallmarks of reversible electrode processes is the ratio of the cathodic and anodic peak currents: in reversible processes, the ratio of the peaks is 1; thus

$$\frac{I_p(c)}{I_p(a)} = 1. \tag{4.1}$$

The difficulty now lies in determining these values for our CV; typically, the peak current of a redox peak is measured relative to the decaying current of the preceding peak by an experimental methods that "separates" the peaks to distinct ones by stopping the scan at the first peak, allowing the current to decay on its own to a small value, then continuing the scan and using the freely decayed peak as the baseline [35]. However,

a much simpler, acceptable method would be assuming that the peak current decays proportionally with $t^{-1/2}$ [35, 94]; since $E \propto t$, then it implies an $E^{-1/2}$ decay, too. In the following sections, we shall use another method, because this experiment was not carried out during the course of the work.

Now that we think a non-aqueous electrolyte might be useful, we have to determine the stability window of the electrolyte to be certain that the electrolyte will be stable within a potential window of 0.66 V and at the potentials of the redox couples. Linear sweep voltammtery was used, as was described in Section 3.5. The resulting voltammogram is shown in Figure 4.15. Since the test was cariied out in a glovebox, a Swagelok cell, with an Ag wire pseudoreference electrode was used. There are no specifc standards for determining the stability window of an electrolyte from the voltammogram [95], but the generally used values are potentials at $\pm$ 1 mA/cm^2; therefore, stability window of the electrolyte is about 4.4 V.

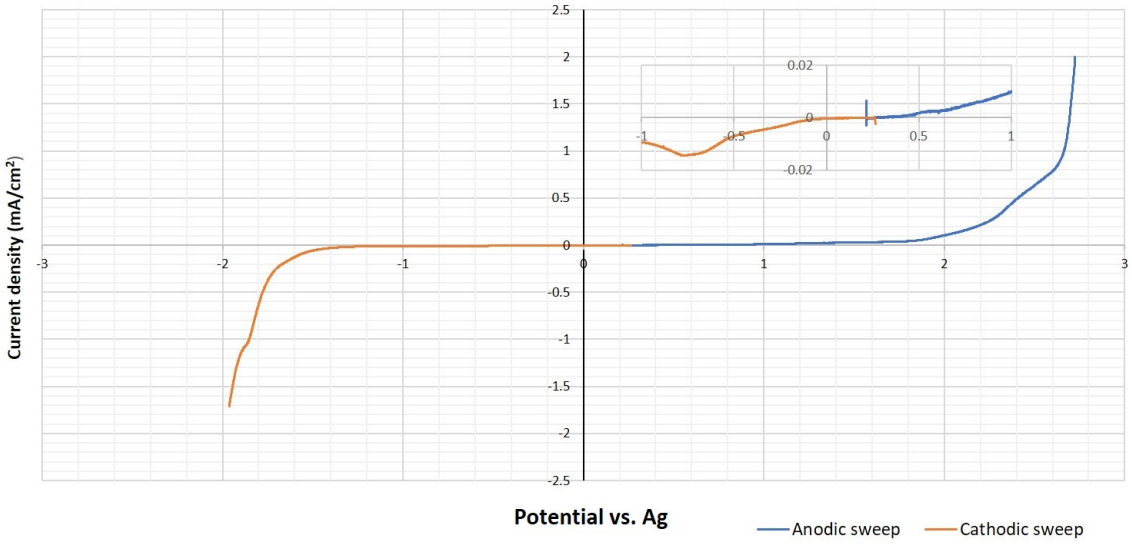

FIGURE 4.15: Stability window of 1 M $LiClO_4$/acetonitrile electrolyte. The potential is vs Ag, a pseudoreference electrode, and ν is 10 mV/s

Finally, we consider the CV for PAni with our electrolyte at various scan rates. Recall Equation 2.20; it shows the relationship between the peak current and scan rate; this relationship is called the *Randles-Sevcik* equation; it implies that, for a reversible redox process, a plot of the peak current vs. square root of the scan rate should give a straight line. In addition, if the peak potentials (i.e., the potentials at the peak currents) appear to be sliding apart as a function of scan rate, the process is quasi-reversible, not reversible. Irreversibility is not in question here, as we see two clear pairs of oxidation and reduction peaks from previous CVs [35, 41].

To ascertain the nature of the reversibility of our PAni films, CV was done in varying scan rates, as shown in Figure 4.16. Again, it was performed in a Swagelok

cell that had been assembled in a glove box to avoid any influences of humidity, and a pseudoreference electrode, Ag wire, was used. While we see no decomposition of the electrode, the oxidation peaks are not well separated.

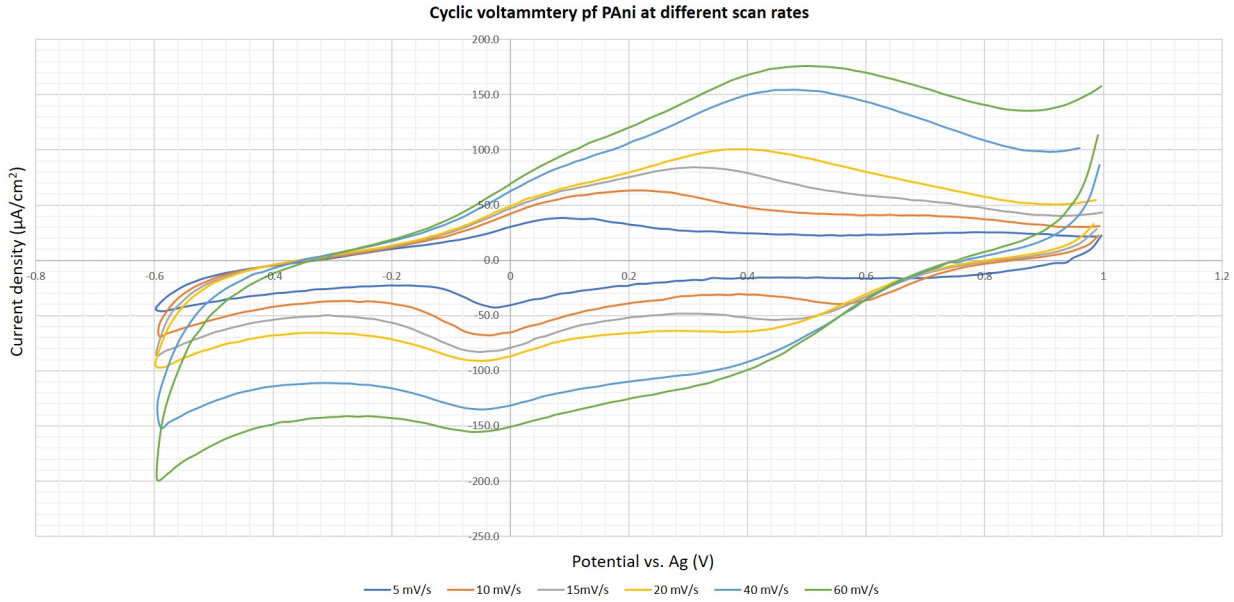

FIGURE 4.16: Cyclic voltammetry of PAni in 1 M $LiClO_4$/acetonitrile electrolyte at variable scan rates. The scan for every ν was performed thrice, but only the second scans of each ν has been presented for clarity.

Nonetheless, we can still make conclusive judgements about the nature of the redox processes in PAni. Recall that Section 2.2.3 gives the characteristics of CVs that determine the nature of reversibility of redox processes. Besides the peak current ratio being 1, it was also stated that, (1) an increase in the scan rate has no effect on the peak potentials, and (2) $\Delta E_p = \frac{2.3RT}{nF}$ for reversible redox processes. It should be clear to the reader by now that the transitions between PAni redox states involve two electrons; thus, on the latter condition, considering that the CVs were performed at 20 °C (313 K), we should expect that ΔE_p is 0.031 V, if the redox processes were reversible. But as Figures 4.14 and 4.16 show, ΔE_p is higher than this value. On the former condition, we can also see that ΔE_p is not constant but varies with the scan rates.

Therefore both redox processes, corresponding to two the pairs of waves in the CV, are *quasireversible*, i.e., the redox process are electron-transfer limiting. Clearly, this fact will have effects on the performance of our battery, as we shall soon see.

4.3 Battery Performance

The next stage after fabrication of battery, determination of the potential window within which our battery can operate and the suitable electrolyte, the battery components were

assembled and its performance evaluated. Galvanostatic charge-discharge voltage profiles were determined for three different symmetric full cell geometries containing thick film electrodes, thin film electrodes, and the interdigitated electrodes. The characteristics are now presented.

4.3.1 Symmetrical thin-film microbattery

The thin-film battery, whose electrodes contained 50-nm PAni film, were assembled in a coin cell, as described in Section 3.7; in general, the areal capacity in charge and discharge are, as one would expect, small, since the mass of active materials is small. Figure 4.17 shows the performance of symmetric PAni thin-film battery cycled at 20 C (2.5 μA/cm^2). Smaller current densities were tried, but all led to poor cycling characteristics, typical of electrolyte decomposition, so the current density was increased until the effect of electrolyte decomposition was negligible.

It can be observed that the specific capacity is constant at a value of 0.09 μAh/cm^2 for more than 200 cycles. Almost no capacity fading was observed until the test was stopped. Furthermore, the current efficiency improves with the number of cycles and remains at $\sim$ 98 % for for the rest of its cycle life.

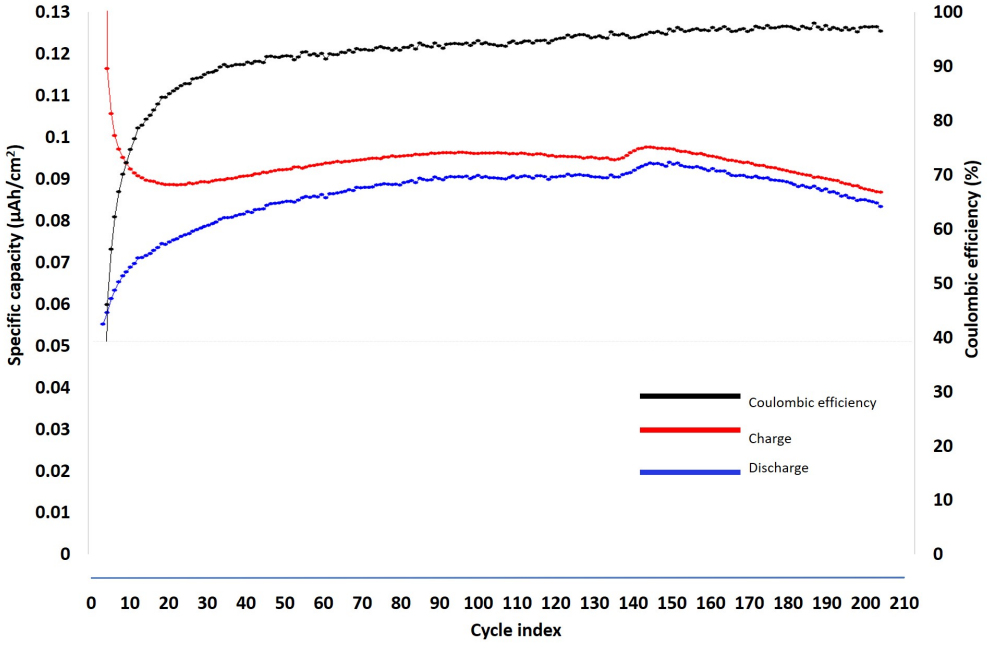

(a)

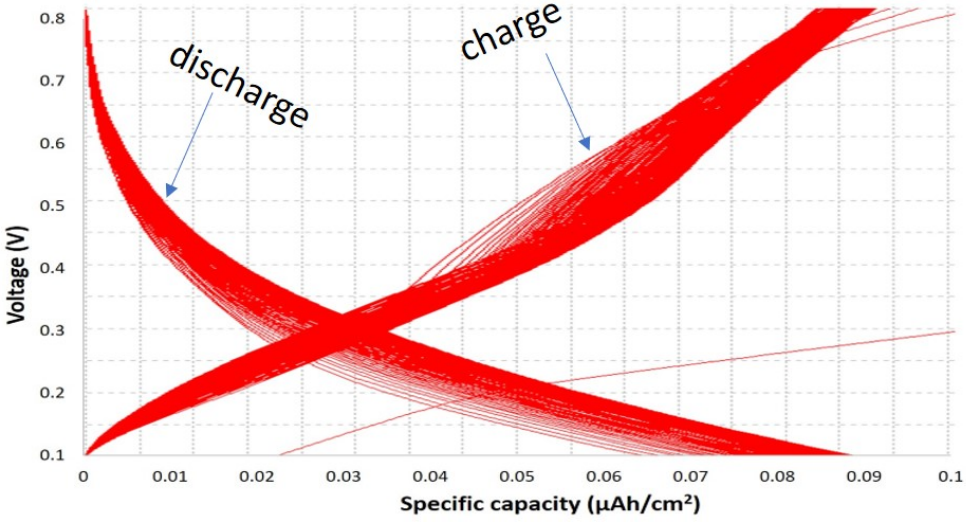

(b)

FIGURE 4.17: Performance of symmetric PAni thin film battery cycled at 20 C (25 μA/cm^2): (a) Charge cycle life; (b) Discharge cycle life; (c) Current efficiency of charge-discharge capacities; (d) Voltage profiles for the first 200 galvanostatic cycles.

Furthermore, also evident in all of Figure 4.17 is an increase in capacity during the first 130 cycles before slowly decreasing. This fact is most accentuated in Figure 4.17b, which presents the voltage profile for the first 200 cycles. In addition, the s-shape profile – typical of many batteries in the bulk – is not observed until after the first 20 cycles or so. The presence of this in galvanostatic experiments (in LIBs, for instance) is an indication of *phase transitions* [96]. Because of the paucity of literature on this, it's not so clear why

this happens, but it's fortuitous enough that the battery performs better with time. Any suitable structural characterization method should make clear what is happening.

The discharge profile, corresponding to rapid discharge, is as expected for a nanostructured electrode [59, 96, 97]; it results from the ion and electrons' paths been considerably shortened, as has been stated in previous chapters. Finally, the SEM micrographs after 1000 cycles of the thin films are shown in Figure 4.18. No substantial degradation of film, as compared to Si, for instance, [98], is observed. This explains its impressive stability with cycling.

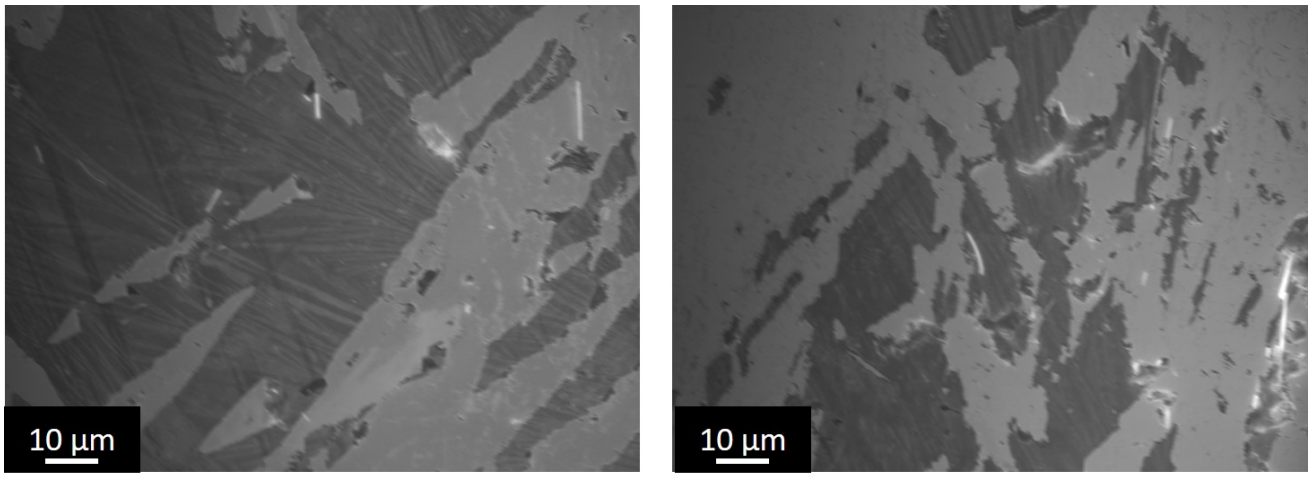

FIGURE 4.18: SEM micrographs of thin-film electrodes after 800 cycles.

4.3.2 Symmetrical 3D microbattery

Now, we consider the result to which this work has been culminating. Symmetrical 3D microbattery, as a reminder, refers to the battery with interdigitated electrodes of Pt_{core}-$PAni_{shell}$ 3DNWN. As has been noted in the opening of this section, the assembly of the cell for cycle testing of the interdigitated electrodes was somewhat challenging and required lots of care to reduce the possibility of nanowire delamination.

Figure 4.19 presents the cycle life curve for the battery made of interdigitated electrodes. To aid the reader with interpretation of results, Table 4.3 is presented to shows the actual current densities and cycle ID corresponding to each C-rate. Note that the current density are based on the footprint area of the electrodes, and that the C-rates stated are not based on the *theoretical* capacities, since we have no access to this at this point, but based on actual experimental data[4]. The behaviour at 20–25 cycles is an artefact.

[4]Simply put, the C-rates were gotten by checking the time it took to attain the highest capacity for each imposed current density.

TABLE 4.3: Corresponding current densities and cycle indices for C-rates shown in Figure 4.19

C-rate	**Current density** (μA/cm^2)	**Cycle ID**
1.4 C	3.85	1–76
4 C	7.69	77–81
8 C	15.35	82–86
20 C	38.46	87–91
50 C	76.92	91–95
100 C	153.84	96–100
250 C	384.62	101–105
1.4 C	3.85	106–121

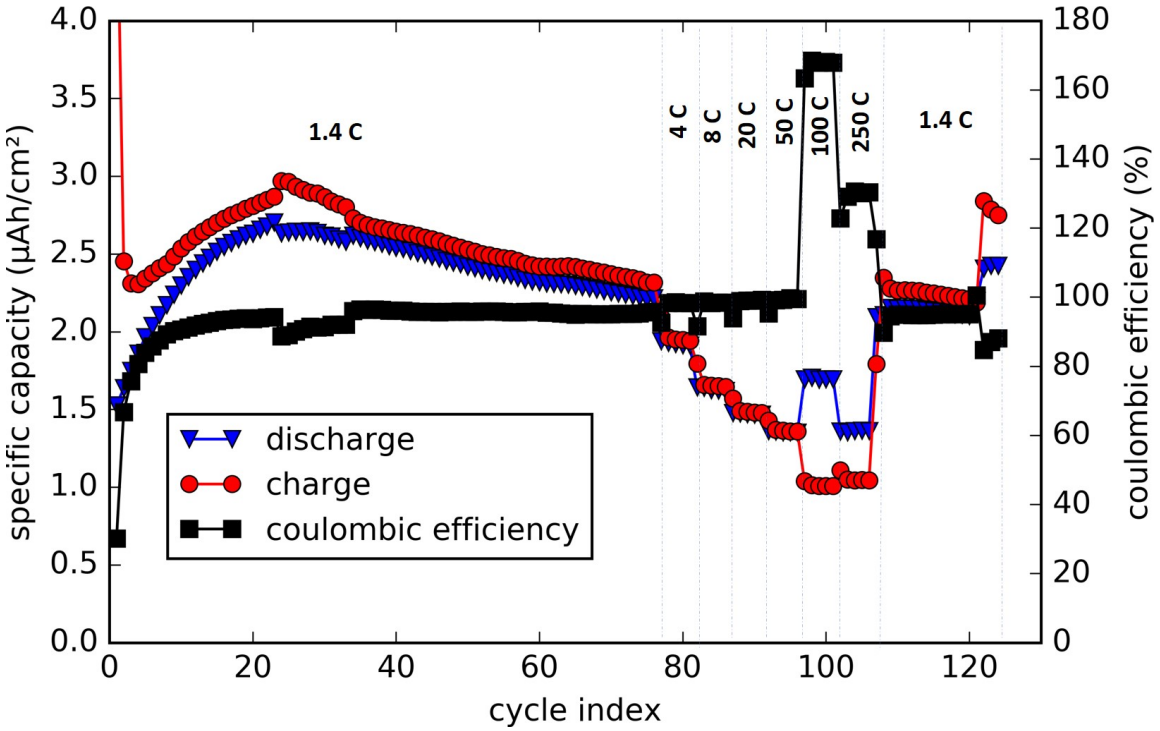

FIGURE 4.19: Cycling performance of symmetrical 3D battery.

Before the discussion of the results, it's important to note that smaller current densities of 0.77 μA/cm^2 ($\sim$C/3) and 1.54 μA/cm^2 ($\sim$1 C) were initially used for cycling, but only electrolyte decomposition was observed. For a likely explanation, consider the inset of Figure 4.15; it suggests that at such tiny current densities, decomposition of the electrolyte might be possible: this is because a small current density implies a longer exposure of PAni to the electrolyte, causing reactions that normally wouldn't occur. This effect is even more amplified now that the electrodes are made of nanowires that present

larger surface area-to-volume ratios. These unfavourable results led to using the higher current densities presented here.

A number of observations can be made from Figure 4.19. The first is the occurrence of an irreversible capacity loss (of 5.05 μAh/cm^2) after the first charge at 1.4 C. Again, the foregoing argument, if true, might apply, as there's usually an irreversible capacity loss, on the first charge, associated with the formation of reaction products when electrode-electrolyte reactions occur [86, 99]. A common example of this is the formation of a solid-electrolyte interphase (SEI) in alkali-metal batteries. In so far as the author is aware, there's been no such reports for PAni/$LiClO_4$-acetonitrile systems – but then, most reports on PAni electrodes use it in the bulk and at much higher current densities. Another possibility is an imbalance in the capacities of the electrodes; since the electrodes are symmetric, it corresponds to difference in the areas of the electrodes. To understand this, consider a cell with electrodes of different capacities; in the first charge, the overall capacity of the cell is less than the capacity of *both* electrodes; in the first discharge, the capacity of each electrode is then limited to the smaller capacity during the first charge, resulting in an overall cell capacity less than the first charge's. All things being equal, the charge-discharge capacities should remain the same in subsequent cycles. This is similar to what is observed in Figure 4.19. It's not conclusive to the author which it is, but further studies, taking care to *perfectly* fabricate and assembled cells, should solve the quandary.

Furthermore, it can be observed that higher C-rates (from 100 C) present unsatisfactory coulombic efficiencies; this can't be simply dismissed as some error in measuring-devices, as it is evident in *all* cycles of the instances in which they occur. Charging and discharging at high currents imply that not all the capacity can be accessed, but there's no reason to think they should be accessed to the same extent in the different respective electrodes. Besides, for a battery, whose capacity is hoped to be utilized, it's never a good idea to cylce at greater than 60 C [96], as it becomes more difficult to access its full capacity. Of course, it would be a whole different matter if we were testing a capacitor.

Similar to what we have seen with the thin films (see 4.3.1), the s-shape of the galvanostatic charge profile (Figure 4.20) appears after about, again, the 20th cycle, in the neighbourhood of the maximum capacity at the 1.4 C cycling rate; also, it loses capacity with cycling, albeit very slowly.

Nevertheless, two excellent points can be be observed in the performance of the battery, as both of Figures 4.19 and 4.20 show. First, the battery is very stable, and this is obvious when you consider the second cycle at 1.4 C: it suggests that if the battery had been left at 1.4 C, the capacity loss would have been negligible with each cycle. Going by the standard of defining the cycle life of a battery as the number of cycles it takes for their capacity to fall below 80 % of their initial capacity [34], it's clear that we are still very far away from the end of the battery of our battery's cycle life. The second point

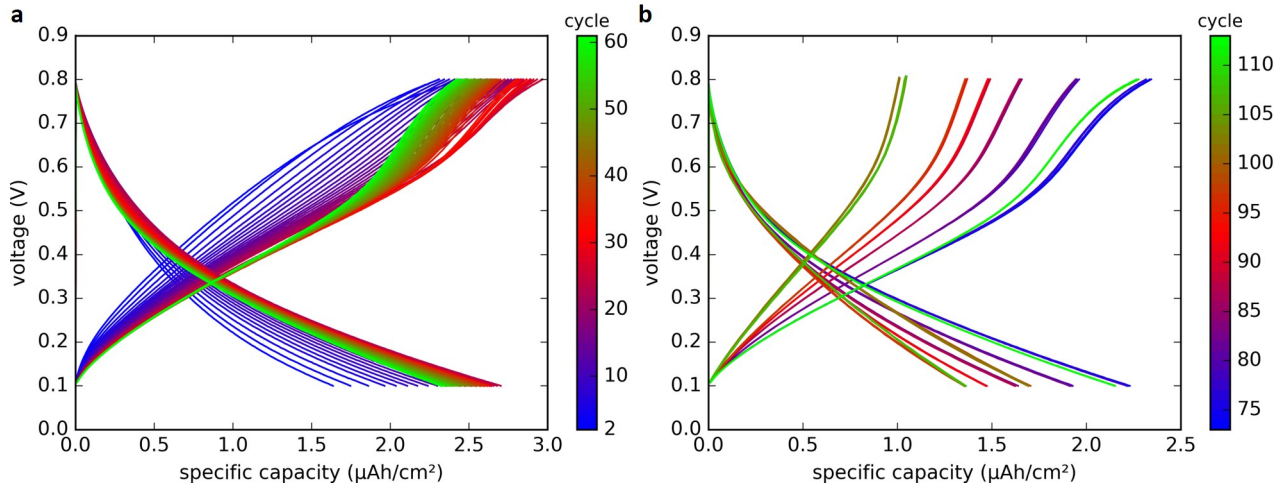

FIGURE 4.20: Galvanostatic voltage profile for symmetrical battery with interdigitated 3DNWN electrodes for (a) First 65 cycles; (b) 66th to 121st cycle.

is that the decrease in the accessible capacity with cycle rates isn't very pronounced; for comparison, a battery, with a Ni_{core}-NiO_{shell} nanowire anode cycled against Li metal [78], lost two-thirds of its initial areal capacity when the C-rate increased by a factor of 10, while our own battery loses only one-sixteenth of its initial areal capacity for the same increase in C-rate. This goes to show that our battery can deliver optimally in applications requiring wide-varying cycle rates. This is a combined consequence of nanostructuring and the interdigitated nature of the electrodes.

Figures 4.19 and 4.20 show that the maximum discharge capacity in this case is 2.7 μAh/cm^2 at 1.4 C, 31 times more than the thin film batteries. The author has, with exhaustive calculations that account for porosity, inclined nature of the nanowires, etc., derived that the expected areal-capacity increase should be by 58 times. The lower value likely results from the large cycling current densities that make it difficult to access the batteries' full capacity, and the possibility of nanowire delamination during cycling. Finally, it can be observed from Figure 4.21 that the nanowires undergo only very little change, even after over 200 cycles. This proves the excellent cycling stability that has been observed from the cycle life curve.

4.3.3 Symmetrical thick-film Battery

Finally, PAni thick film batteries were tested in order to compare the power characteristics with the other two batteries. The thickness of the film was such that it would give the same capacity[5] as the interdigitated electrodes. It was determined from the data that this would require about 2 μm of PAni. The growth conditions for PAni thick films are reported in refs. [75] and [70].

[5]Not *specific* capacity, which, in retrospect, should have been a better idea.

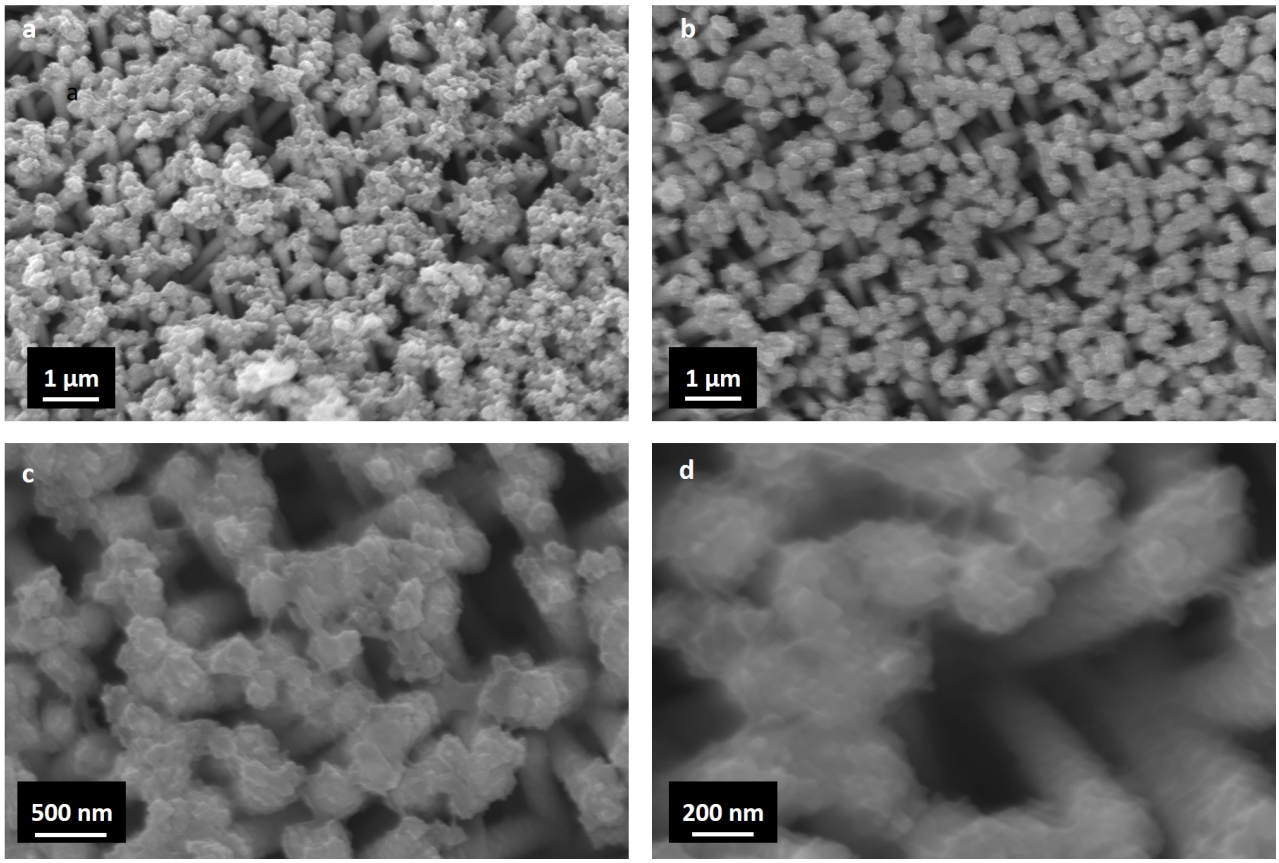

FIGURE 4.21: (a–d) SEM micrographs of 3DNWN electrodes after 200 cycles. Note that 5-nm of Pt was sputtered on it to improve its conductivity for SEM imaging.

Figures 4.22 and 4.23 present the cycle life characteristics and the galvanostatic voltage profile, respectively, for the symmetrical thick-film batteries. Again, cycling could only be done at high C-rates,[6] because of the limitation on the minimum current density that leads to electrolyte decomposition. Table 4.4 shows the corresponding current density for each C-rate.

Much of the trends observed for both the thin films and the interdigitated electrodes can be observed here. The appearance of the s-shape in the charge curve after about 20 cycles, the presence of a large, irreversible capacity on first charge, an initially increasing capacity, poor coulombic efficiency at C-rates above 60 C, etc., are present in the thick-film profile. However, unlike the other two, its cycle life is small. If we go by the position of the second sets of 6 C rate, we see that its capacity is fallen to less than 50 % of its initial capacity at 6 C, suggesting that it has a poor cycle life. This is consistent with the fact that thicker films do not undergo volume changes associated with charge and discharge as facilely as nanostructured materials. Although the SEM micrograph of the film after cycling is not available at the moment, it should be unsurprising to find that the film is

[6]These C-rates, too, aren't based on a theoretical value, but are relative to the first C-rate, 6 C, which was determined from the experimental data.

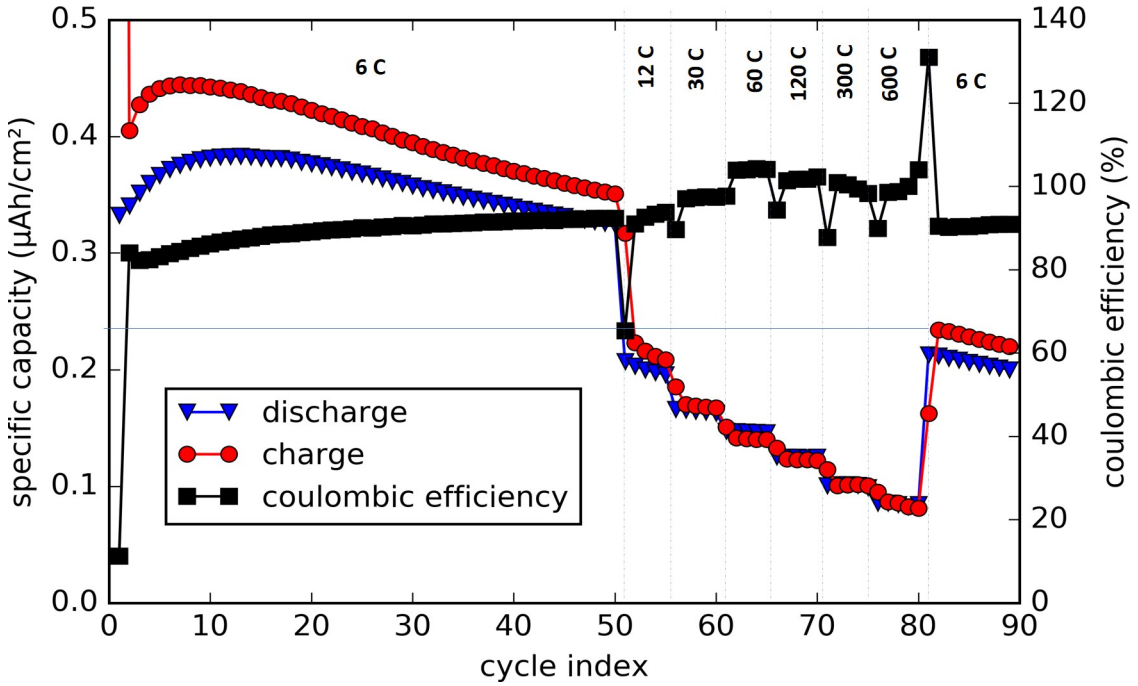

FIGURE 4.22: Cycling performance of symmetrical thick-film battery.

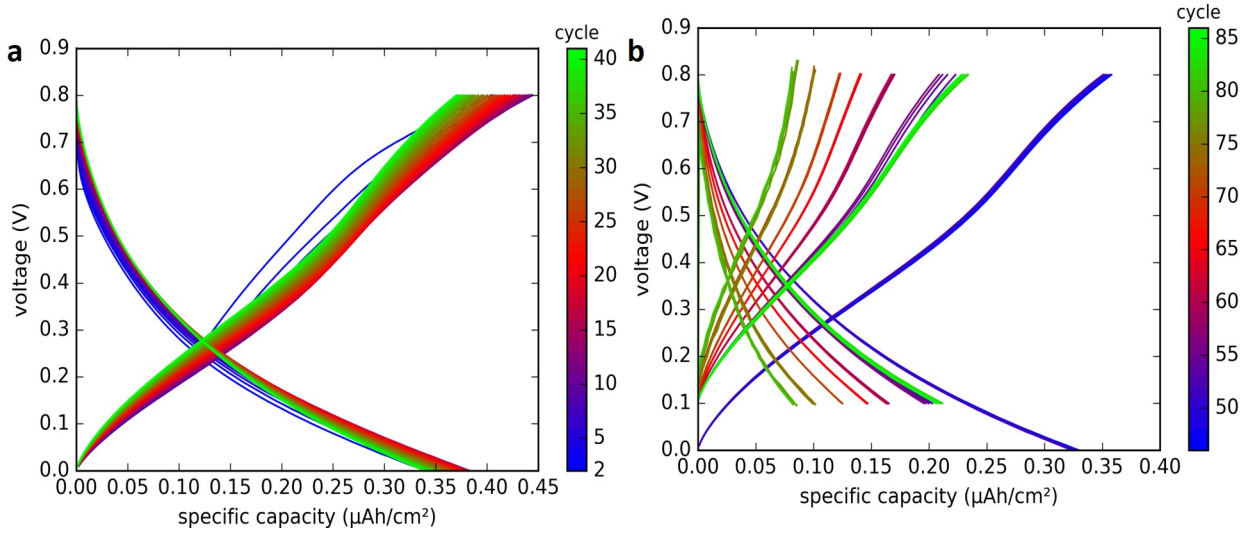

FIGURE 4.23: Galvanostatic voltage profile for symmetrical thick-film battery for (a) 2nd to 43rd cycle; (b) 44th to 90th cycle.

substantially disfigured. Its maximum capacity, at 6 C, is 0.45 μAh/cm^2; in comparison to the thin-film battery, we see that for a 40-time increase in thickness, its capacity increases only 5 times! This, as has been discussed, is a consequence of the limitations on diffusion of ions in thick film electrodes.

TABLE 4.4: Corresponding current densities and cycle indices for C-rates shown in Figure 4.22

C-rate	Current density ($\mu A/cm^2$)	Cycle ID
6 C	2.47	1–50
12 C	4.94	51–55
30 C	12.35	56–60
60 C	24.70	61–65
120 C C	49.40	66–70
300 C	123.50	71–75
600 C	247.00	76–80
6 C	2.47	81–90

4.3.4 Electrochemical performance comparison of as-reported 3D microbattery with other 3D microbatteries in the literature

As we have seen, much of the work on 3D-architecture microbatteries till date, especially lithium-ion batteries, are centred on half-cells, mainly because of the difficulty with assembling full cells with 3D architectures [89]; besides, as we should expect, the areal capacity of microbatteries increase with the height of the 3D components (because of an increase in the active materials). But the interest in microbatteries – for use in (micro)electronic devices, etc. – is areal, not volumetric, implying that, ideally, the performance of microbatteries ought to be reported on the basis of their area, not volume [47]. These facts present challenges to comparing our results, which is that of a full cell, to those in the literature. However, to be fair to all parties, it seems reasonable to compare the results on a volumetric basis, as many of the batteries with large capacity per unit footprint area have these large values because of their high 3D components.

Table 4.5 presents data, mostly for full cells, of the performance of batteries made of 3D nanostructured electrodes, with architecture similar to ours, in chronological order. None of the data is later than from 2010. The kinds of the electrodes, the cycle rates, etc., are also presented to enable the reader make meaningful judgements. What is, however, indisputable is that our battery performs way better than average, in spite of its small cell voltage. If the differences in C-rates, and the fact that ours is a full cell, were accounted for, it would be unsurprising that our battery has the best characteristics. Besides this, the excellent cyclability of the batteries (save for the thick-film battery) has been presented, which, although not shown on the table, exceeds that of almost every battery presented there[7].

[7]The reader is strongly encouraged to confirm this.

4.3.5 Gravimetric Capacities

Finally, the gravimetric capacities of the batteries are presented. Although it's preferred that the capacities of microbatteries be reported on the basis of their area, most of the literature report the capacity of batteries, in general, on a gravimetric basis. During the course of the work, the mass of electrolessly deposited PAni was never measured, because of the complexity of integrating a quartz crystal microbalance (QCM) with the deposition system.

However, the density of PAni, electrolessly deposited from a solution with the same composition as ours, and under similar conditions, has been reported to be 1.4 g/cm^3 [105]. Going by this, the mass of electrolessly deposited PAni, hence gravimetric capacities can be calculated. Table 4.6 presents the results of these calculations.

TABLE 4.6: Gravimetric capacities of fabricated batteries

Battery type	**Mass of PAni** (mg)	**Gravimetric capacity** (mAh/g)
3D battery	0.0135	26.51
Thin-film battery	0.00567	8.57
Thick-film battery	0.2268	1.61

The theoretical capacity of PAni can be easily calculated from Figure 2.22b. Considering that the mid-redox state, emeraldine, is the state in which our PAni films and shell is synthesized, replacing the anion A^- with the sulfate ion SO_4^{2-}, and noting that the faradaic process involves two electrons, it can be easily shown that the theoretical capacity of PAni is 96.4 mAh/g. In so far as the author is aware, there's been only one work [106], from 1968, which has reported the use of PAni as symmetrical electrodes. There, PAni was used in the bulk – in pellet form – and the capacity reported was 13 mAh/g. We see, then, our 3D microbattery gives the best result for PAni-based symmetrical batteries so far. Again, this is due to (1) the interdigitated nature of the electrodes, which offer short ion-transport, thereby substantially decreasing the inter-electrode ohmic resistance as compared to traditional battery configurations [14], and (2) the electrode material's having a nanostructured, 3D architecture that allow for rapid ion diffusion and efficient charge collection [8, 14, 78]. As we have seen, the inability to cycle the batteries at low enough C-rates (due to electrolyte decomposition) prevented us from attaining the theoretical capacity.

TABLE 4.5: Electrochemical performance comparison of as-reported 3D microbattery with other 3D batteries in the literature.

Author	Cathode-Anode	C-rate	Volumetric energy density (μWh/cm^2.μm)	Volumetric power density (μW/cm^2μm)	Comments
ID-3DB[a]	PAni-PAni	1.4 C, 50 C	0.189, 0.006	0.2646, 3.9	Full cell: Symmetrical interdigitated electrodes.
Ref. [100]	$LiFePO_4$–Li	1 C, 10 C	0.05, 0.01	0.05, 1	Half cell.
Ref. [64]	$LiNi_{1/3}Co_{1/3}Mn_{1/3}O_2$–C-coated $Li_4Ti_5O_{12}$	0.1 C	3.12	0.312	Full cell.
Ref. [78]	($Ni_{core}-NiO_{shell}$) 3DNWN–Li	C/10, 1 C	202.5, 75	20.25, 75	Half cell.
Ref. [101]	$LiCoO_2$–Li	14 μA/cm^2[b]	0.17	0.05	Used solid-state electrolyte, half cell.
Ref. [89]	$LiMnO_2$–NiSn	1 C, 1000 C	4.5, 0.6	4.5, 3600	Full cell.
Ref. [102]	$P_2-Na_{2/3}Ni_{1/3}Mn_{2/3}O_2$–Sb nanorod	C/7	143	20	Full cell, Na-ion battery.
Ref [103]	$LiFePO_4$–$Li_4Ti_5O_{12}$	1 C	5	5	Full cell.
Ref. [104]	LMO–NiSn	1.5, 870	0.01, 15	22.9, 5870	Full cell.

[a]ID means "interdigitated," referring to the 3D battery in this work.
[b]Only current density was given.

5 Conclusions and Recommendations

5.1 Conclusions

This work presents the foremost attempt at fabricating *symmetrical* microbatteries with interdigitated electrodes from nanostructured polymeric materials. The impetus is the inability of state-of-the-art microbatteries to simultaneously meet the performance and size requirements for modern-day, constantly miniaturizing devices. To this end, the *type*, *dimensionality*, and *architecture* of electrode materials were exploited. The choice of polyaniline (PAni) as the electrodes' active material stems from its having a substantial potential difference between its extreme redox states, thereby making it utilizable as an electrode material for symmetrical batteries. Its being nanostructured implies a short diffusion length for charge carriers (ions and electrons), causing it to charge and discharge faster (i.e., have a high power). In addition, it confers on the electrodes the ability to facilely undergo the structural changes associated with cycling. Its 3D interconnected core-shell nanowire network architecture provides the ability to tailor the battery's areal capacity without compromising on power density; moreover, the presence of a metallic core – Pt – results in efficient charge collection during the faradaic processes that drive the battery. Finally, the use of interdigitated electrodes allows compact integration of the anode and cathode on a single substrate, consistent with the requirements for microelectronics applications, and reduces the ohmic resistance of the system that results from ions having to shuttle long distance between electrodes.

In order to meet the purpose of this work, there was the need to initially ascertain the optimal parameters for nanowire growth and functionalization, and planar-surface functionalization. Subsequently, the cell components that results in optimal battery performance had to be found. After establishing and fabricating all cell components, they were assembled and the resulting batteries were tested. Batteries made of symmetrical thin-films, thick-film, and interdigitated, electrodes were assembled and tested. The interdigitated electrodes are made of 3D interconnected Pt_{core}-$PAni_{shell}$ nanowire networks.

It was found that the suitable electrolyte for the batteries is a non-aqueous electrolyte, 1 M $LiClO_4$ in acetonitrile, as aqueous electrolytes lead to decomposition of the active material (PAni). The potential range within which to cycle the battery was determined to be between 0.1 V and 0.8 V. Despite the large stability window of the non-aqueous

electrolyte, electrolyte decomposition was still observed at low current densities, requiring that cycling be done, at a minimum, at 1.4 C for the interdigitated electrodes, 20 C for the thin-film electrodes, and at 6 C for the thick-film electrodes. Consequently, it was challenging to access the full capacity of the batteries.

As expected, going by the opening paragraph, the symmetrical battery with interdigitated electrodes performs best: it presented a specific capacity of 2.7 μAh/cm^2. On the other hand, the thin- and thick-film electrode batteries had capacities of 0.09 μAh/cm^2 and 0.45 μAh/cm^2, respectively. The shell (PAni, the active material) of the nanowire network that make up the interdigitated electrodes was only 50 nm thick, the same as the thickness of the thin-film electrodes; yet, the interdigitated electrodes presented a capacity 30 times greater than the thin film's for the same footprint area! Although theoretical calculations by the author predict a 58-time increase, the lower value is consistent with the fact that cycling was done at rates that make it challenging to access their full capacities, and the possibility of some nanowire delamination. Perhaps, a more obvious example of the advantages conferred by our architecture and nanostructuring is that the interdigitated electrodes have a higher capacity than the thick-film, whose active-material thickness is 2 μm. Also, comparing the thick-film battery to the thin-film battery, we see that for a 40-time increase in thickness, the capacity of the thick-film battery increases only 5 times. This, as has been discussed, is a consequence of the limitations on diffusion of ions in thick film electrodes. Moreover, besides the thick film, the other batteries have excellent cyclability, as it has been shown that their cycle lives exceed 200 cycles.

A comparison is made between the 3D battery fabricated in this work and others (published between 2010–2018) in the literature (see Table 4.5). To account for differences in mass loading (that results from longer 3D structures), the comparison is presented on a volumetric basis. We see that our battery performs comparably, in spite of its being symmetrical and having a relatively lower cell voltage than the others.

A recurring question (to the author, at least) during the course of the work is whether the characteristics of PAni is more representative of a pseudocapacitor. In general, the nature of the cyclic voltammogram (CV) is the arbiter of this question [96, 97]. As long as the CV possesses peaks, which result from faradaic processes, then the material in question is a battery; on the other hand, (pseudo)capacitors present rectangular CVs, with no peaks, because the processes that lead to energy storage occur at or near the surface of the electrode material, leading to electrochemical double layer-like electrochemical features. The confusion arises because energy storage in both batteries and pseudocapacitors result from faradaic processes. Worse, when battery electrode materials are nanostructured (like ours), they present similar linear galvanostatic charge-discharge voltage profile as (pseudo)capacitors; however – and importantly – while the linear voltage profile of pseudocapacitors result from their stored energy being concentrated on the electrode's

surface (therefore making it easy to release charges), the linear voltage profile for nanostructured battery materials result from charge carriers' having shorter diffusion paths [59]. The recommendation [96, 97], in this case, when a capacitor-like behaviour doesn't result from intrinsic electrochemical process, but from nanostructuring, is to call such material an *extrinsic pseudocapacitor*. But to decide whether a material is a "battery" or "(pseudo)capacitor," look to the cyclic voltammogram!

The author presents the results of theoretical calculations (Figure 5.1) that show the full potential of the symmetrical interdigitated battery. Recall that the length of the nanowires used in this work was only 10 μm and that the thickness of the PAni core was 50 nm; it's obvious, then, that by increasing the length of the nanowires and/or thickness of the PAni shell, the effective area per unit footprint area, hence specific capacities, of the battery will also increase, because the amount of active material is larger. It should be evident that the increase in capacity is exactly the same as the increase in effective area per unit footprint area. Figure 5.1 shows the theoretical increase with variation of nanowire height and variation of film thickness, respectively.

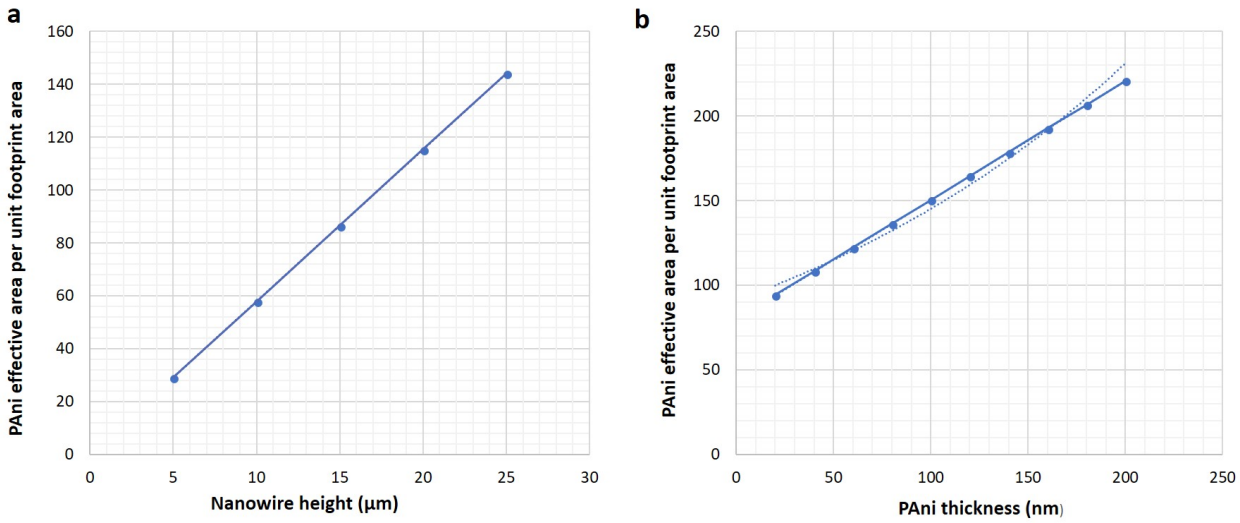

FIGURE 5.1: Increase in PAni effective area per unit footprint area or capacity for (a) Varying nanowire heights for 50-nm thick PAni; (b) Varying PAni film thickness for 20 μm nanowire height.

Evidently, there are limitations on these values. In the case of PAni thickness, we have seen in Section 4.1.3 that beyond 120 nm, the PAni shells from all nanowires merge, making the sample effectively a thick film. If this happens, although the areal capacity increases, all other advantages that results from reduced dimensionality are lost. On the other hand, if the nanowires become too long, the ohmic resistance of the electrodes will become so high that, again, it offsets the advantages of increased areal capacity [14]. Besides, there's a limit on the height of the nanowires that can be fabricated with template-assisted electrodeposition, and at some point, the nanowires are so high that the battery is

no longer a microbattery. The optimal film thickness and nanowire length will be dictated by the balance between the intended areal capacity and power.

Conclusively, this work has indisputably evidenced the possibility of a working symmetrical battery with interdigitated electrodes based on a 3D core-shell nanowire network architecture. Comparison of the results to thin- and thick-film batteries' shows superior performance, just as the exploited properties predict. In addition, it compares favourably with recent results in the literature based on similar 3D architectures. It's no doubt a proof of concept for future works based on materials with higher voltages.

5.2 Recommendations

There are many avenues for improving the performance of the 3D battery presented in this work; the existence of multiple degrees of freedom for performance optimization is what makes 3D batteries promising to meet the energy needs of the future.

Perhaps the most notable shortcoming of using PAni is the dearth of works that explores its use in symmetrical batteries. If the full potential of PAni as a symmetric battery material is to be reached, there's the need for structured mechanistic studies on ion transport, chemistry, etc. Besides this, the electrolyte employed in the batteries seems to limit the amount of the theoretical capacity than can be accessed; if the electrode materials were in the bulk, this *might* have not been an issue, but for microbattery applications, where the mass loading on electrodes is much smaller and involves smaller cycling currents, there is the need to find a more suitable alternative. Solid organic electrolytes, because of their being more stable than liquid electrolytes, and because of the ease with which they can be integrated in batteries to form a solid-state battery, may prove to be more suitable.

Then there's the question of the adhesion of nanowires onto the substrate. The importance of this can't be overemphasized, for it's undesirable that nanowires detach during battery operation. At best, delamination of nanowires leads to reduced battery capacity; at worst, it can lead to short-circuiting that may destroy the battery and external load, even. Neither is desirable.

Finally, in many applications, the cell voltage of PAni symmetric batteries is insufficient; in such cases, alternative battery chemistries have to be explored. For instance, Nagatomo *et al.* [107] have shown that by *electrochemically* *n*- and *p*-doping polyacetylene (PA) films, respectively, one gets a symmetrical battery with an open circuit voltage E_{ocv} of 3.5 V! Whether *n*- and *p*-doping of PAni electrodes leads to a symmetrical battery with higher E_{ocv} is not clear to the author; regardless, the author appreciates the difficulty of electrochemically doping side-by-side interdigitated electrodes with 3D architecture, whether with PAni or PA nanostructures as the active material. But with the tenacity that characterizes all scientific endeavours, this hurdle will be surmounted.

Appendices

A Appendix A

A.1 Solid-state Physics of Conducting Polymers

A.1.1 One-dimensional metals

To understand discussions that will follow in the section, a review of the properties of one-dimensional materials is expedient; thus, we shall cursorily consider them. For a full treatment of the theory, Refs. [68, 108, 109] are invaluable.

Theory predicts that strictly one-dimensional systems will behave very unusually; however (luckily?), real systems contain crystal imperfections (like kinks, impurities, etc.) and contain chains of infinite lengths, reducing the expected "unusualness" predicted [68]. One obvious consequence of one-dimensionality is that obstacles can't be circumvented[1]; to define this tendency, the term "percolation" is used [68, 110]. In general, "percolation" refers to the macroscopic paths from one end of a sample to the other; for a 1D lattice with interconnected[2] bonds, *all* of the bonds (or, if you prefer, sites) between the ends must be connected for there to be connectivity between these points. We say that its *percolation threshold* is 100%, meaning that below this value, connection between these two ends is lost. (It can also be shown that the percolation threshold for a square lattice is 50 % [110], and that the higher the dimensionality of the system in question, the lower its percolation threshold.)

Besides the percolation threshold being 100 % for 1D systems, there's also the fact that their coordination number is two, i.e., each site (or bond) has only two nearest neighbours – one on each side. Now, let's consider a 1D material (one which contains atoms placed side-by-side along its length); if there's only a single bond between every pair of atoms, and If for any reason, the single bond is broken, the 1D material separates into two parts. If we, however, consider the case that there are double bonds between any pair of atoms, and one of these bonds is broken, it means that the electrons (that constitute the broken bond) have been excited from the material's valence to conduction band. As soon as this bond is broken, the distance between atoms increases, leading to a substantial

[1] The reader is enthusiastically invited to read Edwin A. Abbott's *Flatland: A Romance of Many Dimensions* to have a glimpse at the nature of being of a 1D and 2D existence. Thank me later!

[2] For a 1D system, "interconnected" is no more than to be side-by-side.

distortion in the 1D lattice[3]. Therefore, a notable consequence of one-dimensionality in materials is strong *electron-lattice coupling*. Electrons moving in such a 1D material creates a distortion that polarizes the lattice; if the effect of polarization is distinct enough, the electrons, together with the distortion they cause, are called *polarons*.

Electron-lattice coupling is highly significant in 1D materials; one of its important consequence is the *Peierls distortion or transition*. To elucidate why the Peierls distortion occurs, let's consider an isolated chain of a monoatomic 1D metal, sodium, say, with its atoms equidistant from each other (Figure A.1). Because of the extreme delocalization expected of such a system, we expect a close approximation to the nearly free electron model (i.e., one considering the Bloch potential to a free electron gas). The resulting electronic density of states and energy dispersion relation plots are also shown in Figure A.1a. When the arrangement of the atoms is altered by alternating the bond lengths such that they are no more equidistant, the resulting energy of the system is lowered by the creation of a bandgap (Figure A.1b). Consequently, at low temperatures, the system will know (by fluctuations) that it gains energy upon distortion and thus it will distort: electron–lattice coupling will drive the one-dimensional metal into an insulator.

A.1.2 Conjugated double bonds

From organic chemistry, we know there are three types of double bonds, *viz., isolated, cumulated, and conjugated*; the type of interest to us are the conjugated double bonds, which are double bonds that alternate with single bonds. Conjugated polymers are very notable examples (or similitudes) of 1D metals: They constitute of long chains of carbon atoms, whose sp^2p_z hybridization leads to one unpaired electron per carbon atom, strongly bound along the chain, and have weak interchain bonds. Figure A.2 shows some important examples of conjugated polymers[4]; one would naturally expect a semiconducting or metallic behaviour from them, but all of the compounds in Figure A.2 are insulating (or, at best, semiconducting) in their chemically pure form.

A.1.3 Polyacetylene as the archetypical ID metal

Polyacetylene[5] $(CH)_x$ lends itself as an exemplary conducting polymer upon which to base the following discussion, because of its rather "simple" structure when compared to the other polyenes in Figure A.2; specifically, its structure implies that the single and double bonds can be interchanged without affecting the energy of the system, leading to a degenerate ground state, as Figure A.3 depicts [68, 69, 111, 112]. Hence, we shall

[3] It should be obvious that such excitation, while would create charge carriers in 3D systems, it would not lead to sensible distortions in a 3D lattice.

[4] Polyaniline shown here is in its fully reduced form, *leucoemeraldine* (see Section 2.4.1).

[5] Note that the discussion refers to polyactetylene in the *cis*-state.

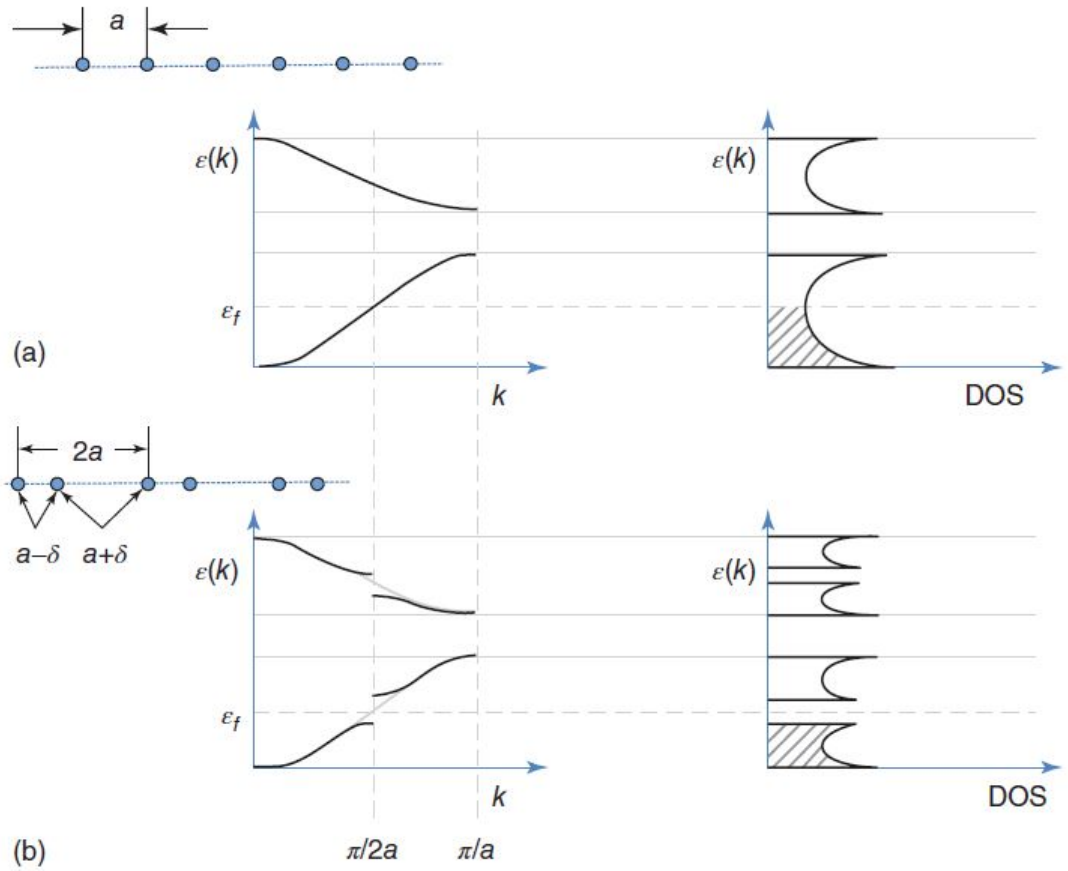

FIGURE A.1: Crystal lattice, electronic density of states, and electron dispersion relation of an isolated chain of equidistant monoatomic metal atoms (a) without distortion (b) with distortion [68].

initially consider the source of its conductivity, then extend the result to the nondegenerate ground-state polyenes, one of which is polyaniline, the material of interest.

Now to the matter at hand. To see why polyacetylene (or any other conducting polymer at that) is not conducting in its chemically pure form, as we would expect, recall the Peierls distortion described in Section A.1.1. The state of being conjugated implies alternating bond lengths [6], which is similar to the case of Figure A.1b; therefore, at low temperatures, a bandgap emerges, since it's energetically more favourable for the system. The Peierls transition occurs at a temperature T_p in the same order of magnitude as the gap energy E_g – above that temperature many electrons are thermally excited across the gap and the solid does not "notice" the gap anymore [68]. Just as with superconductivity (which is, in fact, a peculiar type of Peierls transition, as it, too, is a consequence of electron-lattice coupling, $E_g \sim 4k_bT_p$, which implies that a bandgap opening of 1 eV occurs at $\sim$ 3000 K, way above room temperature; hence, conjugated polymers are always insulating (or semiconducting) at room temperature.

[6] Single bonds are longer than double bonds, albeit not twice as long.

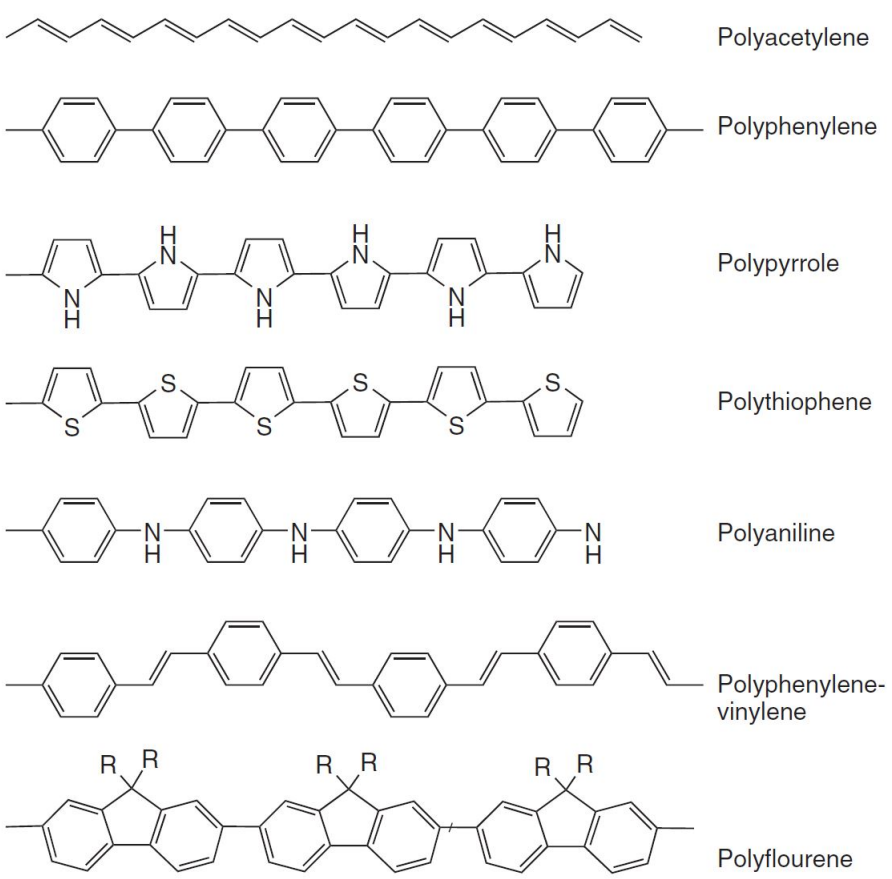

FIGURE A.2: Chemical structure of some important conjugated polymers [68].

Notwithstanding (luckily?), as in every material, *strict* alternation of the bonds is not always conserved throughout the chain length: defects exist, leading to "lattice" misfits, which separate the polymer in question into domains, especially when there's an *odd* number of carbon atoms [112]. Some possible nature of misfits are shown in Figure A.4; the energy states of these misfits are within the bandgap – near its center [109] – of the material, which are easily observable in optical absorption spectra of conjugated polymers as "midgap states" [68].

These misfits are called *solitons*[7]; they have been experimentally observed through electron spin resonance (ESR) studies [68, 109], and, contrary to how they are depicted in Figure A.4, they are delocalized over a distance of about about $14a$, where a is the lattice parameter (length of a single domain), causing them to have a small effective mass, one closer to the electronic mass rather than ionic mass [109] (specifically, it's six free electron masses [111] for polyacetylene). Very noteworthy is that, as has been proven by Pople and Walmsley (1962) [112], these solitons are mobile and can carry charge, giving rise to conductivity. In addition, solitons always exist in pairs and the other party is called – yes,

[7]Some other names it has borne throughout its history are conformational or configurational defect, misfit, domain wall, Pople-Walmsley defect, phase slip center, etc.

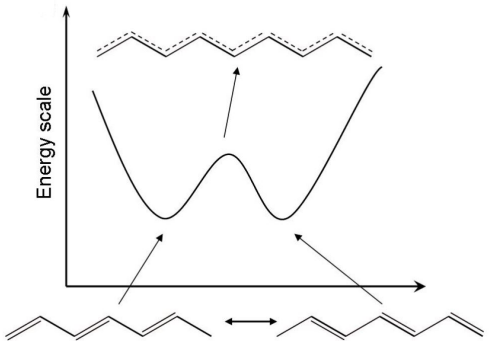

FIGURE A.3: The degenerate ground states of polyacetylene (Adapted from [69]).

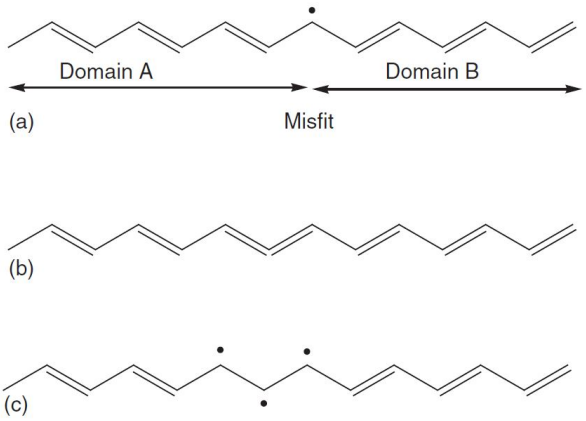

FIGURE A.4: Misfits or domain boundaries in a conjugated chain: (a) two adjacent single bonds plus a dangling bond; (b) two adjacent double bonds, leading formally to a pentavalent carbon atom; and (c) three dangling bonds on a misfit [68].

you guessed right! – *antisolitons*. There's no standard nomenclature for naming the initially observed soliton – but once that one is named, you have to call the subsequent one the opposite [68]. Figure A.5 shows how solitons and antisolitons are created and migrate, leading to electrical conductivity, in polyacetylene.

The solitons discussed so far (Figure A.5) are neutral solitons (radicals) – i.e., they have no charges associated with them; in addition to neutral solitons, however, positively and negatively charged solitons also exist. By now, it should be obvious that they will *always* be solitons due to syntheses, but in a pristine polymer, they are of very low concentration – about 400 radicals per 10^6 carbon atoms for polyacetylene [68] – not enough to confer substantial conductivity. Fortuitously, the concentration of solitons can be increased by various methods, *viz.* (i) chemical doping, (ii) photogeneration, and (iii) charge injection [66, 68, 108, 109]. Therefore, effectively, the function of these methods is the depression of the Peierls transition, so that the metallic state is conserved due to the high soliton concentration.

Chemical doping of conjugated polymers is a reversible redox process; hence,

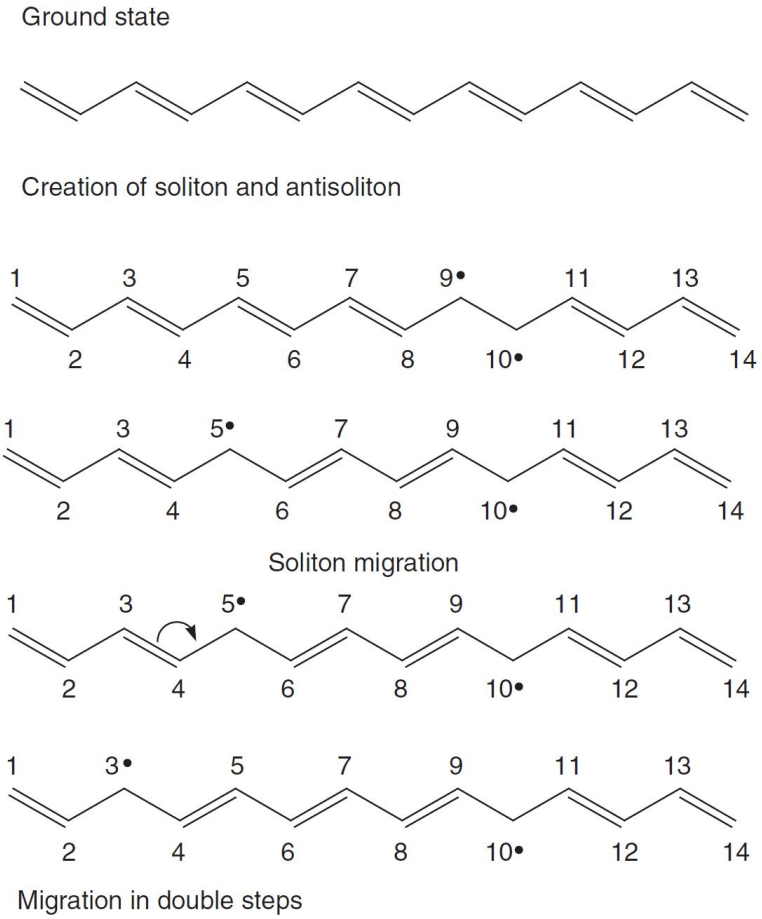

FIGURE A.5: Generation and migration of solitons and antisolitons in polyacetylene [68].

the doping of conjugated polymers implies (i) charge transfer (by oxidation, p type, or reduction, n type), (ii) the associated insertion of a counter ion (for overall charge neutrality), and (iii) the simultaneous control of the Fermi level or chemical potential. Through doping, the electronic and optical properties of conjugate polymers can be controlled over the full range from insulator to metal [109]. Furthermore, it's important to note that, even though electronic and ionic charges can equally compensate at the defect and unperturbed part of the chain, the defects are more sensitive to redox reactions than the rest of the chain [68]. The following are some examples of redox reactions used to dope polyacetylene and Figure A.6 depicts this doping mechanism:
p-type doping:

$$(\mathrm{CH})_x + 3\,\mathrm{I}_2 \longrightarrow (\mathrm{CH})_x{}^{++} + 2\,\mathrm{I}_3^- \tag{A.1}$$

n-type doping:

$$(\mathrm{CH})_x + \mathrm{K} \longrightarrow (\mathrm{CH})_x^- + \mathrm{K}^+ \tag{A.2}$$

In the first step, a double bond is broken followed by the transfer of an electron from the polymer chain to the dopant. Thus, two solitons are created: one neutral and

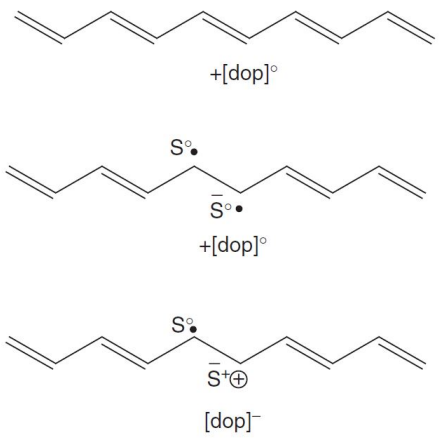

FIGURE A.6: Creation of solitons by chemical doping of a polyacetylene chain [68].

the other positively charged. For p-doping, the next dopant will react with the neutral soliton, because in most p-doping reactions, stoichiometry requires the transfer of two electrons [68]. For n-doping, however, only one electron is transferred; in both cases, very few neutral solitons will survive, because they will diffuse along the chain and annihilate with antisolitons from other doping events.

A.1.4 The case of polyaniline

Recall it was shown that polyacetylene is a case of degenerate polyenes, as interchanging the positions of the single and double bonds is inconsequential to the system. However, every other polymer in Figure A.2 is *nondegenerate*, in that interchanging the positions of the bonds results in different energy states of the system.

In PAni, this difference leads to two different structures – *aromatic* and *quinoid* structures – whose general chemical structure and relative energies are shown in Figure A.7. We can see that that the quinoid state has a higher energy than the aromatic state.
In order to stabilize conjugational defects in PAni (or any other nondegenerate ground-state polymer at that), bound *double*, not single, defects have to be formed [68, 108, 113–115]. Such double defects are called *polarons*. Again, as-prepared polyaniline, in the emeraldine base form, (Figure A.8 a) is semiconducting; but by *p*-doping with acid, the concentration of polarons increases (Figure A.8 b-d), leading to a semiconductor-to-metal transition to a conductivity value of 5 S/cm, an increase by a factor of 10^{10}. [114, 115].

Polarons are solitons bound to either a negative or positive charge. As Figure A.8 shows, a bipolaron (two positive charges[8])is formed, which is unstable, then morphs into a polaron and separates into a polaron lattice along the polymer chain. Finally, as we have seen in the case of solitons, its optical signature is the presence of a single midgap state; a

[8]The same name applies if it were two negative charges.

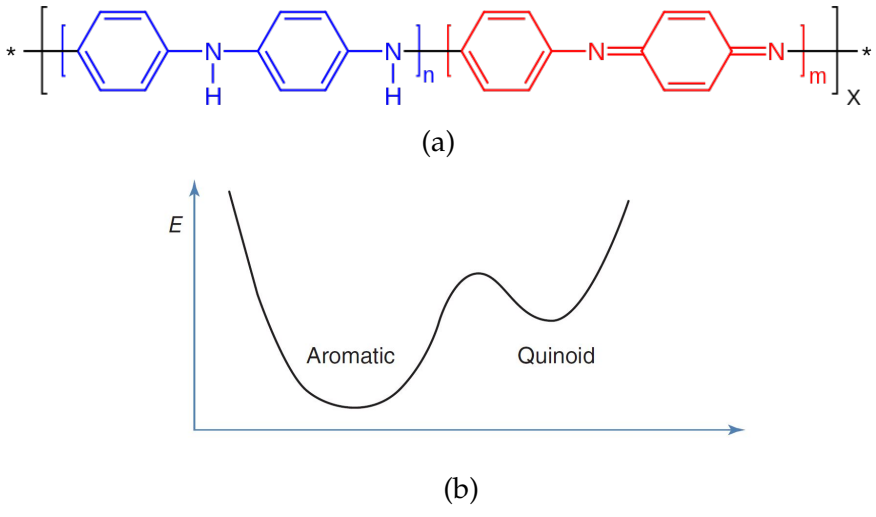

FIGURE A.7: (a) General polyaniline structures, n+m = 1, x = half degree of polymerization (Adapted from Ref. [67]); (b) the nondegenerate ground states of polyaniline. (Adapted from Ref. [68].)

polaron, however, because it consists of two defects, is characterized by two states in the gap [68]. Optical absorption spectra studies and band structure calculations [114] have shown that, unlike all other doped nondegenerate conducting polymers that exhibit two midgap states, PAni exhibits only one broad midgap band with a very narrow band nearly degenerate with the conducting band edge. Because this narrow gap is almost degenerate with the conduction band, it's not observed in doped PAni's optical absorption spectrum.

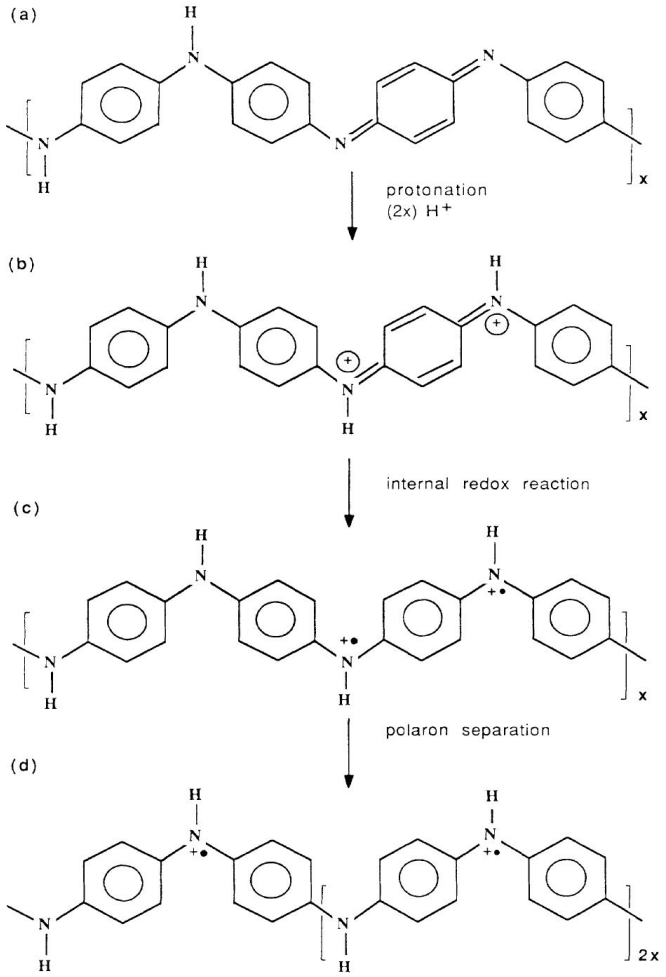

FIGURE A.8: Creation of polarons by chemical doping of a polyaniline chain: (a) before protonation; (b) formation of bipolarons; (c) formation of polarons; (d) separation of of polarons, resulting in a polaron lattice [114].

Bibliography

[1] Chin-Lung Hsu and Judy Chuan-Chuan Lin. "An empirical examination of consumer adoption of Internet of Things services: Network externalities and concern for information privacy perspectives". In: *Computers in Human Behavior* 62 (2016), pp. 516–527. ISSN: 0747-5632.

[2] The Statistics Portal. *Internet of Things (IoT) in Europe - Statistics & Facts | Statista*. 2018.

[3] Louis Columbus. *2017 Roundup Of Internet Of Things Forecasts*. 2017.

[4] A. Zuttel et al. "Hydrogen: the future energy carrier". In: *Philosophical Transactions of the Royal Society A: Mathematical, Physical and Engineering Sciences* 368.1923 (2010), pp. 3329–3342. ISSN: 1364-503X. arXiv: arXiv:1011.1669v3.

[5] Da Deng. "Li-ion batteries: Basics, progress, and challenges". In: *Energy Science and Engineering* 3.5 (2015), pp. 385–418. ISSN: 20500505. arXiv: /doi.org/10.1002/ese3.95 [https:].

[6] M. Armand and J. M. Tarascon. "Building better batteries". In: *Nature* 451.7179 (2008), pp. 652–657. ISSN: 00280836. arXiv: 1005.0853.

[7] Bruno Scrosati and Jürgen Garche. "Lithium batteries: Status, prospects and future". In: *Journal of Power Sources* 195.9 (2010), pp. 2419–2430. ISSN: 03787753. arXiv: 97/0302-023 [0935-9648].

[8] Yury Gogotsi. "What nano can do for energy storage". In: *ACS Nano* 8.6 (2014), pp. 5369–5371. ISSN: 1936086X.

[9] Lixiang Liu et al. "Advances on Microsized On-Chip Lithium-Ion Batteries". In: *Small* 13.45 (2017), pp. 1–12. ISSN: 16136829.

[10] Liqiang Mai et al. "Single Nanowire Electrochemical Devices". In: *Nano Letters* 10.10 (2010), pp. 4273–4278. ISSN: 1530-6984.

[11] Yuxing Wang et al. "Lithium and lithium ion batteries for applications in microelectronic devices: A review". In: *Journal of Power Sources* 286.March (2015), pp. 330–345. ISSN: 03787753.

[12] Jeffrey W. Fergus. "Ceramic and polymeric solid electrolytes for lithium-ion batteries". In: *Journal of Power Sources* 195.15 (2010), pp. 4554–4569. ISSN: 03787753.

[13] Peter H.L. Notten. "3D-integrated all-solid-state batteries". In: *Europhysics News* 42.3 (2011), pp. 24–29. ISSN: 0531-7479.

[14] Jeffrey W. Long et al. "Three-dimensional battery architectures". In: *Chemical Reviews* 104.10 (2004), pp. 4463–4492. ISSN: 00092665.

[15] Debra R. Rolison et al. "Multifunctional 3D nanoarchitectures for energy storage and conversion". In: *Chem. Soc. Rev.* 38.1 (2009), pp. 226–252. ISSN: 0306-0012.

[16] Wei Wang, Miao Tian, and Aziz Abdulagatov. "Three-Dimensional Ni / TiO2 Nanowire Network for High Areal Capacity Lithium-Ion Microbattery Applications". In: *Nano Letters* 12 (2012), pp. 655–660.

[17] M. Rosa Palacín. "Recent advances in rechargeable battery materials: a chemist's perspective". In: *Chemical Society Reviews* 38.9 (2009), p. 2565. ISSN: 0306-0012.

[18] *THE COST COMPONENTS OF A LITHIUM ION BATTERY*. 2017.

[19] Gert Berckmans et al. "Cost projection of state of the art lithium-ion batteries for electric vehicles up to 2030". In: *Energies* 10.9 (2017). ISSN: 19961073.

[20] Yanliang Liang, Zhanliang Tao, and Jun Chen. "Organic electrode materials for rechargeable lithium batteries". In: *Advanced Energy Materials* 2.7 (2012), pp. 742–769. ISSN: 16146832.

[21] M. Jeffrey Oakes. "A Brief History of Batteries and Stored Energy". In: *NETA World* (2006), p. 6.

[22] Paul T. Keyser. "The Purpose of the Parthian Galvanic Cells : A First-Century A . D . Electric Battery Used for Analgesia". In: *Journal of Near Eastern Studies* 52.2 (1993), pp. 81–98.

[23] Aran Frood. *BBC NEWS | Science/Nature | Riddle of 'Baghdad's batteries'*. 2003.

[24] Thomas S Kuhn. *The Structure of Scientific Revolutions*. Vol. II. 2. 1970, p. 210. ISBN: 0226458032. arXiv: 0-226-45803-2.

[25] John L . Heilbron. "G . M . Bose : The Prime Mover in the Invention of the Leyden Jar ?" In: 57.2 (1966), pp. 264–267.

[26] Jerome W. Harrison and Charles A. White. *Magnetism and Electricity*. 5th. 1898.

[27] Rhett Allain. *The Physics of the Leyden Jar in*.

[28] B. Adam Allerhand. "Who Invented the Earliest Capacitor Bank (" Battery " of Leyden Jars)? It 's Complicated". In: *Proceedings of the IEEE* 106.3 (2018), pp. 496–503.

[29] Benjamin Franklin. *The Papers of Benjamin Franklin*. Ed. by Leonard W. Labaree. New Haven: Yale University Press, 1961.

[30] R. Cecchini and G. Pelosi. "Alessandro Volta and his battery". In: *IEEE Antennas and Propagation Magazine* 34.2 (1992), pp. 30–37. ISSN: 1045-9243.

[31] M. Stanley Whittingham. "Electrical Energy Storage and Intercalation Chemistry". In: *Science* 192.4244 (1976), pp. 1126–1127.

[32] Michael Stanley Whittingham. *Battery Based Chalcogenides*. 1973.

[33] Gholam-Abbas Nazri and Gianfranco Pistoia, eds. *Lithium Batteries: Science and Technology*. 1st ed. New York: Springer US, 2003, pp. XX, 708. ISBN: 978-0-387-92675-9.

[34] Jung-ki Park. *Principles and Applications of Lithium Secondary Batteries*. Weinheim: Wiley-VCH, 2012, p. 372. ISBN: 9783527328833.

[35] Allen J Bard et al. *Electrochemical Methods: Fundamentals and Applications*. 2nd. New York: John Wiley & Sons, Inc., 2001, pp. 3–7. ISBN: 9780123813749. arXiv: 1011.1669v3.

[36] David Linden and Thomas B. Reddy, eds. *Handbook of Batteries*. 4th ed. New York: McGraw-Hill, 2004, p. 1200. ISBN: 0071359788. arXiv: 9809069v1 [arXiv:gr-qc].

[37] Patricia Amateis and Martin Silberberg. *Chemistry: The Molecular Nature of Matter and Change*. New York: McGraw-Hill, 2017. ISBN: 978–0–07–304859–8.

[38] Robert E. Lucas Jnr. *The Industrial Revolution*. Tech. rep. Minneapolis: Federal Reserve Bank of Minneapolis, 2003.

[39] Richard S. Nicholson. "Theory and Application of Cyclic Voltammetry for Measurement of Electrode Reaction Kinetics". In: *Analytical Chemistry* 37.11 (1965), pp. 1351–1355. ISSN: 0003-2700.

[40] Richard S. Nicholson and Irving Shain. "Theory of Stationary Electrode Polarography: Single Scan and Cyclic Methods Applied to Reversible, Irreversible, and Kinetic Systems". In: *Analytical Chemistry* 36.4 (1964), pp. 706–723. ISSN: 15206882.

[41] Noémie Elgrishi et al. "A Practical Beginner's Guide to Cyclic Voltammetry". In: *Journal of Chemical Education* 95.2 (2018), pp. 197–206. ISSN: 19381328.

[42] Akiya Kozawa and R A Powers. "Electrochemical Reactions in Batteries Emphasizing the MnO, cathode of dry cells". In: *Journal of Chemical Education* 49.9 (1972), pp. 587–591.

[43] Naoki Nitta et al. "Li-ion battery materials: Present and future". In: *Materials Today* 18.5 (2015), pp. 252–264. ISSN: 18734103. arXiv: arXiv:1011.1669v3.

[44] M. Rosa Palacín. "Recent advances in rechargeable battery materials: a chemist's perspective". In: *Chemical Society Reviews* 38.9 (2009), p. 2565. ISSN: 0306-0012.

[45] Dominique Larcher et al. “Recent findings and prospects in the field of pure metals as negative electrodes for Li-ion batteries”. In: *Journal of Materials Chemistry* 17.36 (2007), p. 3759. ISSN: 0959-9428.

[46] J-M. Tarascon et al. “Nano-sized transition-metal oxides as negative-electrode materials for lithium-ion batteries”. In: *Nature* 407.6803 (2000), pp. 496–499. ISSN: 00280836.

[47] Jean Louis Souquet and Michel Duclot. “Thin film lithium batteries”. In: *Solid State Ionics* 148.3-4 (2002), pp. 375–379. ISSN: 0167-2738.

[48] Albert Einstein. *Relativity: The Special and General Theory*. 3rd ed. New York: Hanry Holt and Co., 1920.

[49] Herbert Marcuse. *One-Dimensional Man: Studies in the Ideology of the Advanced Industrial Society*. 1st ed. Boston: Beacon Press, 1964.

[50] Nobel Media AB. *The Nobel Prize in Physics 1986*. 2014.

[51] Nobel Media AB. *The Nobel Prize in Chemistry 1996*. 2014.

[52] Nobel Media AB. *The Nobel Prize in Physics 2010*. 2014.

[53] Nobel Media AB. *The Nobel Prize in Chemistry 2016*. 2014.

[54] Emil Roduner. “Size matters: why nanomaterials are different”. In: *Chemical Society Reviews* 35.7 (2006), p. 583. ISSN: 0306-0012.

[55] Antonino Salvatore Aricò et al. “Nanostructured materials for advanced energy conversion and storage devices”. In: *Nature Materials* 4.5 (2005), pp. 366–377. ISSN: 14761122. arXiv: {_}barataMaterialsandTechniquesofpolychromewoodensculpt

[56] L. F. Nazar et al. “Nanostructured materials for energy storage”. In: *International Journal of Inorganic Materials* 3.3 (2001), pp. 191–200. ISSN: 14666049.

[57] Candace K Chan et al. “High-performance lithium battery anodes using silicon nanowires”. In: (2007), pp. 31–35.

[58] Mihai Robert Zamfir et al. “Silicon nanowires for Li-based battery anodes: a review”. In: *Journal of Materials Chemistry A* 1.34 (2013), p. 9566. ISSN: 2050-7488.

[59] Masashi Okubo et al. “Nanosize Effect on High-Rate Li-Ion Intercalation in LiCoO2 Electrode”. In: 4 (2007), pp. 7444–7452.

[60] B. Scrosati and C. A. Vincent. “Polymer Electrolytes: The Key to Lithium Polymer Batteries”. In: *MRS Bulletin* 25.03 (2000), pp. 28–30. ISSN: 0883-7694.

[61] Binod Kumar, Stanley J. Rodrigues, and Lawrence G. Scanlon. “Ionic Conductivity of Polymer-Ceramic Composites”. In: *Journal of The Electrochemical Society* 148.10 (2001), A1191. ISSN: 00134651.

[62] M Z A Munshi. *Handbook of Solid State Batteries and Capacitors*. WORLD SCIENTIFIC, 1995. ISBN: 978-981-02-1794-5.

[63] G. Meunier, R. Dormoy, and A. Levasseur. "New positive-electrode materials for lithium thin film secondary batteries". In: *Materials Science and Engineering: B* 3.1-2 (1989), pp. 19–23. ISSN: 09215107.

[64] Robert Hahn et al. "Characteristics of Li-ion micro batteries fully batch fabricated by micro fluidic MEMS packaging". In: *Microsystem Technologies* 0123456789 (2018), pp. 1–9. ISSN: 1432-1858.

[65] Nobel Media AB. *The Nobel Prize in Chemistry 2000*. 2014.

[66] Kenneth J. Wynne and G. Bryan Street. "Conducting Polymers. A Short Review". In: *Ind. Eng. Chem. Prod. Res. Dev.*, 21.1 (1982), pp. 23–28.

[67] Wikipedia the free encyclopedia. *Polyaniline*. 2018.

[68] Siegmar Roth and David Carroll. *One-dimensional Metals: Conjugated Polymers, Organic Crystals, Carbon Nanotubes and Graphene*. 3rd ed. Weinheim: Wiley-VCH Verlag GmbH & Co., 2015. ISBN: 9783527336340.

[69] Anne Attout. "Aniline polymerization strategies for micro- and nano structuring into electrochemical sensors and biosensors". Ph.D Thesis. Université catholique de Louvain, 2010.

[70] Alexandru Vlad. "Advanced fabrication of nanowire arrays and three-dimensional nanostructures". Ph.D. Université catholique de Louvain, 2009.

[71] Akira Watanabe et al. "Comparative Study of the Redox Reactions of Polyaniline Films in Aqueous and Nonaqueous Solutions". In: *Macromolecules* 22 (1989), pp. 3323–3327.

[72] Hideharu Daifuku and Takahiro Kawagoe. "A study of the redox reaction mechanisms of polyaniline using a quartz crystal microbalance". In: 214 (1989), p. 1989. ISSN: 00220728.

[73] A. G. MacDiarmid et al. "Polyaniline: Electrochemistry and application to rechargeable batteries". In: *Synthetic Metals* 18.1-3 (1987), pp. 393–398. ISSN: 03796779.

[74] Florence Fusalba et al. "Electrochemical Characterization of Polyaniline in Nonaqueous Electrolyte and Its Evaluation as Electrode Material for Electrochemical Supercapacitors". In: *Journal of The Electrochemical Society* 148.1 (2001), A1. ISSN: 00134651.

[75] A. Attout, S. Yunus, and P. Bertrand. "Electroless deposition of polyaniline: Synthesis and characterization". In: *Surface and Interface Analysis* 40.3-4 (2008), pp. 657–660. ISSN: 01422421.

[76] Yongjun Chen, E. T. Kang, and K. G. Neoh. "Electroless polymerization of aniline on platinum and palladium surfaces". In: *Applied Surface Science* 185.3-4 (2002), pp. 267–276. ISSN: 01694332.

[77] It4ip. *Track-etching technology - it4ip*.

[78] Alexandru Vlad et al. "Three-dimensional interconnected Ni _{core} –NiO _{shell} nanowire networks for lithium microbattery architectures". In: *J. Mater. Chem. A* 4.5 (2016), pp. 1603–1607. ISSN: 2050-7488.

[79] Maria Eugenia Toimil-Molares. "Characterization and properties of micro- and nanowires of controlled size, composition, and geometry fabricated by electrodeposition and ion-track technology." In: *Beilstein journal of nanotechnology* 3 (2012), pp. 860–83. ISSN: 2190-4286.

[80] Laura Holtschi. "Synthesis and Characterization of 3D Nanowire Networks for High-areal Capacity Li-ion Battery Anodes". MSc. Université catholique de Louvain, 2016.

[81] Sahar S. Mahshid et al. "Electrodeposition of Platinum Nanowires: Electrochemical Characterization". In: *ECS Transactions*. Vol. 28. 18. The Electrochemical Society, 2010, pp. 25–35.

[82] Maral P. S. Mousavi et al. "Unbiased Quantification of the Electrochemical Stability Limits of Electrolytes and Ionic Liquids". In: *Journal of The Electrochemical Society* 162.12 (2015), A2250–A2258. ISSN: 0013-4651.

[83] Magnus Bengtsson, Dirk Müller, and Bernhard Klimt. *Picosecond lasers come of age for micromachining - Industrial Laser Solutions*. 2013.

[84] Jan Oberländer et al. "Study of Interdigitated Electrode Arrays Using Experiments and Finite Element Models for the Evaluation of Sterilization Processes". In: *Sensors* 15.10 (2015), pp. 26115–26127. ISSN: 1424-8220.

[85] Rudi Winter. *Scanning electron microscopy (SEM)*. 2015.

[86] Brent L. Adams. "Handbook of Material Charecterisation". In: *Asm* 10 (1998), p. 1310. ISSN: 0-87170-007-7(v. 1).

[87] Charles Kittel. *Introduction to Solid State Physics*. 8th ed. New York: John Wiley & Sons, Inc., 2010. ISBN: 9783540938033. arXiv: arXiv:1011.1669v3.

[88] Digital Instruments. *Scanning Probe Microscopy Training Notebook. Version 3.0*. Tech. rep. 2000.

[89] Hailong Ning et al. "Holographic patterning of high-performance on-chip 3D lithium-ion microbatteries". In: *Proceedings of the National Academy of Sciences* 112.21 (2015), pp. 6573–6578. ISSN: 0027-8424.

[90] Reza Ansari and M. B. Keivani. "Polyaniline Conducting Electroactive Polymers Thermal and Environmental Stability Studies". In: *E-Journal of Chemistry* 3.4 (2006), pp. 202–217. ISSN: 0973-4945.

[91] Katsuaki Okabayashi et al. "Electrochemical studies of polyaniline and its application". In: *Synthetic Metals* 18.1-3 (1987), pp. 365–370. ISSN: 03796779.

[92] E. M. Genies, A.A. Syed, and C. Tsintavis. "Electrochemical Study Of Polyaniline In Aqueous And Organic Medium. Redox And Kinetic Properties." In: *Molecular Crystals and Liquid Crystals* 121.1-4 (1985), pp. 181–186. ISSN: 0026-8941.

[93] Hubert H. Girault. *Analytical and Physical Electrochemistry*. 1st ed. Powles 1981. Lausanne: EPFL Press, 2004. ISBN: 0-8247-5357-7.

[94] D. S. Polcyn and Irving. Shain. "Multistep Charge Transfers in Stationary Electrode Polarography." In: *Analytical Chemistry* 38.3 (1966), pp. 370–375. ISSN: 0003-2700.

[95] J. Kasnatscheew et al. "Determining oxidative stability of battery electrolytes: validity of common electrochemical stability window (ESW) data and alternative strategies". In: *Physical Chemistry Chemical Physics* 19.24 (2017), pp. 16078–16086. ISSN: 1463-9076.

[96] Patrice Simon, Yury Gogotsi, and Bruce Dunn. "Where do batteries end and supercapacitors begin?" In: 343.6176 (2014), pp. 1210–1212.

[97] T. Brousse, D. Belanger, and J. W. Long. "To Be or Not To Be Pseudocapacitive?" In: *Journal of the Electrochemical Society* 162.5 (2015), A5185–A5189. ISSN: 0013-4651.

[98] Timothy S. Arthur et al. "Three-dimensional electrodes and battery architectures". In: *MRS Bulletin* 36.07 (2011), pp. 523–531. ISSN: 0883-7694.

[99] M. B. Pinson and M. Z. Bazant. "Theory of SEI Formation in Rechargeable Batteries: Capacity Fade, Accelerated Aging and Lifetime Prediction". In: *Journal of the Electrochemical Society* 160.2 (2012), A243–A250. ISSN: 0013-4651. arXiv: 1210.3672.

[100] E. Cohen et al. "Novel rechargeable 3D-Microbatteries on 3D-printed-polymer substrates: Feasibility study". In: *Electrochimica Acta* 265 (2018), pp. 690–701. ISSN: 00134686.

[101] Mao Shoji, Hirokazu Munakata, and Kiyoshi Kanamura. "Fabrication of All-Solid-State Lithium-Ion Cells Using Three-Dimensionally Structured Solid Electrolyte Li7La3Zr2O12 Pellets". In: *Frontiers in Energy Research* 4.August (2016), pp. 1–7. ISSN: 2296-598X.

[102] Liying Liang et al. "Large-scale highly ordered Sb nanorod array anodes with high capacity and rate capability for sodium-ion batteries". In: *Energy Environ. Sci.* 8.10 (2015), pp. 2954–2962. ISSN: 1754-5692. arXiv: {_}barataMaterialsandTechniquesofpc

[103] Ke Sun et al. "3D printing of interdigitated Li-ion microbattery architectures". In: *Advanced Materials* 25.33 (2013), pp. 4539–4543. ISSN: 09359648.

[104] James H. Pikul et al. "High-power lithium ion microbatteries from interdigitated three-dimensional bicontinuous nanoporous electrodes". In: *Nature Communications* 4 (2013), pp. 1732–1735. ISSN: 20411723.

[105] Chuanping Liao and Mingyuan Gu. "Electroless deposition of polyaniline film via autocatalytic polymerization of aniline". In: *Thin Solid Films* 408.1-2 (2002), pp. 37–42. ISSN: 00406090.

[106] R. De Surville et al. "Electrochemical chains using protolytic organic semiconductors". In: *Electrochimica Acta* 13.6 (1968), pp. 1451–1458. ISSN: 00134686.

[107] Takao Nagatomo et al. "A long-lasting polyacetylene battery with high energy density". In: *Japanese Journal of Applied Physics* 22.5 (1983), pp. L275–L277. ISSN: 13474065.

[108] William Barford. *Electronic and Optical Properties of Conjugated Polymers*. 1st ed. Oxford: Oxford University Press, 2005. ISBN: 0–19–852680–6.

[109] A. J. Heeger et al. "Solitons in conducting polymers". In: *Reviews of Modern Physics* 60.3 (1988), pp. 781–850. ISSN: 00346861.

[110] Richard Zallen. *The Physics of Amorphous Solids*. New York: John Wiley and Sons, 1998. ISBN: 0-471-01968-2.

[111] W. P. Su, J. R. Schrieffer, and A. J. Heeger. "Solitons in Polyacetylene". In: *Physical Review Letters* 42.25 (1979), pp. 1698–1701.

[112] J. A. Pople and S. H. Walmsley. "Bond alternation defects in long polyene molecules". In: *Molecular Physics* 5.1 (1962), pp. 15–20. ISSN: 13623028.

[113] a. J. Heeger. *Charge storage in conducting polymers: Solitons, polarons, and bipolarons.* 1985.

[114] S. Stafström et al. "Polaron lattice in highly conducting polyaniline: Theoretical and optical studies". In: *Physical Review Letters* 59.13 (1987), pp. 1464–1467. ISSN: 00319007.

[115] A J Epstein et al. "Insulator-to-metal transition in polyaniline". In: *Synthetic Metals* 18 (1987), pp. 303–309.